1978

# THE ELECTRON IMPACT DISSOCIATION OF SOME MOLECULES OF ENVIRONMENTAL INTEREST.

GEOFFREY. ALLCOCK
*University of Windsor*

Recommended Citation
ALLCOCK, GEOFFREY., "THE ELECTRON IMPACT DISSOCIATION OF SOME MOLECULES OF ENVIRONMENTAL INTEREST." (1978). *Electronic Theses and Dissertations.* Paper 3977.

National Library of Canada

Cataloguing Branch
Canadian Theses Division

Ottawa, Canada
K1A 0N4

# NOTICE

The quality of this microfiche is heavily dependent upon the quality of the original thesis submitted for microfilming. Every effort has been made to ensure the highest quality of reproduction possible.

If pages are missing, contact the university which granted the degree.

Some pages may have indistinct print especially if the original pages were typed with a poor typewriter ribbon or if the university sent us a poor photocopy.

Previously copyrighted materials (journal articles, published tests, etc.) are not filmed.

Reproduction in full or in part of this film is governed by the Canadian Copyright Act, R.S.C. 1970, c. C-30. Please read the authorization forms which accompany this thesis.

THIS DISSERTATION
HAS BEEN MICROFILMED
EXACTLY AS RECEIVED

Bibliothèque nationale du Canada

Direction du catalogage
Division des thèses canadiennes

# AVIS

La qualité de cette microfiche dépend grandement de la qualité de la thèse soumise au microfilmage. Nous avons tout fait pour assurer une qualité supérieure de reproduction.

S'il manque des pages, veuillez communiquer avec l'université qui a conféré le grade.

La qualité d'impression de certaines pages peut laisser à désirer, surtout si les pages originales ont été dactylographiées à l'aide d'un ruban usé ou si l'université nous a fait parvenir une photocopie de mauvaise qualité.

Les documents qui font déjà l'objet d'un droit d'auteur (articles de revue, examens publiés, etc.) ne sont pas microfilmés.

La reproduction, même partielle, de ce microfilm est soumise à la Loi canadienne sur le droit d'auteur, SRC 1970, c. C-30. Veuillez prendre connaissance des formules d'autorisation qui accompagnent cette thèse.

LA THÈSE A ÉTÉ
MICROFILMÉE TELLE QUE
NOUS L'AVONS REÇUE

# THE ELECTRON IMPACT DISSOCIATION OF SOME MOLECULES OF ENVIRONMENTAL INTEREST

by

GEOFFREY ALLCOCK

A Dissertation
Submitted to the Faculty of Graduate Studies through the
Department of Physics in Partial Fulfilment
of the requirements for the Degree of
Doctor of Philosophy at the
University of Windsor

Windsor, Ontario, Canada

1978

TO MY WIFE AND FAMILY

When I consider thy heavens,
the work of thy fingers, the
moon and the stars, which thou
hast ordained;
What is man, that thou art
mindful of him? and the son
of man, that thou visitest him?
(Psalm 8:3 - 4)

# ABSTRACT

Metastable atoms and molecules, including Rydberg species, have been directly detected following the electron impact dissociation of $CO_2$, $CCl_2F_2$, $CCl_3F$ and $N_2O$. The kinetic energies of these fragments were measured during time-of-flight spectroscopy. Excitation function measurements of fragments of known kinetic energy provided information about the mass of the detected fragment and the dissociation limit of the excited state of the parent molecule. This information was obtained from plots of fragment kinetic energy against appearance potential. These plots also enabled the dissociation processes which involve the production of two fragments to be distinguished from those which involve the production of more than two fragments. Unambiguous identification of the Rydberg fragments was achieved during use of a mass sensitive Rydberg detector. Both Rydberg and non-Rydberg fragments were also detected by an Auger detector.

Most of the dissociation processes identified in the present work produced an excited atom and an electronically excited molecule. However, in most cases the molecular fragments appeared to receive little or no vibrational energy.

# ACKNOWLEDGEMENTS

It is a pleasure to acknowledge the continual guidance and supervision of Dr. J.W. McConkey throughout the entire course of this work. I would also like to thank Dr. I.C. Malcolm for a number of helpful discussions and suggestions. Special thanks are also due to Mr. H. Dassen for providing the computer software and to the technical staff of the Department. I am also indebted to Mrs. Jean Franklin for typing the manuscript.

Finally, it is with deep gratitude that I acknowledge the continual support and encouragement of my wife, Marilyn.

During the course of this work I was supported by a University of Windsor teaching assistantship and by funds from N.R.C. research grants.

The project was financed by Environment Canada and the National Research Council of Canada.

# TABLE OF CONTENTS

# LIST OF TABLES

# LIST OF FIGURES

# INTRODUCTION AND MOTIVATION FOR RESEARCH

A detailed account of the preliminary work associated with this research project has been previously presented (Allcock, 1975). In the present account some of this background material is repeated and updated for the sake of clarity and completeness. Where necessary, additional background material is introduced in order to fully describe and explain the latest experimental results.

Metastable atoms and molecules, including Rydberg species, can be extensively studied by time-of-flight spectroscopy following electron impact excitation. The technique involves the measurement of translational kinetic energy distributions of fragment atoms and molecules following dissociative excitation of a parent molecule. Excitation function measurements, where fragments of known kinetic energy are recorded as a function of incident electron energy, provide information on repulsive and predissociated states of the parent molecule and often lead to identification of the fragment states. In addition, angular distributions of fragments, with respect to the incident electron beam, provide information about parent molecule state symmetries.

Metastable atoms and molecules are of interest because of their involvement in atmospheric and laser physics. For example, a review of the major atomic and molecular processes taking place in the upper and middle atmosphere shows immediately the importance of certain metastable states of oxygen and nitrogen. In particular, metastable oxygen atoms ($O(^1D)$) are the result of photodissociation of molecular oxygen in the thermosphere following the absorption of ultraviolet radiation. At lower altitudes photodissociation of ozone during statospheric absorption of near ultraviolet radiation also produces these fragments. At higher altitudes the metastable states $O(^1S)$ and $O(^1D)$ in addition to the corresponding states of atomic nitrogen are produced via dissociative recombination of electrons and the molecular parents.

The importance of $O(^1D)$ is further emphasized by consideration of some of the major reactions which lead to the build-up and breakdown of the stratospheric ozone layer (Nicolet, 1974). For example, $O(^1D)$ forms an important source of atomic oxygen for ozone production (through 3-body reactions with $O_2$ and another molecule). In addition, it reacts with atmospheric $H_2O$ to produce the OH radical which attacks ozone.

Studies of the mechanisms involved in the production of the Earth's ozone layer have now taken on a new importance due to the threat of high altitude atmospheric pollution. In particular, fear has been expressed that increased concentrations of the oxides of nitrogen at these altitudes may upset the delicately balanced natural processes. Supersonic transporters and atmospheric nuclear tests are known to pollute the atmosphere in this way. Chlorine containing compounds such as the freons are also a major concern. Freon 11 ($CCl_3F$) and freon 12 ($CCl_2F_2$) are used extensively as refrigerants and and aerosol propellants. The only known atmospheric sink for these gases involves diffusion into the stratosphere where they undergo photodissociation,

$$CCl_3F + h\nu \longrightarrow CCl_2F + Cl \qquad (1)$$

$$CCl_2F_2 + h\nu \longrightarrow CClF_2 + Cl \qquad (2)$$

The chlorine atoms produced may then attack ozone in the following way

$$Cl + O_3 \longrightarrow ClO + O_2 \qquad (3)$$

$$ClO + O \longrightarrow Cl + O_2 \qquad (4)$$

$$\text{Net} \quad O_3 + O \longrightarrow 2O_2 \qquad (5)$$

The net result of the above reactions is the catalytic removal of ozone from the stratosphere.

Major processes involved in the Atmospheric Airglow also involve metastable atoms and molecules. In particular, emissions from metastable states of atomic oxygen are important. These are also parent states of some of the prominent auroral emissions (Chamberlain, 1961). Metastable species are prominent in other planetary atmospheres as well. Metastable $O(^1S)$ and $O(^1D)$ are strongly represented in the atmospheres of Mars and Venus, being produced by photodissociation of $CO_2$ and also dissociative recombination of $O_2^+$ and $CO_2^+$. The dayglow spectrum of Mars includes a variety of emission features of which the Cameron bands of metastable $CO(a^3\pi \rightarrow X^1\Sigma^+)$ are important (McConnell et al. 1970).

Population inversion in many laser systems involves metastable states and so any information regarding the production of these states is useful. For example, work is currently being undertaken on the feasibility of an oxygen atom laser using the 5577Å line of atomic oxygen. Photodissociation of nitrous oxide and carbon dioxide has been suggested as a method of obtaining the $O(^1S)$ metastable state for this purpose (Rockwood, 1973) (Murray et al. 1973).

The difficulties involved in unambiguously and directly monitoring metastable species have led workers to the development of time-of-flight spectroscopy. Metastable atoms and molecules, including Rydberg species, can be directly detected by Auger electron emission from metal surfaces of sufficiently low work function. In addition, atoms and molecules in Rydberg states, can be ionized by strong electric fields and the resulting ions directly detected by a mass spectrometer. The present work involves the development of special detectors based on both these techniques.

A detailed study of dissociation channels in carbon dioxide, nitrous oxide, freon 11 and freon 12 is presented in this dissertation. The metastable atoms and molecules produced by these dissociation channels were directly detected.

# CHAPTER 1

# THEORETICAL CONSIDERATIONS

## 1.1 The Franck-Condon Principle

An electron transition in a molecule can occur during electron impact, photon absorption or photon emission. The way in which the molecular nuclei behave during such a transition is summarized by the Franck-Condon principle. This principle states that, in an electron transition, the nuclear separation and velocity of relative nuclear motion alter only by a negligible amount. In other words, the transition takes place so quickly that the nuclei do not have time to move an appreciable distance. It is thus possible to predict the consequences of an electron transition by study of the potential energy curves of both the initial and final electronic states.

To illustrate this point, three possible transitions in a diatomic molecule AB are shown in Fig.1(a). In all three cases the transition takes place between a ground state potential energy curve and an upper state potential energy curve. The upper state curves do, however, differ in shape and may correspond to the excited states of either a molecule or molecular ion. The nuclear separation in the ground vibrational level will effectively lie between the limits a and b in all cases. Hence, according to the Franck-Condon principle, the nuclear separation still lies between these limits after the transition. Referring to Fig. 1(a), the final

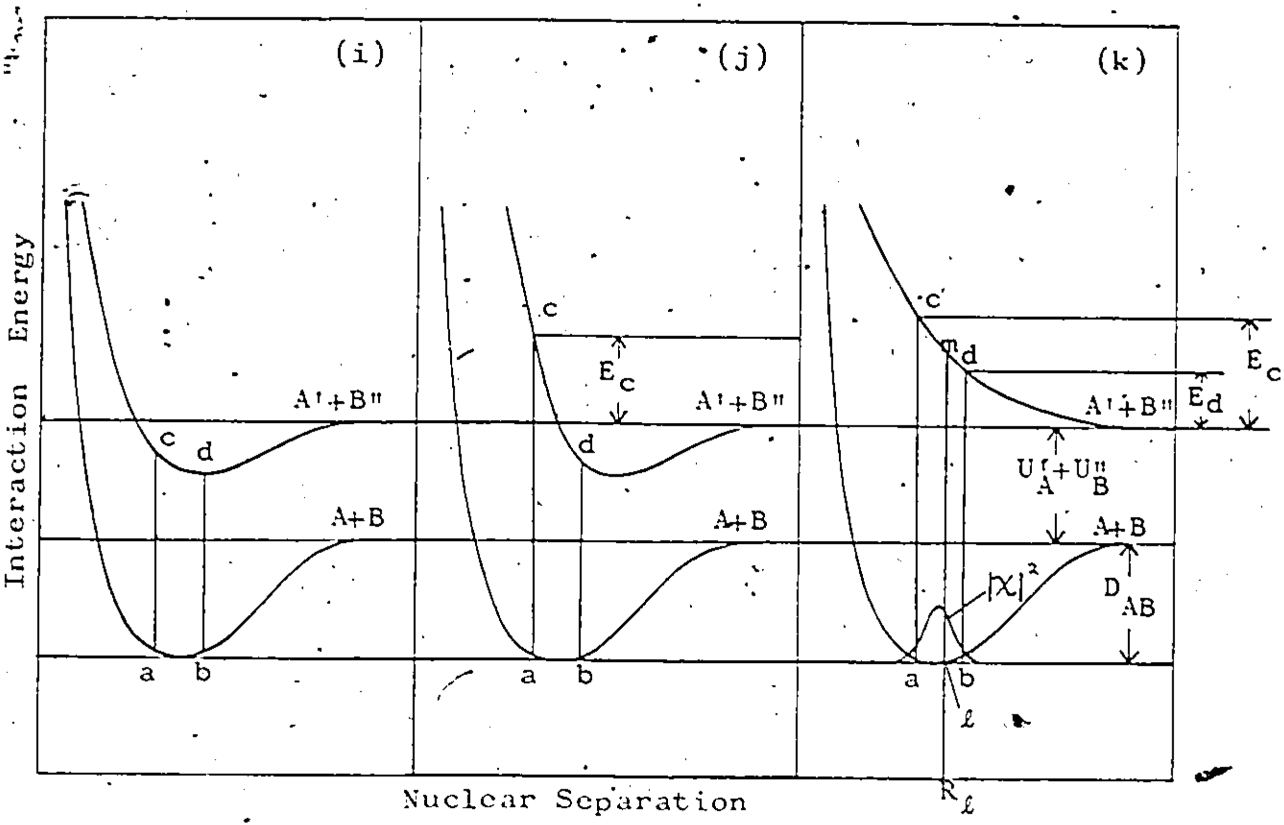

Fig. 1(a) Electronic transitions in molecules from a given initial state to three final states having different potential energy curves, illustrating the consequences of the Franck-Condon principle.

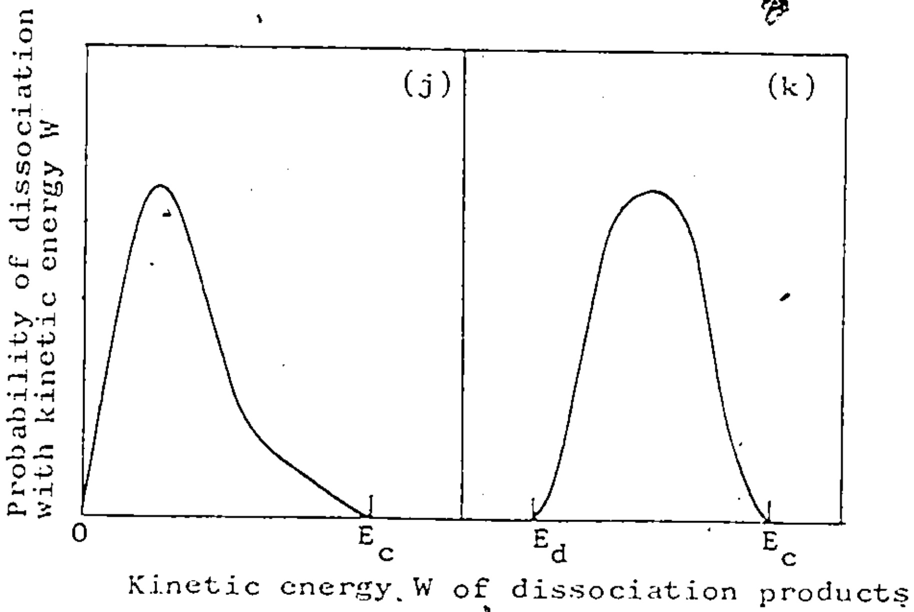

Fig. 1(b) Two possible kinetic energy distributions of products of dissociation by electron impact.

state of the molecule will therefore be represented by points lying between c and d on the upper curves. The three cases that are illustrated thus result in the following consequences.

Case (i) The final state always lies within the region of the discrete vibrational levels of the upper potential energy curve and thus the transition always results in a stable electronically excited molecule (or molecular ion) possessing some degree of vibrational excitation.

Case (j) The region in which the final state must lie includes some part of the continuum as well as some discrete vibrational levels. A certain proportion of the transitions will therefore lead to dissociation of the molecule (or molecular ion) while others will produce stable excited molecules (or molecular ions). During the dissociation the molecule (or molecular ion) splits into two atoms A' and B" (or an atom and an ion) with relative kinetic energies ranging from 0 to $E_c$ as shown in Figs.1(a)j and 1(b)j.

Case (k) The final state always lies within the continuum of vibrational levels. In this case, dissociation of the molecule (or molecular ion) accompanies all transitions between the lower and upper electronic states. The relative kinetic energies of the atoms (or atom and ion) into which the molecule (or molecular ion) dissociates will lie between $E_d$ and $E_c$ as shown in Figs.1(a)k and 1(b)k.

The atoms produced during the dissociation of a molecule (or molecular ion) may either be in electronically excited states or in the ground state. This depends entirely on the dissociation limit of the particular molecular (or molecular ion) parent state. In a similar way, the dissociation limit of a molecular ion state may correspond to the production of excited or ground state atomic ions.

Similar considerations to the above apply to downward transitions in a molecule. These transitions may also result in the production of a stable molecule or lead to molecular dissociation, depending on the nature of the potential energy curve for the lower state and the nuclear separation involved.

Some of the excited molecular states, produced by electron impact, may be metastable and the dissociation of others may result in metastable fragments.

## 1.2 Dissociation Energetics

Consider a transition from the ground state of a diatomic molecule AB to an upper electronic state of the molecule. Take as the zero of potential energy the energy of the ground vibrational level of the ground state. Let $D_{AB}$ be the dissociation energy of AB and $W_{min}$ the minimum energy of relative motion of the atoms A' and B" after the dissociation. Thus, if $U_A'$ and $U_B''$ are the excitation energies of these atoms, then according to the Franck-Condon principle, the minimum energy $E_{min}$ necessary to produce the transition is given by

$$E_{min} = U'_A + U''_B + W_{min} + D_{AB} \qquad (6)$$

as may be seen from Fig.1(a)k in which $W_{min} = E_d$. A more general expression than the above is given by

$$E = U'_A + U''_B + W + D_{AB} = D'_{AB} + W \qquad (7)$$

where E is now the energy required to produce a transition anywhere within the Franck-Condon region, W is the resulting kinetic energy of the relative motion of A' and B" and $D'_{AB}$ is the dissociation limit of the excited molecule.

The importance of Eq. (7) lies in the fact that it may be possible to obtain information about $D'_{AB}$ or the nature of the products A' and B" by measuring E and W. In any such measurement it is usually only possible to determine the kinetic energy of one of the fragments. However, given this information and the necessary condition of momentum conservation, it follows that

$$W = \frac{M_{AB}}{M_A} W_B \qquad (8)$$

where $W_B$ is the measured kinetic energy of B", $M_{AB}$ is the mass of the molecule and $M_A$ is the mass of fragment A'.

The kinetic energy $W_B$ of fragment B" can be determined, assuming its mass is known, by measuring the fragments transit time over a known distance. This is exactly what is done during time-of-flight spectroscopy.

In an electronic transition that can lead to dissociation, the resulting atoms may have a finite range of relative kinetic energies. It is of interest and importance to have some means of estimating the probability that a given fragment will have a particular energy in this range. This probability is a reflection of the probability that the nuclear separation should have a particular value in the classically allowed range. Thus, referring to Fig. 1(a)k, the probability that a transition be from $\ell$ to m is determined mainly by the probability that the nuclear separation of the initial state be $R_\ell$. This probability is given by the value of $|\chi_{no}(R_\ell)|^2$, where $\chi_{no}$ is the vibrational wave function of the lowest vibrational state. The distribution of this probability as a function of $R_\ell$ is shown in Fig. 1(a)k. The probability reaches a single maximum at about the centre of the Franck-Condon region and falls off rapidly outside the region of classically allowed motion. Using this function as a weighting factor, the energy distributions of the atoms resulting from transitions of respective types (j) and (k) take the forms illustrated in Fig. 1(b). There is a characteristic difference between these two energy distributions. In the former case, illustrated in Fig. 1(b)j, atoms with zero kinetic energy may be produced and the curve falls off quite sharply at the low energy side, whereas in case (k), illustrated in Fig. 1(b)k, the atoms always have some finite kinetic energy and the curve remains nearly symmetrical.

Thus it is possible, in principle, to distinguish between the dissociation of molecules in repulsive states (such as in Fig.1(a)k ) and the dissociation of molecules in bound states (such as in Fig.1(a)j ).

## 1.3 The Importance of Excitation Functions in the Study of Metastable Atoms and Molecules

### 1.3.1 The General Shape of Excitation Functions

Excitation functions, which are recordings of signal intensity against electron energy, have a characteristic high energy dependence which depends on the specific excitation mechanism being studied. In the present experiment, this signal intensity corresponds to the signal intensity of directly detected metastable atoms and molecules and its high energy dependence is a reflection of the behaviour of the cross-section for metastable excitation at high energy. If the excitation involves only optically forbidden transitions (e.g. the excitation of molecular metastable states), then according to the first Born approximation, the high energy cross-section for excitation of all these states falls off as the reciprocal of the incident electron energy E. However, if a study is made of the metastable fragments produced during the dissociation of optically allowed molecular states, then according to the same approximation, the high energy cross-section for production of all these fragments falls off as $E^{-1} \ln CE$, where C is a constant. Furthermore, if any of the above excitations involve electron exchange (i.e. a change of multiplicity between the initial and final states of the molecule), then according to Ochkur approximation, the high energy cross-section for excitation of that particular state falls off as $E^{-3}$.

In the present work, a number of different excitation mechanisms contribute signal to each excitation function and thus analysis of the high energy behaviour is rarely meaningful. However, the energy at which an excitation function reaches a maximum also serves as a useful indication of the nature of the predominant excitation mechanisms. For example, an excitation function which reaches a maximum near threshold indicates the presence of at least one exchange process. In contrast, an optically allowed process normally reaches a maximum at about 4 to 5 times the energy of threshold.

### 1.3.2 The Detailed Structure of Excitation Functions

Consider an excitation function obtained by plotting the signal intensity of metastable molecules against electron energy. If the electron energy is less than the excitation energy of the lowest molecular metastable state, then zero signal will be observed. This remains the case until the electron energy is sufficient to cause a transition from the ground state of the molecule to the first accessible vibrational level of the metastable state. At this point the first signal will be observed and it continues to increase in magnitude as the cross-section for excitation of the vibrational level increases. If the incident electron beam is sufficiently monoenergetic and high resolution detection is possible, then it ~~may~~ be possible to observe the excitation of different vibrational levels in the metastable molecule. The excitation of each of these levels would then cause an increase in the observed signal and hence a change in slope of the excitation function. However, poor resolution usually prevents such detailed observations and thus the total signal due to excitation of the metastable electronic state rises smoothly as the cross-section for its excitation increases. This continues until the electron energy is sufficient to excite the next molecular metastable state. At this energy an observable change in the slope of the excitation function occurs. It is thus possible to measure the minimum energy required to excite the molecule from its ground state to each molecular metastable state (i.e. the metastable state excitation energies).

In a similar way, it is possible to measure the dissociation limit of the excited states which result in metastable fragments. This is done by recording an excitation function in which only metastable fragments of known kinetic energy are recorded. Such an excitation function enables the electron energy to be measured at the first appearance of fragments from each dissociation process. It then follows from Eq. (7) that the dissociation limit $D'_{AB}$ of each of the molecular parent states is given by

$$D'_{AB} = E_{APP.} - W \qquad (9)$$

where $E_{APP.}$ (appearance potential) is the electron energy at fragment appearance and W is the kinetic energy of relative motion of the dissociation fragments.

Since the kinetic energy of only one of the dissociation fragments is measured, it is convenient to substitute for W in the above equation using the expression given in Eq. (8). Rearrangement of the resulting expression gives

$$W_B = \frac{M_A}{M_{AB}} (E_{APP.} - D'_{AB}) \ . \qquad (10)$$

This is the equation of a straight line of slope $\frac{M_A}{M_{AB}}$ and appearance potential intercept $D'_{AB}$. It follows that a plot of fragment kinetic energy against appearance potential yields $D'_{AB}$ directly. It also follows from Eq. (7) that

$$D'_{AB} = U'_A + U''_B + D_{AB} \qquad (11)$$

where $U'_A$ and $U''_B$ are the excitation energies of the fragments and $D_{AB}$ is the dissociation limit of the ground state of the molecule AB. Thus, if $D_{AB}$ is known, it may be possible to identify the excited states of the fragments. This is done by comparing the measured value of $D'_{AB}$ with dissociation limits which are calculated by combining different values of $U'_A$ and $U''_B$.

Knowledge of $D'_{AB}$ and the various appearance potentials enables the position of a molecular parent state, on a potential energy diagram, to be determined and also provides qualitative information about its shape. In addition, angular distributions of dissociation fragments, with respect to the incident electron beam, provide information about the symmetry of the molecular parent state (Dunn, 1962; Zare, 1967). A detailed discussion of this technique has been previously presented (Allcock, 1975).

## 1.4 Fragment Mass Identification and the Dissociation of Polyatomic Molecules

So far in the analysis it has been assumed that the mass of the detected fragment is a known quantity. This may not be the case if the dissociating molecule is a polyatomic or a heteronuclear diatomic. The problem may be overcome for heteronuclear diatomic molecules if the masses of the constituent atoms are sufficiently different. The key to fragment identification in such a case is a plot of fragment kinetic energy against appearance potential where the detected fragment is assumed to have any convenient mass m. If the actual mass of the detected fragment is $M_B$, it follows from Eq. (10) that the line obtained by plotting $W_m$ (fragment K.E. assuming mass m) against $E_{APP.}$ is given by

$$W_m = \frac{m}{M_B} \cdot \frac{M_A}{M_{AB}} \left[ E_{APP.} - D'_{AB} \right] \qquad (12)$$

The slope of this line is characteristic of the actual mass of the detected fragment. If $M_B$ is sufficiently different from $M_A$, the slope of the above line will be significantly different from the slope of the line obtained by detecting fragments of mass $M_A$. The slope obtained for fragments of mass $M_A$ is $m \cdot M_B/(M_{AB} \cdot M_A)$. Thus, a plot of $W_m$ against $E_{APP.}$ is a useful first step towards fragment identification. In many cases such identification is not possible by other means.

Two-fragment dissociation processes in polyatomic molecules may also occur. The molecular fragments produced in such a case may possess rotational and vibrational energy in addition to being electronically excited. The energy previously available for translation of the fragments (i.e. $E_{APP.} - D'_{AB}$) must now be partitioned between translation rotation and vibration. In general, this partitioning will depend on the path of dissociation. This is illustrated in Fig. 2 where a schematic potential energy diagram for an excited state of $CO_2$ is shown. For motion along the symmetry axis, the potential energy surfaces of a linear triatomic molecule may be visualized in three dimensional space (see Herzberg, 1966). The motion of a small mass moving without friction on such a surface represents the motions of the atoms in the molecule. Fig. 2 shows an excitation from the ground state of $CO_2$ to a point Y on the

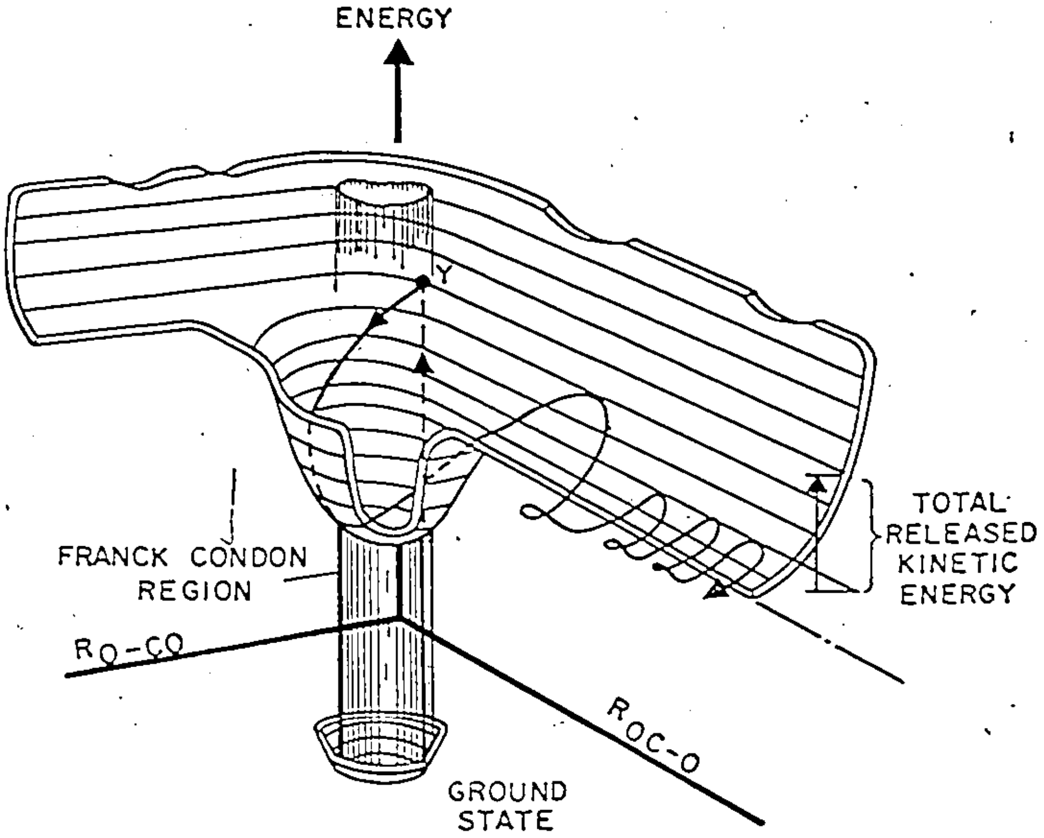

Fig. 2 An electron transition in a linear triatomic molecule ($CO_2$) leading to a two-fragment dissociation in which the molecular fragment is vibrationally excited.

repulsive wall of an excited state. A small mass leaving point Y would undergo a complicated Lissajous motion as it passes through the potential well and into the valley leading to dissociation into O and CO. The CO fragment would be vibrationally excited as indicated by the oscillations which stretch and compress the O-C bond. Clearly, for a given value of $E_{APP.}$ (i.e. fixed height above the ground state) different fractions of the available energy can go into vibration of the CO fragment and hence the detected fragment can be produced with different amounts of kinetic energy. This depends on where in the Franck-Condon region the transition takes place and on the local shape of the potential surface. If the exit channel can be reached by different paths, the energy sharing may be different in each case and thus each path can lead to a different dissociation limit. The limits being given by

$$D'_{AB} = U'_A + U''_B + D_{AB} + \eta \qquad (13)$$

where $U'_A$ and $U''_B$ are the electronic excitation energies of the fragments, $D_{AB}$ is the dissociation limit of the ground state of the parent molecule (i.e. the energy required to break the bond between fragments A and B) and $\eta$ includes the vibrational and rotational energy of the molecular fragments. It should be noted, however, that this variable partitioning of energy will not be apparent at high appearance potentials on a plot of $W_m$ against $E_{APP.}$, provided that a significant fraction of the fragment molecules are produced with little or no vibrational energy. Clearly, it is these molecules or their dissociation partners which will be detected first in an excitation function [N.B. for fixed kinetic energy, $E_{APP.}$ has a minimum when $D'_{AB}$ has a minimum (see Eq. (9))]. Thus, the plot of $W_m$ against $E_{APP.}$ will obey Eq. (12) at high appearance potentials and the measured value of $D'_{AB}$ will correspond to that given by Eq. (13) with $\eta = 0$. In such a situation, slope analysis may again result in identification of the mass of the detected fragment. The variable partitioning of energy will only become apparent for excitations at the outer edge of the Franck-Condon region and then only in situations where the excited state remains sufficiently repulsive. Here the appearance potentials reach a minimum in accordance with the Franck-Condon principle and the production of fragments with various kinetic energies at a fixed appearance potential can no longer be obscured. At this appearance potential the data points will depart from the above line and appear to lie on a line of infinite slope. Such a behaviour has been reported by Schiavone et al. (1977) during a study of hydrogen-Rydberg production from $CH_4$ and $C_2H_6$. However, these workers also observed the preferential population of higher and higher vibrational states of the molecular fragments as the appearance potential increased. In their study of two-fragment dissociation processes, the data points in question did not follow lines given by Eq. (12), but appeared to lie on lines of lower slope. Appell and Kubach (1971) also observed the production of fragments ($H^+$) with various kinetic energies at a fixed appearance potential during a similar study of $CH_4$. In the present work, Eq. (12) was found to adequately describe all the dissociation processes where the data points were observed to follow lines of finite slope. This indicates that either a fixed amount of energy was being partitioned into vibration of the molecular fragments or that a large fraction of the molecular fragments were being produced with little or no vibrational energy. The second possibility was verified in all cases where the electronic excitation energies of the fragments were unambiguously known.

Multiple fragmentation processes in polyatomic molecules involve the production of more than two fragments. If the fragments are produced isotropically (i.e. no symmetry restrictions exist) during a one-step dissociation of the parent molecule, then partitioning of the available kinetic energy is no longer constrained by the conservation of momentum and energy. In such a situation the detected fragment will be produced with a range of kinetic energies as soon as the fragmentation is energetically possible. Excitation function measurements on such processes will indicate the production of fragments with various kinetic energies, but with the same appearance potential. Little information can be obtained about such fragmentation processes since the total kinetic energy released during the dissociation remains an unknown.

It should be noted that an autoionization of an excited state of the parent molecule may also produce the above effect since in such a case the outgoing electron may possess variable amounts of kinetic energy (see Chapter 5).

In the present experiment the Rydberg fragments produced during the various dissociation processes could be directly identified using a special Rydberg detector coupled to a quadrupole mass spectrometer.

## 1.5 The Direct Detection of Metastable Atoms and Molecules

Metastable atoms and molecules, including Rydberg species, may be directly detected by monitoring the Auger ejection of electrons from a metal surface upon which the fragments impinge. In order to be detected the fragments must retain their excitation energy during the flight from the electron gun to the detector (i.e. the excited states must have sufficiently long lifetimes). The Auger transitions in which the electrons are released do not involve directly the translational energy of the incoming particles. A detailed theoretical account of the Auger de-excitation of metastable atoms at such a surface has been given by Hagstrum (1954). The excitation energy of the incident particle is used to eject an electron from the conduction band of the metal. If this excitation energy is greater than the work-function of the metal then the electron may escape from the surface. An entirely equivalent process is the radiationless transition of an electron from the conduction band of the metal to the ground state of the atom followed by ejection of the excited atomic electron. Hagstrum points out that the Auger emission takes place as the incident particle approaches the surface and that it occurs in a time period which is much shorter than typical radiative lifetimes (i e. shorter than $10^{-8}$ sec).

A high-Rydberg state in an atom or molecule is a state which possesses such a large principal quantum number that the average distance $\langle r \rangle$, from the nucleus to the electron, is large. In such a case, the core ion of the atom or molecule can be approximated to a point charge and thus the high-Rydberg electron behaves in a similar way to a hydrogenic electron. Atoms and molecules in high-Rydberg states retain their excitation energy because the radiative lifetime of a state of fixed angular momentum $\ell$ increases as $n^3$ where n is the principal quantum number. Smyth et al. (1973) present a table which shows the variation of additional properties of high-Rydberg states with this quantum number. Atoms in Rydberg states may be ionized by a sufficiently strong electric field and hence directly detected. The effect of such a field is to lower the ionization potential of the atom. It is easy to show by a semi-classical calculation that the electric field $E_o$ required to ionize an atom in a Rydberg state of effective quantum number $\nu$ is given by

$$E_o = \frac{1}{Z}\left[\frac{Z}{2\nu}\right]^4 \tag{14}$$

where the electric field is in atomic units and Z is the atomic number of the atom. Since the Rydberg electron spends most of its time at a large distance $\langle r \rangle$ from the core-ion of the atom, Z is effectively unity for large values of $\nu$. In the present experiment, the electric field used to ionize the Rydberg fragments had a typical value of 6000 volts/cm. The above equation indicates that this field would ionize Rydberg atoms with quantum numbers greater than $\nu = 15$. The corresponding binding energies of the Rydberg electrons would be less than 0.06 eV.

During a dissociation process, Rydberg atoms may be produced which have excited core ions. Many of these atoms would autoionize before reaching the detector. However, in some cases autoionization is strongly forbidden by selection rules and the autoionization lifetime may be as long as 100 $\mu$s (Kuhn, 1969). Therefore, it is not possible to rule out the detection of such fragments in a time-of-flight experiment. A number of the dissociation processes identified in $N_2O$ (see Chapter 5) appear to produce Rydberg atoms of this kind.

## 1.6 The Core-Ion Model for the Dissociation of Molecules in Rydberg States

Molecules which have been excited to high-Rydberg states may produce atoms in Rydberg states during a dissociation process. The energy of a high-Rydberg molecule, as a function of its internuclear distance, is given by the electronic states of the core ion, lowered only by the very small binding energy of the high-Rydberg electron. Potential energy curves of the high-Rydberg molecule are thus parallel to those of the core ion and lie less than 0.1 eV lower in energy. The model therefore predicts that the dissociation of a high-Rydberg molecule is governed entirely by the potential energy curves of the core ion. This remains the case until the distance between the separating nuclei becomes comparable to ⟨r⟩. Until this time, the Rydberg electron has merely been a spectator to the dissociation process. As the nuclei separate, it is hypothesized that the Rydberg electron is most likely to remain bound to the ionic dissociation fragment in a high-Rydberg orbital. The kinetic energy of this high-Rydberg atom is, however, the kinetic energy acquired by the atomic ion during the dissociation of the molecular core ion. The Rydberg electron's mass and binding energy have little effect on the dissociation process. In addition, the threshold for the dissociation process should lie below the corresponding dissociative ionization threshold by only the small binding energy of the high-Rydberg electron.

# CHAPTER 2

## EXPERIMENTAL CONSIDERATIONS

## 2.1 Introduction

A detailed account of the experimental arrangement and its associated data accumulation systems has been previously presented (Allcock, 1975). Since this presentation, a number of major modifications have been made to the apparatus and to the data storage facilities. The most important of these modifications was the addition of a mass sensitive Rydberg detector to the apparatus. A gas beam was also added. A brief description of the present experimental arrangement, including the modifications, is presented in the following account. For clarity, a review of the whole experiment is presented before these considerations.

## 2.2 A Review of the Experiment

The time-of-flight experiment involved exciting the molecules of a gas beam target, with a pulse of approximately monoenergetic electrons and then recording the resulting fragment signal as a function of its arrival time at an Auger detector. This technique enabled photons, fast atomic and molecular metastable fragments and thermal energy metastable molecules (using a diffuse-gas target) to be separately resolved in the time-of-flight spectrum. In addition, the use of a mass sensitive Rydberg detector enabled the Rydberg species to be positively identified. Only Rydberg fragments and fragments with sufficient internal energy to cause Auger electron emission from a special surface were detectable. Radiative decay from atoms and molecules in non-metastable states rendered them undetectable and the use of electric and magnetic fields prevented the detection of ions and electrons. During the flight to the Auger detector, radiative decay from certain metastable states also occurred and thus prevented the direct detection of some fragments. A typical time-of-flight spectrum, which was obtained during use of the Auger detector, is shown in Fig. 3.

The flight path from the electron beam to the Auger detector covered a distance of 41.3 ± 0.5 cm and careful measurement of fragment flight times, over this distance, enabled the corresponding fragment kinetic energies to be calculated. Where possible, a coordinate transformation was performed and the signal intensity was plotted as a function of fragment kinetic energy.

Excitation functions, which are recordings of signal intensity against electron energy at fixed time-of-flight, enabled the electron energy at fragment appearance (appearance potential) to be determined. Plots of fragment kinetic energy against appearance potential provided information about fragment mass and the dissociation limits of the fragment parent states (see Eq. (12) of Chapter 1).

Time-of-flight and excitation function data was also obtained during use of the Rydberg detector. This detector could be tuned to different fragment masses. The flight path from the electron beam to the Rydberg ionizer of this detector covered a distance of 20.5 ± 0.1 cm.

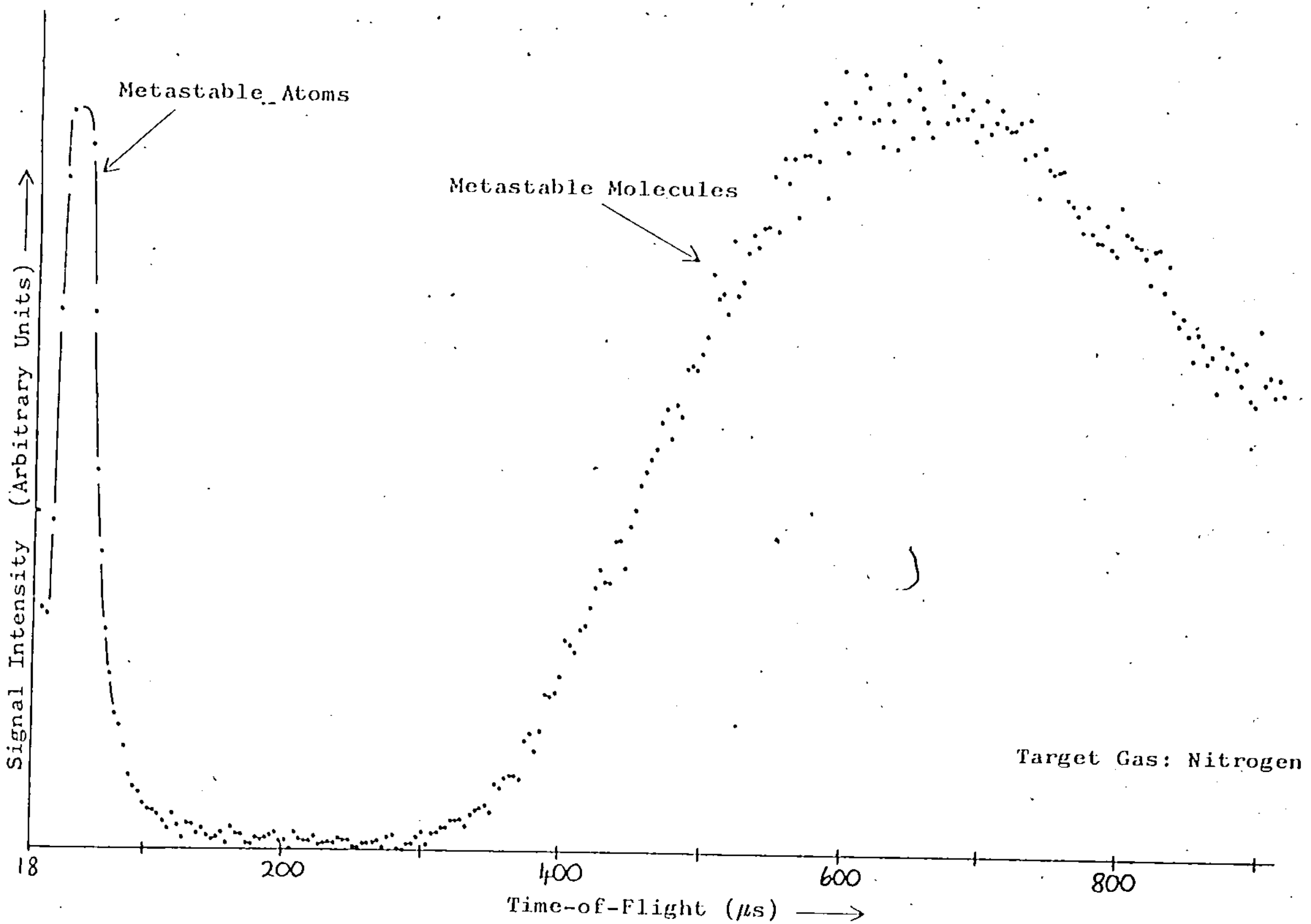

Fig. 3 A Typical Time-of-Flight Spectrum

Secondary processes such as the collision of an electron with more than one gas molecule and the collision of metastable fragments with parent gas molecules, were avoided by careful choice of both gas pressure and electron current. Plots of signal intensity, against the gas-beam head pressure and the electron current, were used in order to select the best operating conditions. These plots become non-linear if a significant number of secondary collisions take place.

## 2.3 Description of the Apparatus

The apparatus (Fig. 4) consisted of two differentially pumped vacuum chambers which were connected by a narrow bore tube through which the dissociation fragments could pass. In the smaller of the two chambers a magnetically focused electron gun (Fig. 5) was mounted between the poles of a large permanent magnet (800 gauss) in such a way that the magnetic field lines ran parallel to the electron beam direction. Three electrostatic focusing electrodes were also available. Electrons were accelerated from a negatively biased cathode to a grounded electrode and then entered the grounded interaction region. The electrons were collected in two concentric, cylindrical, Faraday cups which allowed beam dispersion to be monitored. To reduce any electron reflection, the outer cylinder was blackened with soot and the shielded inner cylinder biased a few volts positive. The normally inhibited electron beam was pulsed on by driving the first electrode from negative to positive, with respect to the cathode, and turned off by returning its

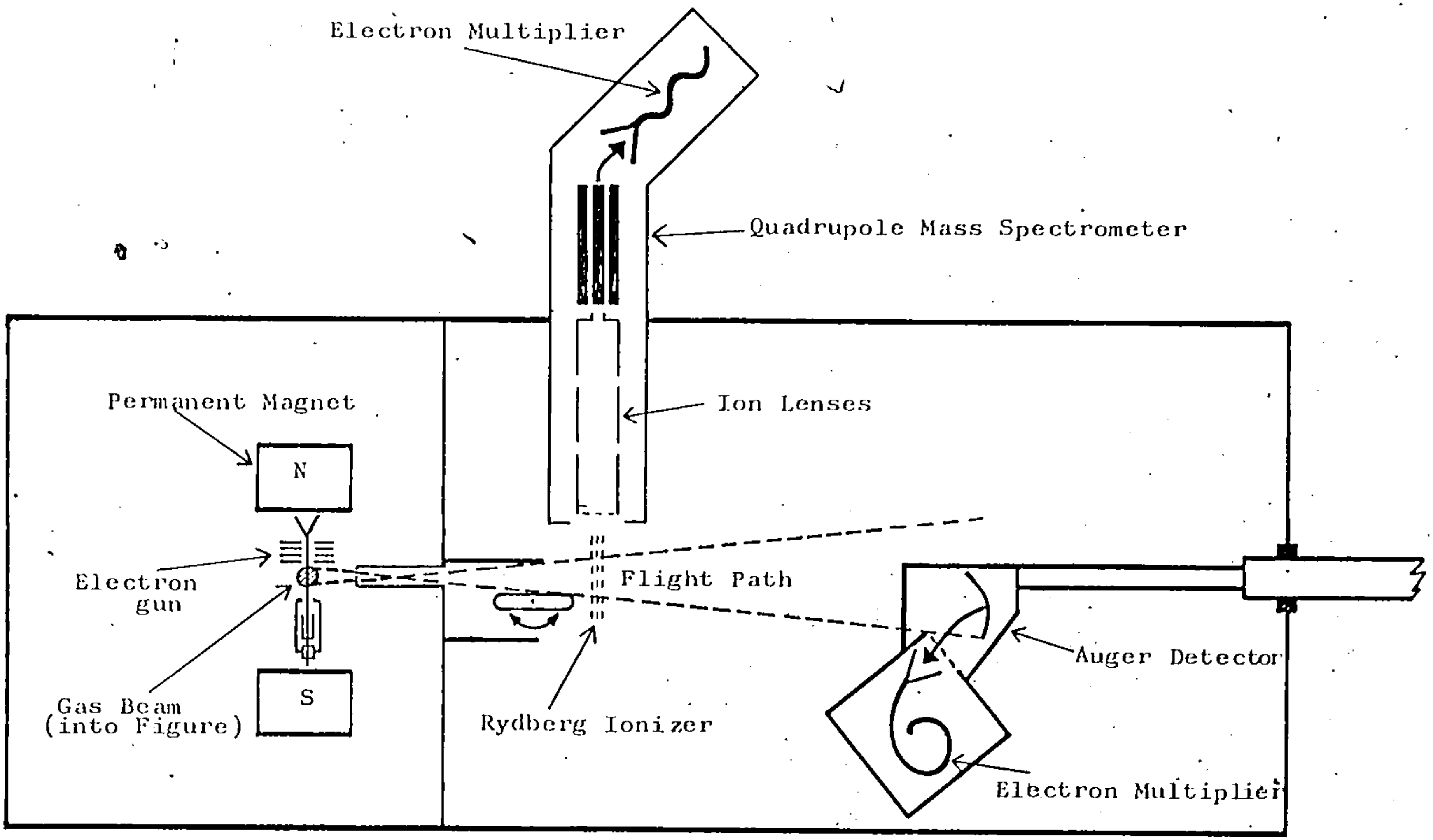

Fig. 4 Schematic of the Apparatus

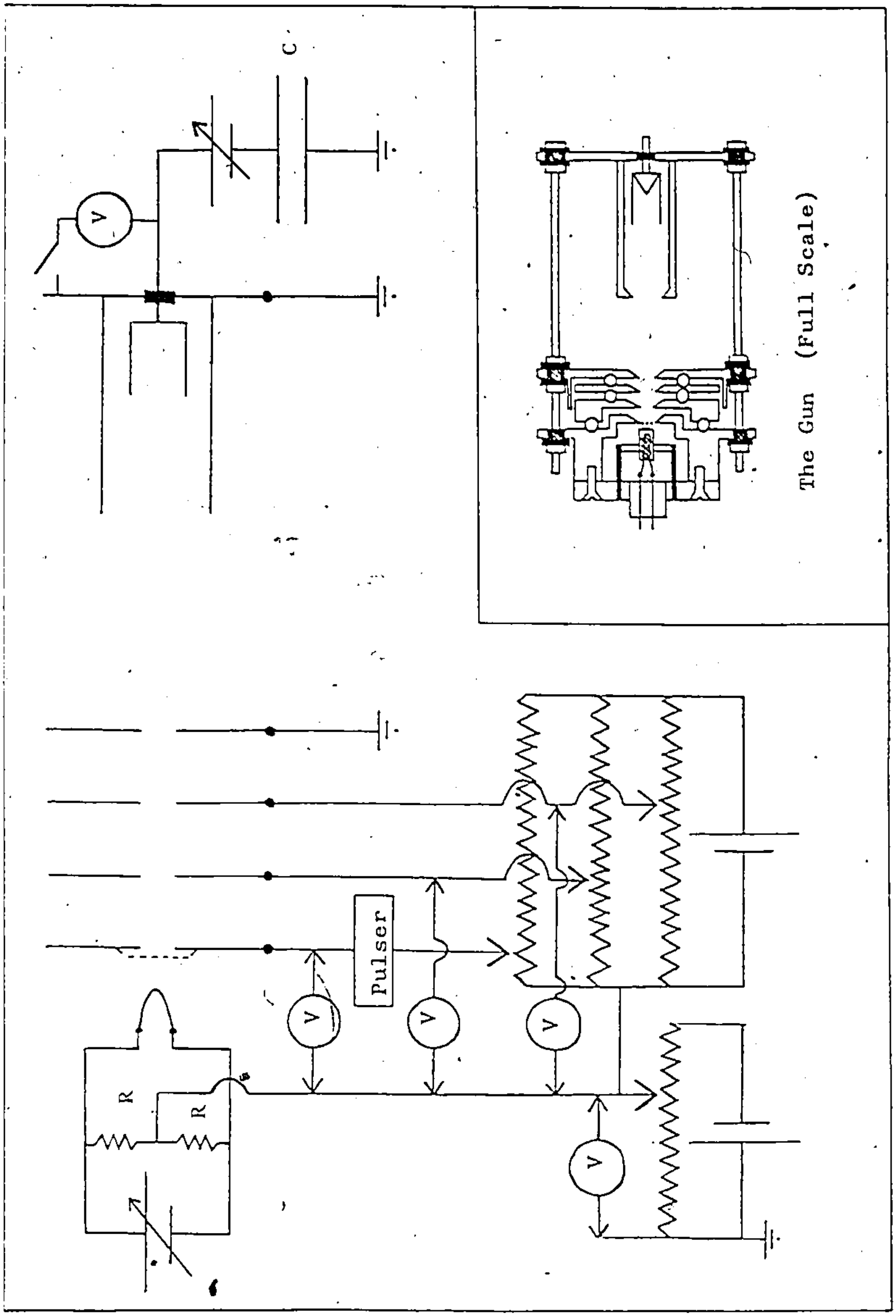

Fig. 5 The Electron Gun and Circuit

potential to the original negative value. The electron beam pulse duration could be varied between 1 and 10 $\mu$s with a repetition rate of usually 1000 Hz. Directly or indirectly heated cathodes could be mounted in the gun as required. Electrode location and spacing was by ruby balls and the gun was held together by three retaining rods. The shaped electrodes prevented insulator contamination while maintaining good pumping around the cathode. The electron beam was positioned in the same horizontal plane as the narrow bore tube which connected the two vacuum chambers.

A molecular beam was produced by passing gas molecules through a system of capillaries which was mounted above the electron gun interaction region. The molecular beam intersected the electron beam at right angles and the resulting metastable fragments could enter the detector chamber via a mutually orthogonal flight path. Charged particles were deflected from the beam of dissociation fragments by the strong magnetic field (cyclotron radius for a 5 eV $N^+$ ion was 1.5 cm). Electrostatic grids were also available for this purpose but were found to be unnecessary.

The larger vacuum chamber contained an Auger detector and a mass sensitive Rydberg detector (see Fig. 4). The Auger detector consisted of a special low work function surface from which Auger electrons could be ejected by metastable fragments and photons. The surface (Ag-O-Cs) was obtained by breaking open a photodiode tube in vacuum. The electrons ejected from this surface were first accelerated and then detected by a channeltron ✓

electron multiplier. The detector mount, which was constructed from copper, was attached to a cold finger to reduce the thermal emission of electrons from the freshly exposed surface. Cooling of the detector to liquid nitrogen temperatures became unnecessary after the surface became partially contaminated. The channeltron was partially shielded from stray magnetic fields by mounting it inside a conetic box and the ejected electrons were accelerated and directed into this box by a tungsten grid mounted at the entrance. Data pulses from the channeltron were passed to the counting circuitry by a high input/low output impedance preamplifier. The Auger detector was sensitive to metastable atoms and molecules, Rydberg fragments and photons.

During their flight to the Auger detector, the dissociation fragments passed through a system of three high transparency grids which could be used to ionize any Rydberg fragments present in the beam. This was done by applying a high voltage to the central element of the grid system. Large electric fields (~ 6 K.V./cm) were generated by this system since the outer grids were grounded and placed about 1 mm from the central element. The ions produced were extracted at right angles to the original beam direction and focused by three cylindrical lenses into a quadrupole mass spectrometer. The lens system was shielded from stray magnetic fields by a tube made from conetic material. After mass analysis the ions were detected by a channeltron electron multiplier. The time taken for the ions to travel down the lens system and through the mass spectrometer was subtracted from the measured flight time in order to calculate the kinetic energy of the Rydberg fragments. The flight time of the ions was determined by pulsing the Rydberg ionizer on and off with a pulse which was also used to start a Time-to-Amplitude Converter. The arrival of an ion at the detector provided a stop pulse and the output of the T.A.C. was taken as a measure of the required flight time. The electron beam was operated D.C. during this work. The central element of the Rydberg ionizer was grounded when the Auger detector was in use. The above system constituted the Rydberg detector.

## 2.4 The Apparatus Electronics and Data Accumulation Systems

### 2.4.1 The Electron Gun Pulsing Mode

The normally inhibited electron beam was pulsed on by driving the first electrode of the electron gun from negative to positive with respect to the cathode. A variable width pulse of suitable voltage for this purpose, was delivered by a triggered pulser approximately every millisecond. This low repetition rate allowed sufficient time between electron pulses for the low kinetic energy fragments to reach the detector. The pulser was triggered by the initial rise of a 2 $\mu s$ computer generated pulse. The accelerating potential and the other electrode voltages were supplied by two smoothed D.C. power supplies. The electron gun circuit is shown in Fig. 5.

During the pulsed operation of the electron gun the necessary current normalization proved difficult so a charge normalization technique was developed. This involved slowly charging a 150$\mu$F tantalum capacitor with charge from the gun collectors, until its voltage reached a small preset level. When this level was reached the capacitor was quickly discharged. This slow charging and quick discharging cycle was repeated throughout data taking and the number of complete chargings counted by a scaler. To accomplish this the voltage across the capacitor, which was measured and amplified by an electrometer, was used to switch on a Comparator circuit when it reached the preset level. This circuit then shorted out the capacitor and delivered a suitable pulse to the scaler for counting. The capacitor voltage was only allowed to reach a few millivolts in order to prevent it affecting the electron energy. The advantage of recording the total charge passed by the gun during data taking was that electron current instabilities could then be completely ignored. The main cause of these instabilities was cathode contamination which caused the electron current to gradually decrease with time. Small changes in electron current also occurred with changes in electron energy, but once again, normalizing with respect to charge removed the necessity for the current to remain stable.

### 2.4.2 Time-of-flight Data Accumulation

A time-of-flight spectrum was obtained by plotting fragment signal intensity against flight time at constant electron energy and constant gas pressure. The data was recorded automatically by placing the experiment on line to an interfaced PDP-8/E computer. The computer controlled interface delivered a triggering pulse to the electron gun pulser and then after a preset delay time accumulated data counts in one of two identical buffers. After a preset channel width time, the incoming data pulses were channeled into the other buffer and the total count in the first buffer deposited into the memory. On completion of the next time interval, the incoming data pulses were channeled to the now empty first buffer and the total count in the second buffer deposited in memory at a new address. This process enabled signal from dissociation fragments with a fixed range of flight times to be recorded at a particular memory address. Using this two buffer system, there was no loss of data during the time taken to deposit the buffer count into the 256 time channels. Upon completion of the 256 channel scan the data accumulation was terminated and after a further delay the electron gun was pulsed again. The gun repetition rate allowed sufficient time between electron pulses for the low kinetic energy fragments to reach the detector. The complete cycle was repeated with a frequency of usually 1000 Hz and data accumulation times varied from several hours to several days. Different time-of-flight spectra (e.g. spectra obtained at different electron energies) could be charge normalized to each other by accumulating data for the same number of chargings of the collector capacitor. A gate unit which cut off the signal to the interface, after a preset number of these chargings, automatically terminated data taking at the right time. The logic signal for this purpose was supplied by a scaler. This system of data accumulation is shown schematically in Fig. 6.

The displayed time-of-flight spectrum could be averaged and expanded as required. Background subtraction and count integration were also available options. The time-of-flight spectrum could be reproduced on paper using a point plot routine and the data could be recorded on magnetic tape or punched onto paper tape for storage.

As the computer was not located in the same room as the experiment, it was necessary to amplify and discriminate the incoming data pulses at the interface location as well as at the experiment.

The maximum time resolution possible using this data taking system was limited by the speed at which the PDP-8/E could carry out instructions. In practice, this limit was 2.5 $\mu$s (two instructions). The time limit was utilized to best advantage by the addition of hardware which permitted direct access to the computer memory.

Fig. 6 Experimental Arrangement for Time-of-Flight and Excitation Function Data Accumulation

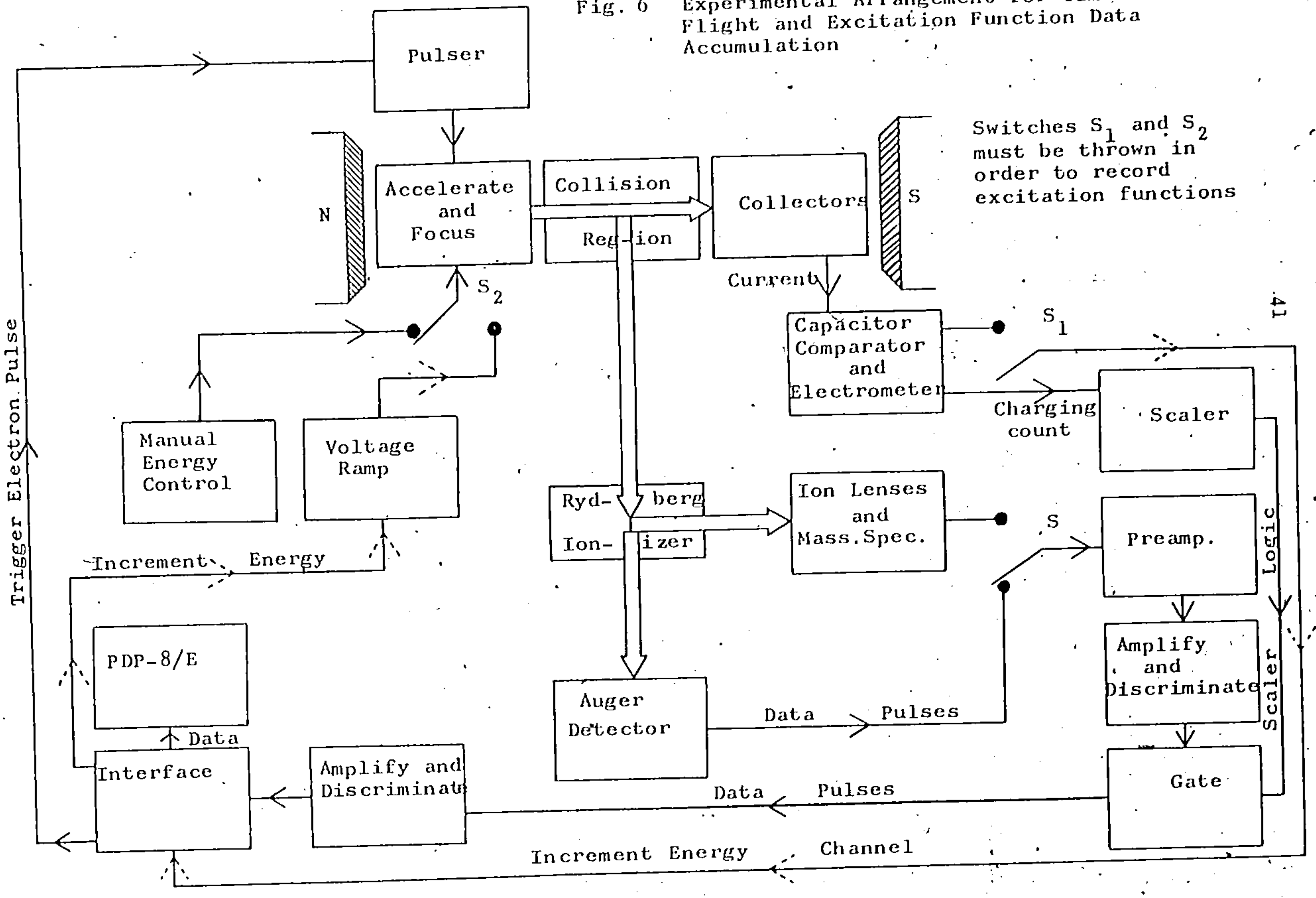

Switches $S_1$ and $S_2$ must be thrown in order to record excitation functions

### 2.4.3 Excitation Function Data Accumulation

An excitation function was obtained by plotting fragment signal intensity against electron energy at constant time-of-flight and constant gas pressure. A number of excitation functions, each corresponding to a different time-of-flight, were recorded automatically by placing the experiment on line to the interfaced PDP-8/E computer. The excitation functions were obtained by recording time-of-flight spectra at 256 different electron energies. Each spectrum was recorded during one complete charging of the collector capacitor. Upon completion of the charging cycle, the count recorded in selected time windows was stored in the computer memory and the electron energy was incremented by a preset amount. A new time-of-flight spectrum was then recorded and the count in each of the selected time windows stored at a new memory address. This process was repeated throughout the electron energy scan. Upon completion of the scan, the data corresponding to each recorded time window could be displayed as a function of electron energy. Alternatively, the energy scan could be continually repeated in order to improve statistics. Using the above system, 48 different excitation functions could be recorded simultaneously. Changes in the electron current, at different electron energies, had no effect on the excitation functions since the time-of-flight spectra were charge normalized to each other.

A voltage from the computer was used to ramp the electron energy through the required range. This voltage was amplified by a D.C. power supply. Data storage and the change in electron energy was initiated by a pulse from the Comparator circuit at the end of each charging cycle. The pulse switched on a computer interrupt which was serviced upon completion of the current time-of-flight scan. The above system of data accumulation is shown schematically in Fig. 6.

The displayed excitation functions could be reproduced on paper using a point plot routine and the data could be recorded on magnetic tape or punched onto paper tape for storage.

## 2.5 Apparatus Performance

### 2.5.1 The Electron Gun Performance

The electron gun was carefully tested before performing the experiment. A detailed account of the tests involved and the electron gun performance has been previously presented (Allcock, 1975). The tests included a check on the electron energy spread, contact potential shifts, electron collection efficiency, beam dispersion and the electron pulse profile. The electron gun was found to perform extremely well during all the tests.

The contact potential shifts were monitored by recording an excitation function for the production of helium atoms in the 2 $^3S_1$ metastable state. This process is particularly suitable for calibration purposes since its excitation cross-section can be approximated to a step function. This step function rises steeply at an excitation threshold of 19.81 eV (Pichanick, 1968). This excitation threshold can be used to calibrate the incident electron energy scale. Furthermore, comparison of the experimentally obtained excitation function, with its expected step function behaviour, enables an estimate to be made of the spread in incident electron energy. Contact potential shifts of 0.1 eV were commonly found and the electron energy spread was typically 1 eV (F.W.H.M.). A typical He$^*$ excitation function is shown in Fig. 7.

Space charge effects were also observed at high electron currents. These effects resulted in an upward shift in the appearance potential of the 2 $^3S_1$ metastable state and also resulted in an increased spread in electron energy (Heddle, 1967). The absence of positive ions in the vicinity of the electron beam allowed this shift to be observed in helium. The effect is significantly reduced at electron energies where positive ion production competes with space charge production. Despite this, the electron current was reduced to a level where the space charge shift became negligible before proceeding with

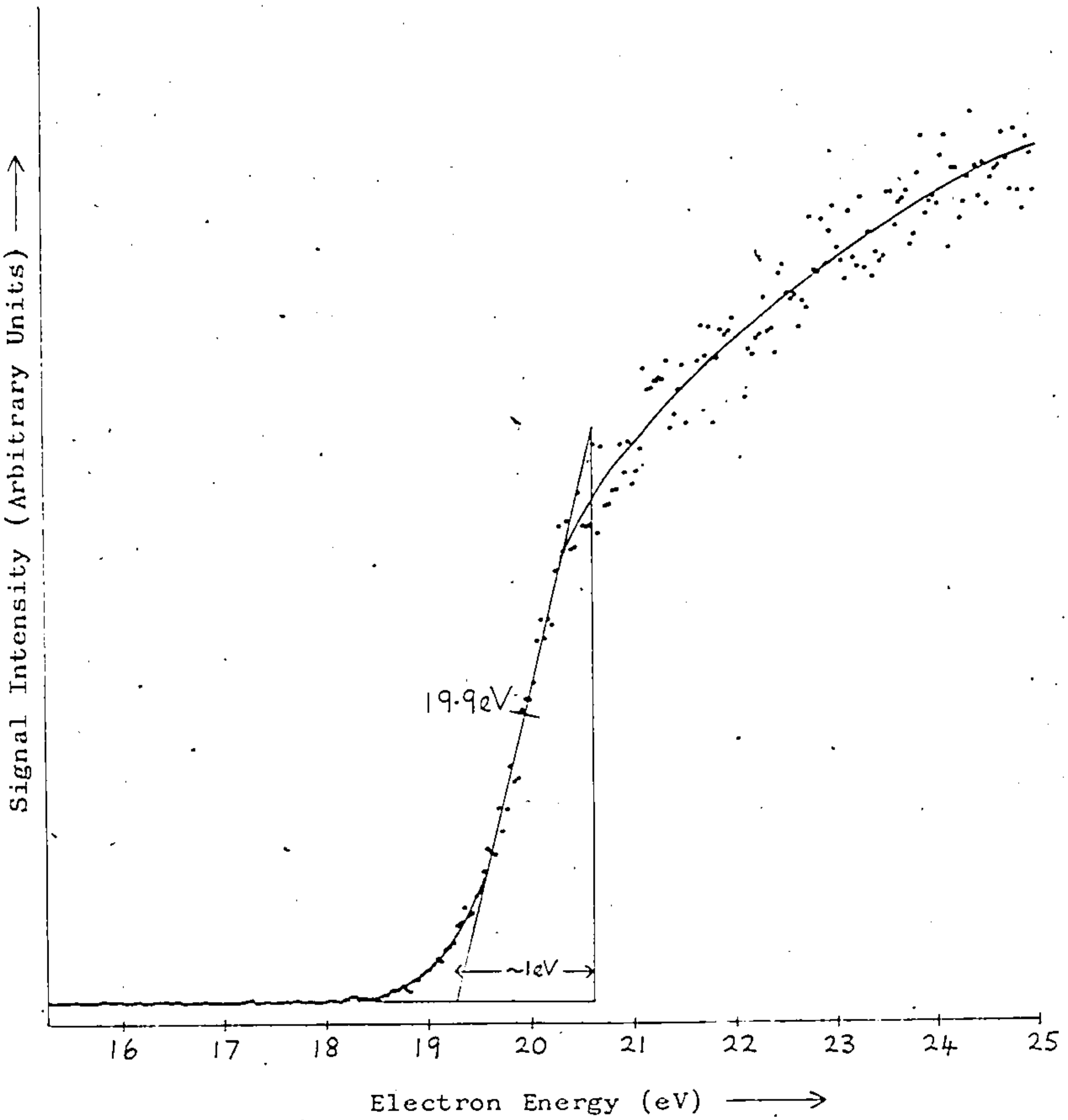

Fig. 7

A typical $He^*$ excitation function

the experiment. Any remaining appearance potential shift was then attributed to contact potentials. Occasionally, it became necessary to operate the electron gun at higher electron currents in order to obtain sufficient signal intensity from the gas being studied. In such cases, the appearance potentials obtained for the strongest signal producing processes were compared at low and high electron currents. Usually, the appearance potentials were found to agree at all but the lowest electron energies. This was taken as an indication that space charge effects were negligible.

### 2.5.2 Detector Performance

The low work-function surface of the Auger detector was obtained by removing the glass envelope from a photodiode tube in vacuum. This was done by rapidly heating a tungsten wire which surrounded the scratch-weakened envelope. The envelope then fell with the aid of weights, from the inverted photodiode, into a stainless-steel cradle in the bottom of the vacuum chamber. Contamination of the low work-function surface began upon removal of the envelope. This contamination gradually reduced the sensitivity of the Auger detector to metastable fragments of low excitation energy. Unfortunately, little quantitative information is available about the working lifetime of this detector. However, for a period of several weeks, the surface did remain sensitive to photons entering the chamber through a glass window (i.e. $\lambda > 3800Å$). This result suggests that the working lifetime of such a detector is quite long. Furthermore, it was discovered that a brief exposure to the atmosphere had little effect on this behaviour. Repeated exposure did, however, result in a loss of sensitivity to low energy photons. Despite this, it is likely that a completely contaminated photodiode surface remains more sensitive to low energy metastable fragments than a similar Cu/Be surface. After some initial problems with the thermal emission of electrons from the freshly exposed surface, the Auger detector was found to perform extremely well.

Despite two major problems, the mass sensitive Rydberg detector was also found to perform extremely well. The first of these problems was one of detector efficiency. During development of the Rydberg detector a channeltron was temporarily mounted in the vicinity of the Rydberg ionizer in order to check on signal intensities. Very large ion count rates were obtained at this channeltron. Unfortunately, after extraction, focusing and mass analysis the ion signal intensity was found to be very much reduced. The second problem associated with this detector concerned the focusing of the ions produced by the Rydberg ionizer. A final ion signal could only be obtained by operating the Rydberg ionizer at a fixed voltage. Any significant increase or decrease in this voltage resulted in total loss of the ion signal despite additional focusing. Because of this, it was not possible to obtain information about the production of Rydberg fragments with different principal quantum numbers (see Section 1.5 of Chapter 1).

## 2.6 Experimental Uncertainties

### 2.6.1 Degradation of the Time-of-Flight and Kinetic Energy Resolutions

Smyth (1973) has made a quantitative study of the factors which are responsible for degradation of the time-of-flight resolution. As may be expected, the most significant cause of this degradation is the use of a finite width electron pulse and a finite width time-of-flight window. For good time-of-flight resolution it is necessary to reduce the width of both of these windows. Unfortunately, such a width reduction necessarily involves a significant loss in signal intensity. This loss in signal intensity is a serious problem when recording excitation functions near threshold. It is often necessary to sacrifice some time-of-flight resolution in order to improve this signal intensity. The excitation functions reported in this dissertation were obtained by using a 10 μs electron pulse and a 3.5 μs time-of-flight window.

Using this setup it was necessary to accumulate data for several days and thus it was not practical to significantly reduce these pulse widths.

The time-of-flight slit function produced by combining a 10 μs electron pulse with a 3.5 μs time-of-flight window is trapezoidal in shape and has a base width of 13.5 μs. The trapezoid, which is symmetrical about a perpendicular line drawn through the centre point of this base line, has a top width of 6.5 μs. The time at the centre point of this slit function corresponds to the time delay measured from the centre of the electron pulse to the centre of the time-of-flight window. In the present work this delay is taken as the mean fragment flight time. The uncertainty in this fragment flight time is quoted as ± 5 μs. This uncertainty, which corresponds to the half width (H.W.H.M.) of the time-of-flight slit function is probably an overestimate of the error since over 90% of the recorded fragments have flight times within these limits. In fact, 65% of the recorded fragments have flight times within about ± 3 μs of the mean flight time. The uncertainty in the calculated fragment kinetic energy, corresponding to a flight time uncertainty of ± 5 μs, is quite significant since the calculation involves a $\frac{1}{t^2}$ term. The average uncertainty can be obtained by simple differentiation and is given by

$$\frac{\Delta W_B}{W_B} = \frac{2\Delta t}{t} \qquad (15)$$

where $\Delta W_B$ is the uncertainty in the kinetic energy of fragment B" and $\Delta t$ is the corresponding uncertainty in its time-of-flight. For a typical time-of-flight of 65 μs the above consideration results in a 15% uncertainty in $W_B$. The kinetic energy error bars, displayed in the following chapters, were obtained by using Eq.(15) or by calculating the kinetic energy at the appropriate time-of-flight limits. The second approach produces error bars of unequal length with respect to the kinetic energy corresponding to the mean fragment flight time. Other experimental uncertainties, which affect the measurement of the fragment kinetic energy, were found to be negligible in comparison. In particular, uncertainties due to the thermal motion of the parent gas molecules (Allcock, 1975) were negligible since a gas beam was used throughout the work.

It is important to note that in accordance with Eq.(15), the percentage error in the fragment kinetic energy becomes negligible at long flight times (i.e. low kinetic energies). This fact emphasises again the importance of a plot of fragment kinetic energy against appearance potential when determining the dissociation limit of a fragmentation process. On such a plot, the accurately known points can be used to weight a straight line fit when locating the appearance potential intercept (see Section 1.3.2 of Chapter 1).

### 2.6.2 Appearance Potential Uncertainties

A certain amount of ambiguity exists when assigning a particular kinetic energy to an observed appearance potential in an excitation function. This is because of the above spread in fragment kinetic energy and the spread in incident electron energy. The situation is somewhat simplified at long flight times where the fragment kinetic energy is accurately known. In this situation it is only necessary to consider the effect of the spread in electron energy. Given sufficient signal intensity, the first onset in a one process excitation function occurs when the highest energy electrons, in the electron energy spread, have sufficient energy to produce dissociation fragments with the above kinetic energy [see Fig. 8 (a)]. The mean electron energy [as derived from the centre tapped cathode potential (see Fig. 5)] is less than this value. As the mean electron energy is increased, the number of electrons with sufficient energy to produce the dissociation fragments also increases. This results in an increase in signal intensity which is dependent on the shape of the electron energy distribution function. Consequently, the initial curvature of an excitation function may be quite complex. This remains the case until all the electrons in the electron energy distribution function have sufficient energy to produce the above fragments. At higher electron energies, the excitation function rises in

Fig. 8(a) Determination of an Appearance Potential for Fragments of Known K.E.

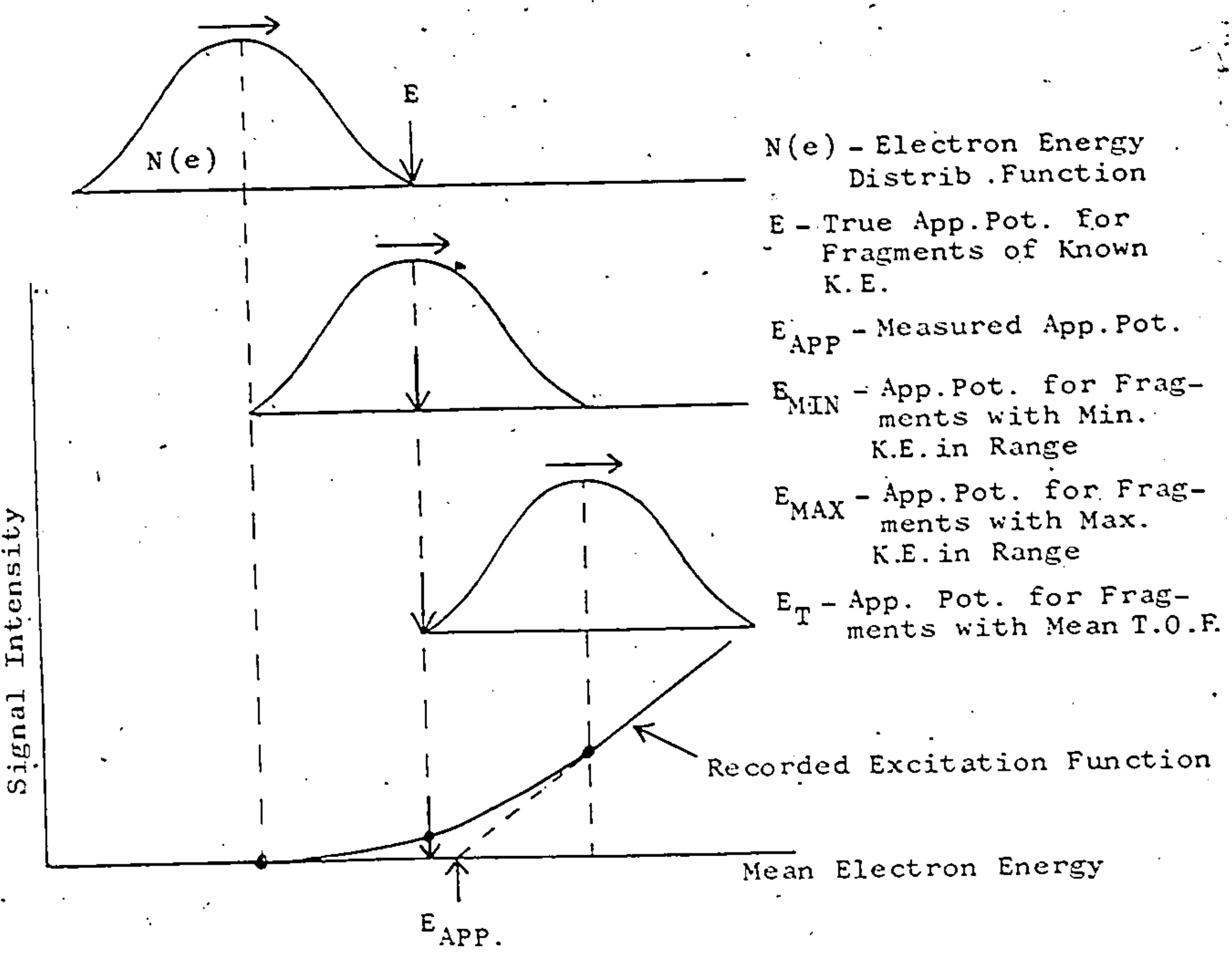

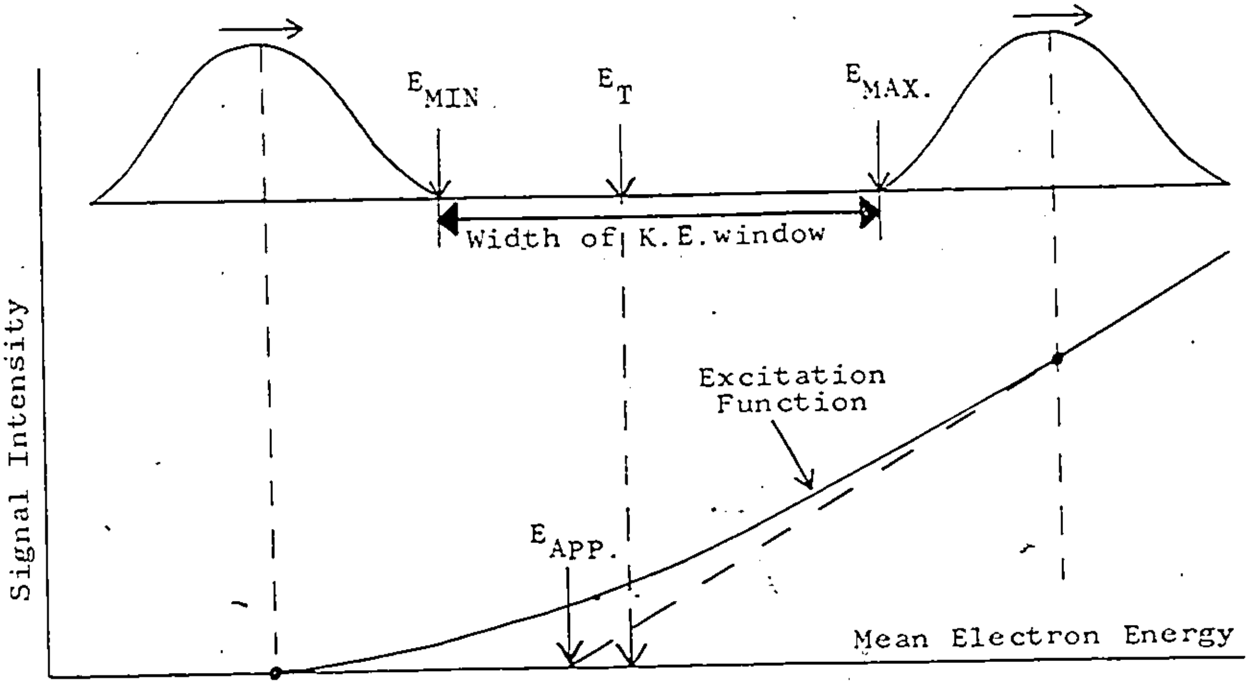

Fig. 8(b) Determination of an Appearance Potential where Fragments with a range of K.E.'s are recorded accordance with the process cross section. Initially, this rise may be approximated to a straight line. In the present work the process appearance potentials were obtained by linear extrapolation from above and below a process onset. This technique locates an appearance potential approximately half way between the first production of signal and the start of the linear rise. This appearance potential corresponds fairly well to the true threshold for production of known kinetic energy fragments [see Fig. 8(a)]. In practice, the initial curvature of the excitation functions was not clearly defined due to poor counting statistics and thus very 'sharp' onsets were normally obtained. In the following chapters an uncertainty of ± 1 eV is quoted with the measured appearance potentials. This uncertainty covers the ± 0.5 eV spread in electron energy and also reflects the difficulties involved in accurately locating an onset due to poor counting statistics.

At shorter flight times the situation becomes more complicated since fragments with a large range of kinetic energies may be recorded in an excitation function. In this case it is necessary to assign a particular kinetic energy to the appearance potential obtained by linear extrapolation. As illustrated in Fig. 8(b), a good estimate of this kinetic energy is obtained from the mean fragment flight time.

Occasionally, excitation functions were recorded by operating the electron gun in a D.C. mode during use of the Rydberg detector. The signal recorded in such excitation functions is due to the detection of fragments of all kinetic energies. However, at low electron energies the first onset of signal corresponds to the detection of the lowest kinetic energy fragments produced by the process being studied (see Eq. (6) of Chapter 1). This onset was usually visible after D.C. operation of the electron gun because of the very much greater signal intensities involved. An uncertainty of ± 1 eV is quoted with the appearance potentials obtained from such onsets.

# CHAPTER 3

## THE RESULTS FOR $CO_2$

## 3.1 Introduction

The results presented in this chapter are concerned with the atomic metastable fragments produced during the electron impact dissociation of carbon dioxide. A preliminary account of this study has already been presented (Allcock, 1975). However, since this presentation, a more detailed study of the various dissociation channels has been completed. This additional work has enabled positive identification of a number of dissociation channels to be made. In particular, the use of a primitive Rydberg ionizer (an early development stage of the Rydberg detector discussed in Chapter 2) has enabled the processes which result in Rydberg atoms to be positively identified. In addition to the most recent results, some of the previously presented data is also included in the following account. All the results are discussed in terms of a revised dissociation scheme.

Early time-of-flight studies of the break-up of $CO_2$ into metastable fragments following electron impact excitation (Freund and Klemperer, 1967; Clampitt and Newton, 1969) revealed that $CO(a^3\pi)$ molecules were produced with high efficiency but, because of a combination of poor time resolution and the use of detectors which were selectively sensitive to $CO(a^3\pi)$, fast metastable atomic fragments were not observed. More recently, Freund (1971) and Wells et al. (1972) demonstrated that, in addition to $CO(a^3\pi)$ molecules, metastable O atoms were also produced in the $3s(^5S^0)$ state and high-lying Rydberg states.

Misakian et al. (1975), in a parallel study to the present one, investigated the nature of the fast fragments in some detail. The results of these workers are in general agreement with the present data (see later). However, in the present case, the availability of excitation functions of better quality than those presented by Misakian et al. and the addition of a Rydberg ionizer to the apparatus, has resulted in considerable clarification of the dissociation processes. The agreement of the present results with those of Misakian et al. is taken as a further indication of the reliability of the apparatus.

## 3.2 Description of the Results for $CO_2$

### 3.2.1 Signal Intensity of the Fast Fragments as a Function of Gas Pressure and Electron Current

A plot of fragment signal intensity against gas-beam head pressure is shown in Fig. 9 for the fast metastable fragments produced during the dissociation of $CO_2$. The data points, which represent an integration over all the relevant flight times, were obtained using the Auger detector. The plot which was obtained at an electron energy where all the dissociation processes are contributing to the observed signal (100 eV), shows a linear relationship for head pressures below 0.04 torr. The slight non-linearity above this pressure is a characteristic of the gas-beam used and does not indicate the onset of a secondary process. This behaviour was observed with all the gases studied. The gas-beam head pressure, used during time-of-flight and excitation function data accumulation was 0.05 torr.

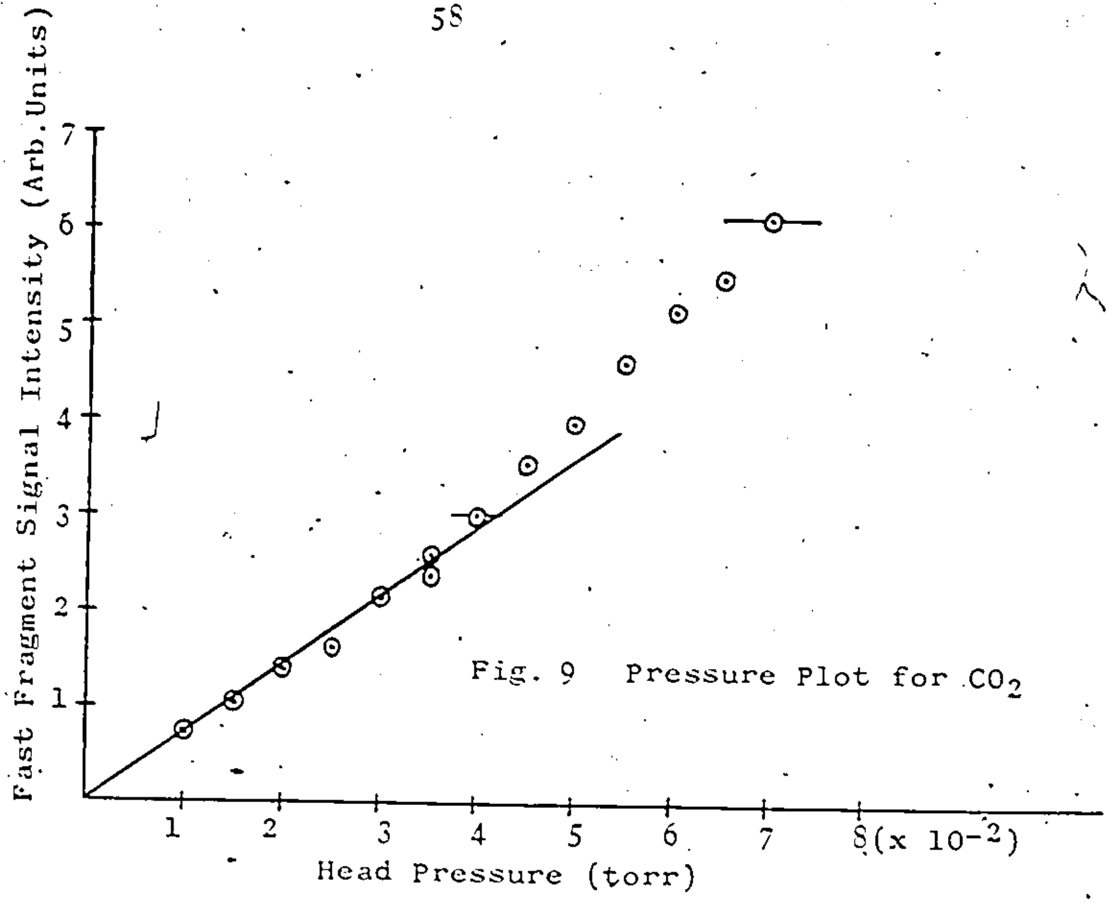

Fig. 9 Pressure Plot for $CO_2$

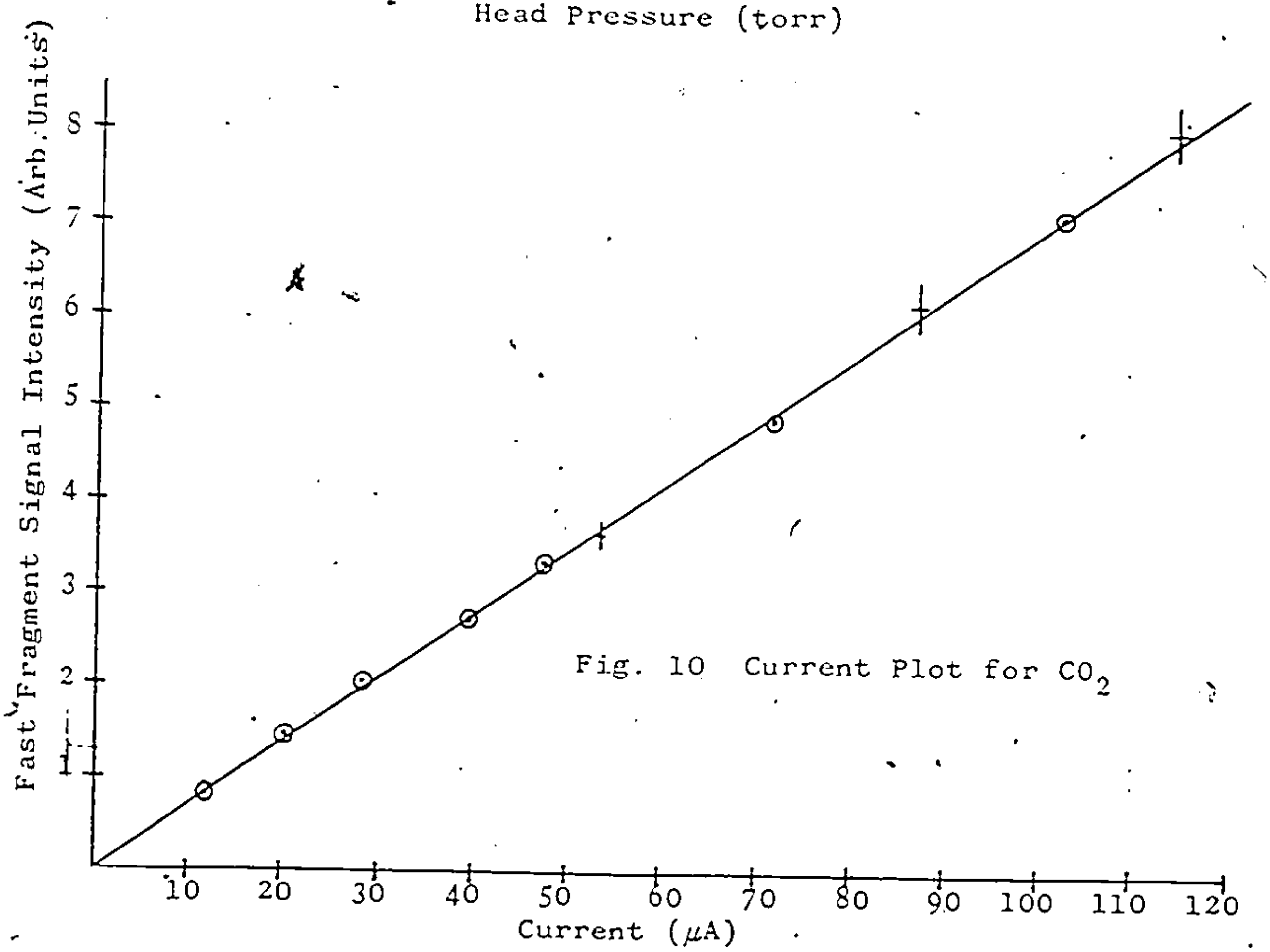

Fig. 10 Current Plot for $CO_2$

Research grade $CO_2$ was used throughout these studies.

A similar plot of fragment signal intensity against electron current is shown in Fig. 10. The plot is seen to be linear for electron currents below about 115 $\mu$A. In general, a 30 $\mu$A electron current was used during data taking. Space charge effects were found to be negligible at this electron current.

### 3.2.2 Time-of-Flight and Kinetic Energy Distributions of the Fast Fragments

The fast fragment time-of-flight spectra, which were obtained at different electron energies, are presented in Fig.11. The Auger detector was used throughout the data taking.

At an electron energy of 20 eV there is little evidence of a fast peak in the time-of-flight data. The spectrum is dominated by the broad $CO(a^3\pi)$ feature at long flight times. At an electron energy of 30 eV the fast peak is clearly visible. As the electron energy is increased, this peak broadens and becomes structured until by 100 eV at least three distinct peaks are clearly visible. Excitation function data (see later) indicates that at least five different dissociation processes contribute signal to the fast-fragment spectra. The numbering scheme, which is shown in the figure, is used to identify the features which are likely to be caused by these processes. At very short flight times, the figure also shows the presence of a photon signal. This is due to the in-flight radiative decay of some fragments (Allcock, 1975).

Fig. 11 Time-of-Flight Spectra for $CO_2$

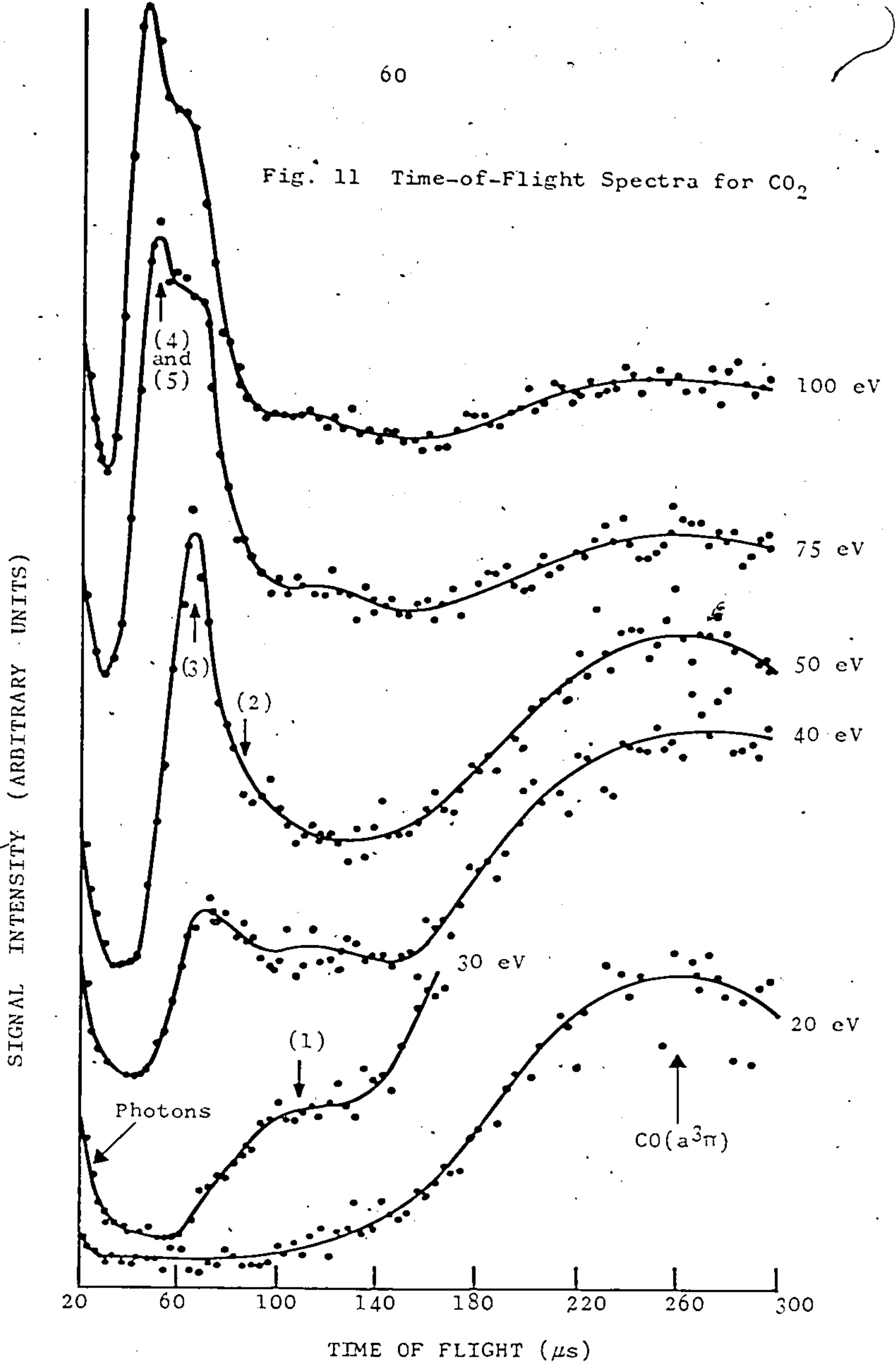

In order to investigate the contribution due to fragments in Rydberg states, a fine mesh grid, which could be raised to high potential, was placed in the path of the fragments after they entered the detector chamber (N.B. the mass sensitive Rydberg detector, discussed in Chapter 2, was not available at this time). The strong electric field between this grid and the earthed surroundings ionized a large percentage of the Rydberg atoms present in the beam. The ions produced were deflected from their path to the Auger detector by this field. The effect of this removal on the time-of-flight spectrum obtained at an electron energy of 100 eV is shown in Fig. 12. Curve A represents the data obtained when no voltage was applied to the Rydberg ionizer and curve B represents the signal obtained when its potential was raised to 5 K.V. The insert spectrum shows the difference between the two curves and hence represents the contribution due to Rydberg fragments. A number of facts are immediately obvious from this figure. Firstly, because of the almost complete disappearance of the 65 $\mu$s peak (labelled number (3) on Figs. 12 and 11), on applying the high voltage, it can be concluded that this peak is largely, if not entirely, due to the detection of fragments in Rydberg states. Secondly, at least one of the dissociation processes, which give rise to the fastest peak in the spectrum (i.e. the 45 $\mu$s peak labelled (4) and (5)), also involves the production of Rydberg fragments. In this case, however, the presence of a strong residual peak in the lower curve indicates the existence of an

Fig. 12 Time-of-Flight Spectra for $CO_2$ showing the Rydberg contribution

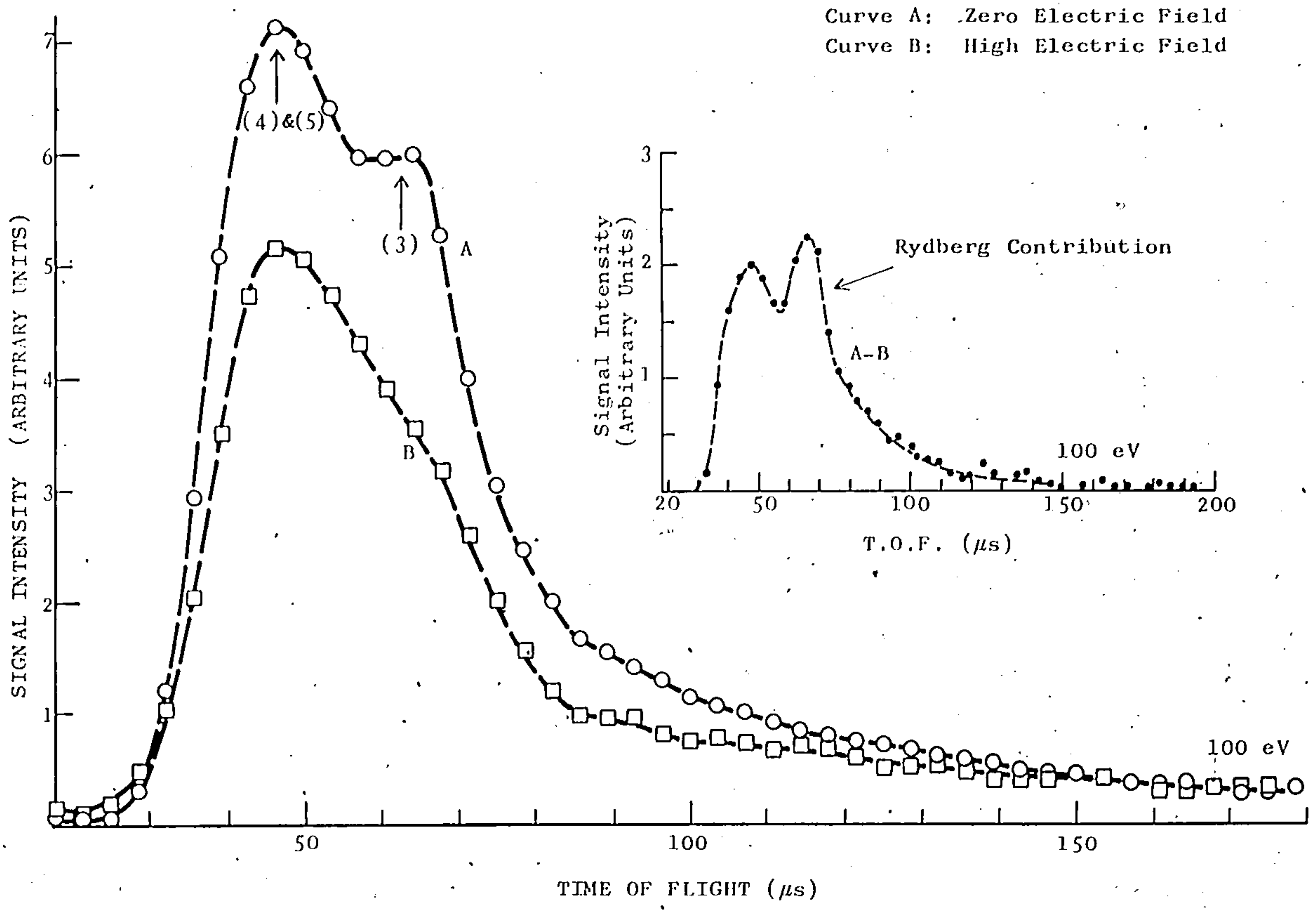

additional non-Rydberg component. Thirdly, a significant number of low energy Rydberg fragments are also produced. This is indicated by the long time-of-flight tail of the insert spectrum. Fourthly, there is also a significant non-Rydberg component at low kinetic energies (see long tail of curve B).

The time-of-flight spectra shown in Fig. 11 were converted into the corresponding kinetic energy spectra by performing a numerical transformation. The transformation involved, which strongly weights signal arriving at long flight times, has been previously discussed (Smyth et al. 1973; Allcock, 1975). In order to perform the transformation it was assumed that in all cases the detected fragment was an oxygen atom. A plot of fragment kinetic energy against appearance potential verified this assumption (see later). A number of the kinetic energy spectra are shown in Fig. 13 and for comparison, the corresponding spectra obtained by Misakian et al. (1975) are also shown in the figure. Despite differences in the relative magnitudes of the various peaks, the two sets of data clearly show the presence of four strongly overlapping features. These are numbered (1) to (4). This suggests that at least four dissociation processes are contributing to the observed signal. A fifth process is also involved. This process is partially responsible for the broad feature at high kinetic energies (see later). In the figure, feature (2) is of particular interest since its presence might not be suspected from the time-of-flight curves alone. It appears clearly in the transformed data because the transformation involved strongly

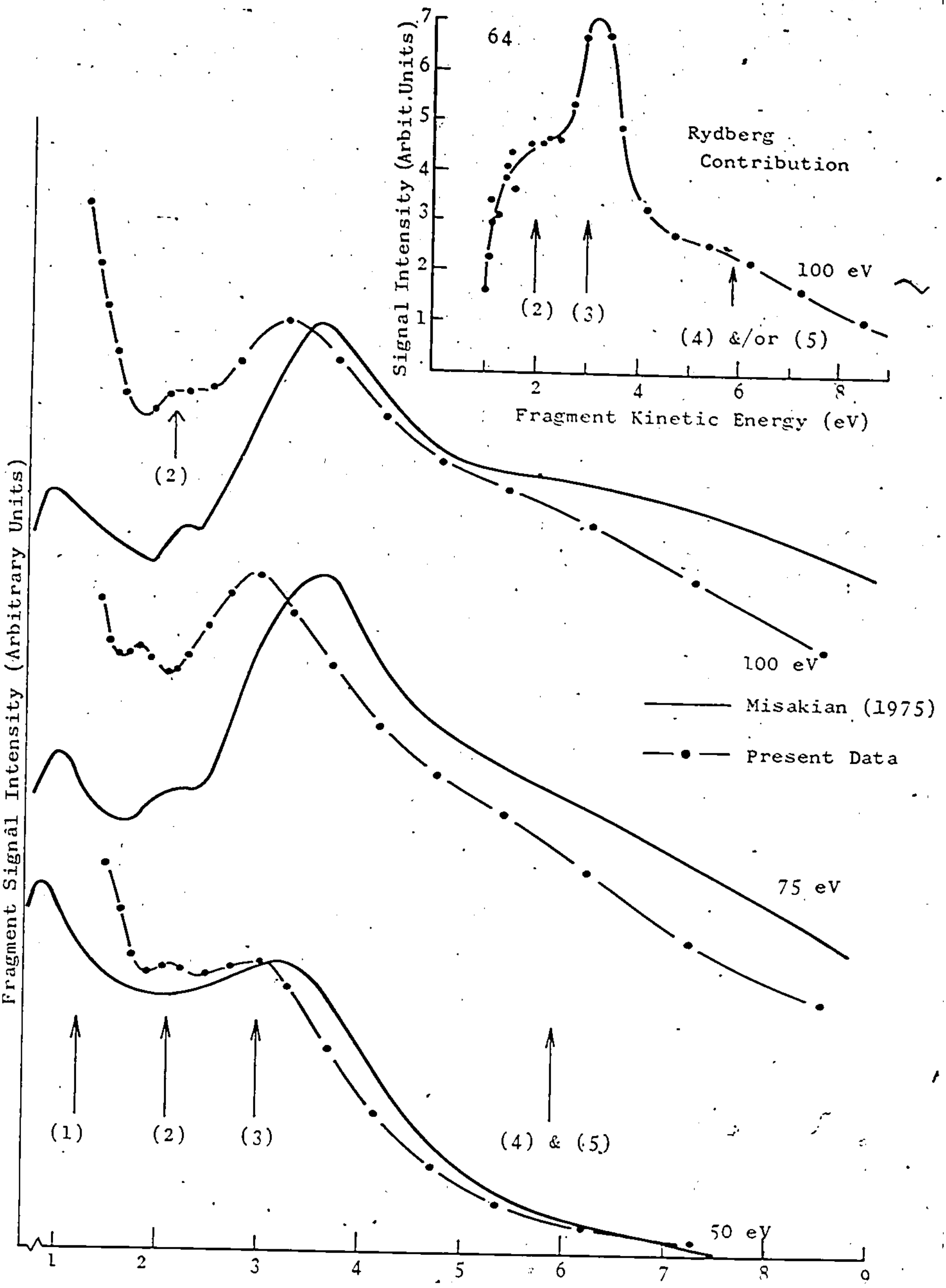

Fig. 13 Kinetic Energy Spectra for $CO_2$

weighted signal arriving at long flight times. The signal responsible for this peak is lost in the trailing edge of the time-of-flight peak labelled number (3) (see Fig. 11). This fact clearly emphasizes the importance of transforming the time-of-flight data into the corresponding kinetic energy distributions. The kinetic energy spectra have been truncated at the low kinetic energy side because of uncertainties in the background levels at long flight times. As noted above, any signal present at long flight times (e.g. due to random noise counts or to the detection of $CO(a^3\pi)$) is strongly weighted in the transformation. The slight shift to lower kinetic energies of the peak labelled number (2) (see 75 eV spectrum in the present data) is probably due to such a problem and should not be regarded as significant. Similarly, differences in the relative magnitudes of the features present in the two sets of data (i.e. the present data and that of Misakian et al.) should not be regarded as significant. Such differences might be expected not only because of the difficulties involved in making accurate kinetic energy transformations, but because of the different detector surfaces used (see Clampitt and Newton, 1968) and the different flight paths involved. The flight path used in the present experiment was about three times as long as the flight path used by Misakian et al. and would allow more in-flight radiative decay to occur. Loss of signal due to accidental field ionization of atoms in Rydberg states (i.e. by ion repelling grids, etc.) may also be a factor. The two sets of data have been normalized at the peak labelled number (3). The slight shift in the position of this peak, with respect to the data of Misakian et al., may be due to one or more of the above effects.

The insert spectrum shown in Fig. 13 was obtained by transforming the Rydberg time-of-flight spectrum shown in Fig. 12. The resulting distribution is similar in shape to the other distributions shown in the figure. Comparison of the various peak positions, with those already identified, suggests that features (2) and (3) are due to the detection of oxygen atoms in Rydberg states. In addition, the absence of feature (1), from the Rydberg spectrum, indicates its non-Rydberg nature. These suggestions are supported by the excitation function data (see later).

### 3.2.3 Excitation Functions

A number of excitation functions, corresponding to different flight times of the fast fragments, are shown in Fig. 14. The data was obtained during use of the Auger detector. The kinetic energies quoted in the figure were calculated by assuming that the detected fragment is an oxygen atom. The excitation functions, which are only representative of the available data, have been chosen to illustrate the onset of different dissociation processes. These processes are indicated by numbers above the corresponding onsets. As shown in the figure, multiple onsets were often observed for fragments with the same kinetic energy.

Fig. 14 Excitation Functions for $CO_2$

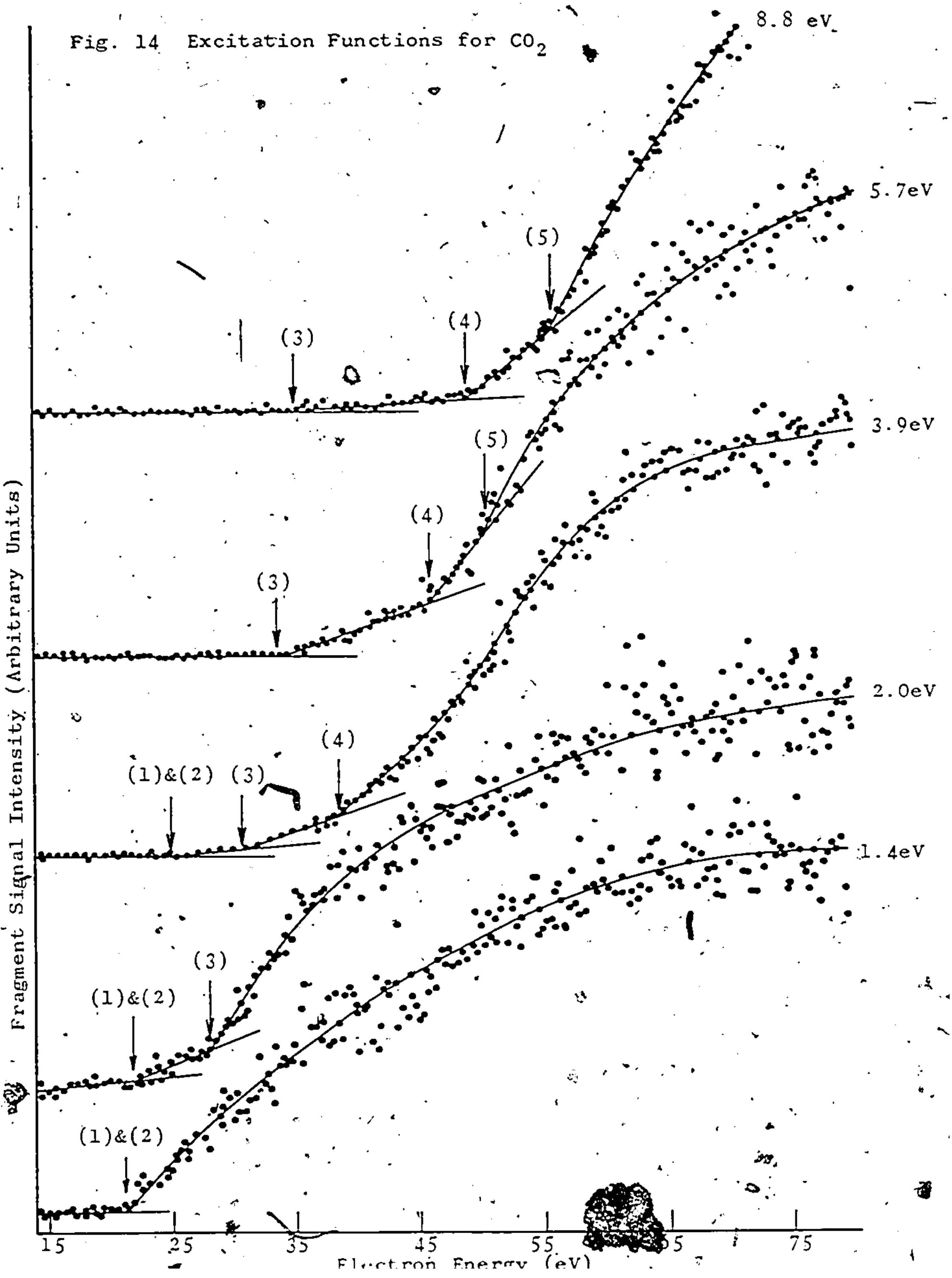

It is clear that none of the excitation functions peak sharply near threshold and hence one can conclude that direct excitation of triplet states from the singlet ground state of $CO_2$, is negligible in the present instance. This conclusion was also reached by Misakian et al. (1975).

### 3.2.4 Fragment Kinetic Energy as a Function of Appearance Potential

A plot of fragment kinetic energy (assuming that the detected fragment is an oxygen atom) against appearance potential, is presented in Fig. 15. The appearance potentials were obtained from the breaks in the excitation functions shown in Fig. 14. Additional data is also included in the figure. If the detected fragment is an oxygen atom and is produced during a two-fragment break-up of the parent molecule (i.e. a process involving the production of O and CO), then the data points corresponding to a particular dissociation process should lie on a line of slope 7/11 (i.e. the ratio of the mass of the CO fragment to that of the parent molecule). The intercept of this line with the appearance potential axis gives the dissociation limit of the corresponding molecular parent state. In the case of carbon dioxide, multiple fragmentations of the parent molecule (i.e. with the production of three fragments) may also produce a straight line of finite slope

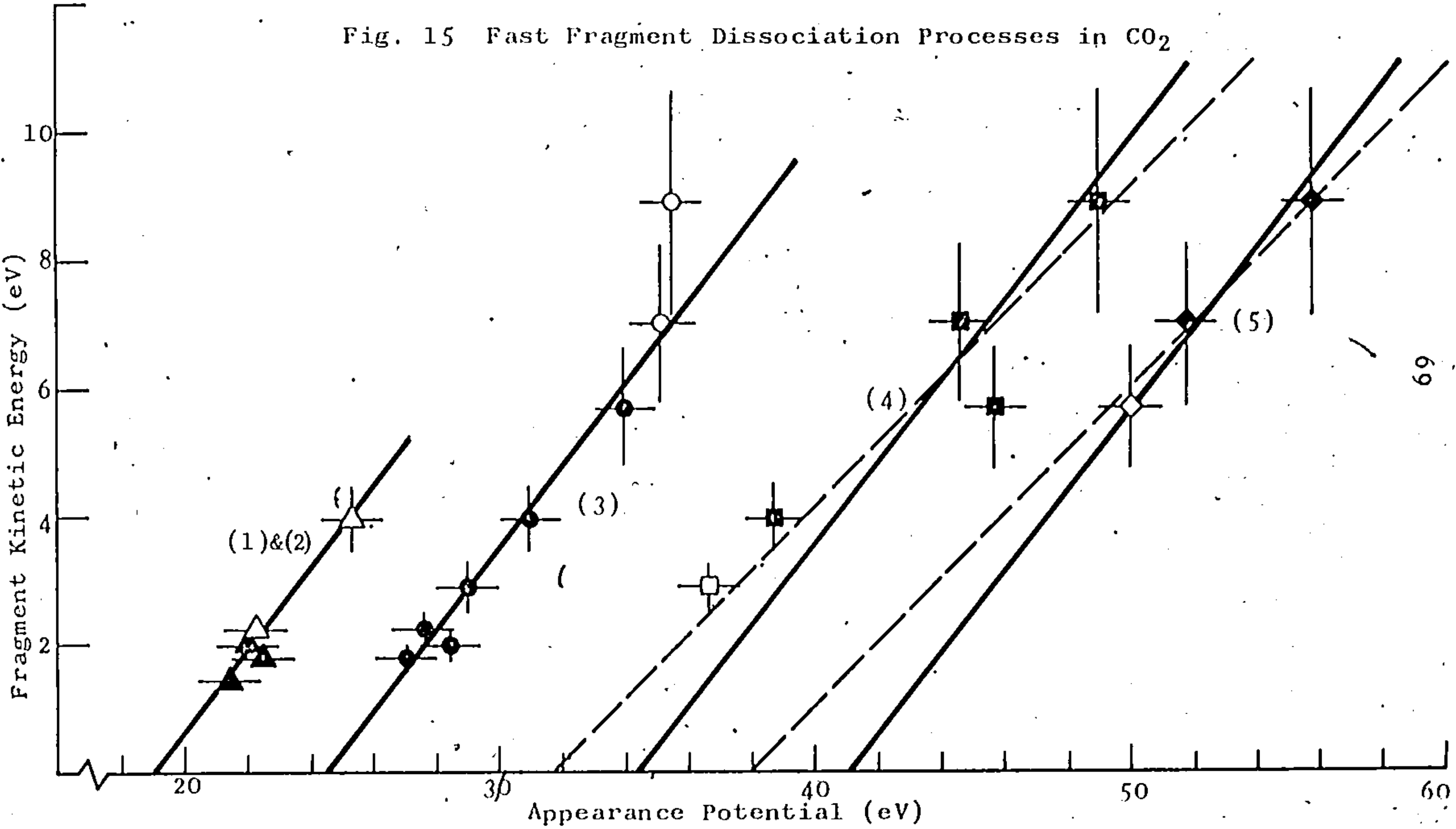

Fig. 15 Fast Fragment Dissociation Processes in $CO_2$

on such a plot. This may only occur for situations where the excited molecule remains linear and where the dissociation proceeds in a straight line with the carbon atom remaining stationary in the centre of mass frame (i.e. the dissociation of a molecule executing the symmetrical stretch mode of vibration). In this case, two equal energy oxygen atoms will be produced and a straight line plot of slope 1/2 will be obtained. Again the dissociation limit can be obtained from the appearance potential intercept.

Fig. 15 shows that the data points for processes with appearance potentials below about 35 eV do indeed lie on lines of slope 7/11 and so can be identified with O-CO break-up. The detected fragment being an oxygen atom in each case. For the remaining processes, the scatter in the data points is too great for any simple conclusions to be drawn. In particular, the data points for processes (4) and (5) could lie equally well on lines of slope 7/11 (solid line) or 1/2 (dashed line). In either case, however, the detected fragment must be an oxygen atom.

A certain amount of care is needed when assigning a particular dissociation process to an observed feature in the time-of-flight and kinetic energy distributions. This is because of the strong overlap of the features and because two of the dissociation processes have very similar dissociation limits and cannot be separated in the excitation function data. A brief discussion of how this conclusion was arrived at, and how the above processes and features were correlated, is presented below.

The excitation function data for fragments with a kinetic energy of 1.4 eV shows only one onset of signal (see Fig. 14). The data point corresponding to this onset lies on a line which intersects the appearance potential axis at 19.2 eV (see Fig. 15). The kinetic energy spectra shown in Fig. 13 indicate the presence of two strongly overlapping features at this kinetic energy. The lowest energy feature is due to the detection of non-Rydberg oxygen atoms while the higher energy feature is due to the detection of atoms in Rydberg states. The corresponding dissociation processes are labelled (1) and (2) respectively. The fact that only one appearance potential could be obtained at this kinetic energy suggests that both these processes have similar dissociation limits and cannot be separated in the data. These dissociation limits lie close to 19.2 eV. The corresponding energy spectra reach maxima at different kinetic energies because of the different shapes of the repulsive curves within the Franck-Condon region.

At higher fragment energies, signal from a third overlapping peak may also be recorded in the excitation functions. This peak, which reaches a maximum at about 3 eV, also involves the production of Rydberg oxygen atoms (see Fig. 13). The corresponding dissociation process is labelled number (3). The data points for this process lie on a line corresponding to a dissociation limit of 25 eV. Points were obtained for this process up to high fragment energies. This is consistent with the broad nature of this feature. At high fragment energies, two additional processes were observed. These are numbered (4) and (5) and are responsible for the highest kinetic energy feature of Fig. 13.

The kinetic energy error bars, shown in Fig. 15, were obtained in the manner previously discussed. The large uncertainty in the kinetic energy of the fragments at high energy should be noted as should the very small uncertainty at low kinetic energies. The maximum uncertainty involved in locating an onset is also indicated in the figure. The solid data points are regarded as good points whereas data points which have been left open are considered less reliable (see figure).

## 3.3 Discussion of the Fast Fragment Results

### 3.3.1 Introduction

Table 1 lists dissociation limits (assuming no rotational/vibrational excitation of the molecular fragment) for various possible break-up processes and also gives the measured dissociation limits (obtained from Fig. 15) for comparison. The limits obtained by Misakian et al. (1975) are also listed. The identification of the different dissociation processes is discussed below.

As a first approximation in carrying out this identification, it has been assumed that the molecular fragments produced in each case possess no rotational/vibrational

TABLE 1. A comparison of the measured dissociation limits with those of possible dissociation channels in $CO_2$.

| Dissociation Fragments† | Diss. Limit (eV) | Measured Dissociation Limit (eV) | | |
|---|---|---|---|---|
| | | Present Data | Misakian et al. (1975) | |
| $CO(X^1\Sigma_g^+) + O(^5S^0)$ | 14.6 | | | |
| $CO(X^1\Sigma_g^+) + O(^5P) \rightarrow O(^5S^0)$ | 15.7 | | | |
| $CO(X^1\Sigma_g^+) + O^+(^4S^0)R$ | 19.0 | 19.2 ± 1.0 | | (2) |
| $CO(a^3\pi) + O(^5S^0)$ | 20.6 | | 20.5 | (1) |
| $CO(a'^3\Sigma^+) + O(^5S^0)$ | 21.5 | | | |
| $CO(a^3\pi) + O(^5P) \rightarrow O(^5S^0)$ | 21.7 | | | |
| $CO(X^1\Sigma_g^+) + O^+(^2P^0)R$ | 24.0 | | | |
| $CO(b^3\Sigma^+) + O(^5S^0)$ | 25.0 | | | |
| $CO(a^3\pi) + O^+(^4S^0)R$ | 25.0 | 24.7 ± 1.0 | 25.5* | (3) |
| $CO(B^1\Sigma^+) + O(^5S^0)$ | 25.5 | | | |
| $CO(a'^3\Sigma^+) + O^+(^4S^0)R$ | 25.9 | | | |
| $CO(j^3\Sigma^+) + O(^5S^0)$ | 26.0 | | | |
| $CO(C^1\Sigma^+) + O(^5S^0)$ | 26.1 | | | |
| $CO(c^3\pi) + O(^5S^0)$ | 26.1 | | | |
| $CO(b^3\Sigma^+) + O(^5P) \rightarrow O(^5S^0)$ | 26.1 | | | |
| $CO(E^1\pi) + O(^5S^0)$ | 26.2 | | | |
| $CO(d^3\Delta) + O^+(^4S^0)R$ | 26.5 | | | |
| $CO(B^1\Sigma^+) + O(^5P) \rightarrow O(^5S^0)$ | 26.6 | | | |
| $CO(e^3\Sigma^-) + O^+(^4S^0)R$ | 26.9 | | | |
| $CO^+ + O^+(^4S^0)R$ | 33.0 | ~32 or 34 | — | (4) |
| $O(^5S^0) + C(^3P) + O^+(^4S^0)R$ | 39.0 | ~38 or 41 | 42 | (5) |

* Misakian et al. correlate this with feature (2).

† Note that the designation of the core ion is indicated for the Rydberg fragments, e.g. $O^+(^4S^0)R$.

excitation energy. This assumption is not strictly correct as it has been demonstrated, for example, that a significant amount of the energy involved in the dissociation of $CO_2$ by electron impact can go into vibrational and rotational excitation of CO (Mumma et al. 1971, 1975). Fortunately, this is not a problem in the present instance, at least for the first three dissociation processes. Here the electronic states of the fragments can be identified with little ambiguity. If the assignments are correct then the measurements indicate that little or no energy goes into the internal degrees of freedom of the CO fragment (see later). The electronic states of CO, which are listed in Table 1, were obtained from the tabulation by Tilford and Simmons (1972). If there are any hitherto unobserved electronic states of this molecule, they are likely to be high-lying and thus may be excluded from the discussion of processes (1) to (3).

### 3.3.2 Processes (1) and (2)

As pointed out above, process (1) involves the production of a non-Rydberg oxygen atom during a two-fragment dissociation of the parent molecule. The dissociation limit of the process is close to 20 eV. The only non-Rydberg process producing a detectable oxygen atom which has a dissociation limit in this energy region, is that involving the production of $CO(a^3\pi)$ and $O(^5S^0)$. The dissociation limits of other possible states are too high or too low as shown in Table 1 (N.B. the measured dissociation limits are upper bounds if the CO fragments are vibrationally excited). The dissociation limit deduced from Fig. 15 is somewhat less than the 20.6 eV expected for this process. This is attributed to the overlap which is occurring between process (1) and process (2) which has a dissociation limit of 19.0 eV (see below). The spread in incident electron energy, combined with low signal intensities at energies close to threshold, prevented differentiation between the data points from these processes.

Assuming the above designation for fragments from process (1), the Wigner-Witmer correlation rules predict a $\pi$ classification for the molecular parent state with multiplicities of 3, 5 or 7. Despite the strongly overlapping kinetic energy distributions, Misakian et al. (1975) attempted to measure the angular distribution of dissociation fragments from process (1). From these measurements they predict that the initial excitation is to a $\Sigma_u^+$ state of the parent molecule. They explain the apparent contradiction between this result and the above discussion by suggesting that this state is predissociated by a repulsive $\pi_u$ state. They also suggest that the $\Sigma_u^+$ state is a singlet in order to remain consistent with the fact that the excitation functions do not peak sharply near threshold (N.B. the ground state of $CO_2$ is a singlet). This, however, violates the $\Delta S = 0$ selection rule for the predissociation since, as pointed out above, the $\pi$ state is a multiplet. To overcome this problem, the workers suggest that the ${}^1\Sigma_u^+$ parent state has a certain triplet character due to spin orbit mixing, which allows it to interact with a triplet π state.

As discussed previously, it is likely that process (2) involves the production of a Rydberg oxygen atom during a two fragment dissociation of the parent molecule. The dissociation limit of this process is close to that of process (1). The only Rydberg producing process in this energy region has a dissociation limit of 19.0 eV and corresponds to the production of CO(X $^1\Sigma_g^+$) and O(R) (see Table 1). It should be noted that the combined dissociation limit for processes (1) and (2) is actually quite close to this value. Additional support for the existence of this channel comes from the unpublished work of J.A. Schiavone and R.S. Freund (1975; private communication).

Assuming that the fragments produced by process (2) are CO(X $^1\Sigma_g^+$) and O(R), the Wigner-Witmer correlation rules predict the involvement of a $\Sigma^-$, π or Δ parent state since the Rydberg oxygen atom, which correlates with the above dissociation limit, can be in an $S^0$, P or $D^0$ state. The molecular parent state can be a triplet or a quintet in accordance with the multiplicity of the Rydberg atom. Direct excitation of the $\Sigma^-$ state is unlikely because it involves a parity violation (+ → -) and similarly, excitation of a Δ state would be unlikely because of its dipole forbidden nature. Furthermore, a transition from a singlet state to a quintet is not possible by electron impact. It is, therefore, likely that the initial excitation is to $^3\pi$. This appears to contradict the experimental fact that the excitation functions do not peak sharply near threshold and suggests that a more complicated dissociation mechanism may be involved, as invoked previously for process (1).

It should be noted that the present conclusions about process (2) are significantly different from those of Misakian et al. They discounted the possibility of any process with a 19 eV dissociation limit.

### 3.3.3 Process (3)

Process (3) involves the production of a Rydberg oxygen atom during a two-fragment dissociation of the parent molecule. The dissociation limit of the process is close to 25 eV. Table 1 shows that three Rydberg producing processes have dissociation limits which lie within about ± 1 eV of this energy. The most likely of these has a dissociation limit of 25.0 eV and involves the production of a CO($a\ ^3\pi$) molecule and a Rydberg oxygen atom based on a $^4S^0$ core ion. The corresponding parent state could be a singlet or triplet $\Sigma^+$ or $\pi$. A less likely candidate has a dissociation limit of about 24 eV and produces a ground state CO molecule (i.e. CO($X\ ^1\Sigma_g^+$)) and an oxygen Rydberg based on a $^2P^0$ core ion. This process is a less likely candidate because its dissociation limit is slightly low and because there is a possibility of the Rydberg oxygen atom autoionizing. The parent state of this process could be a singlet or triplet $\Sigma^+$ or $\pi$. The final process, which has a dissociation limit of 25.9 eV, involves the production of a CO($a'\ ^3\Sigma^+$) molecule and an oxygen Rydberg atom based on a $^4S^0$ core ion. This process is an unlikely candidate since its dissociation limit lies at the very limit of the energy error bars (see Fig. 15). Additional evidence for its exclusion comes from the symmetry of its parent state. The angular distribution measurements of Misakian et al. (1975) demonstrate that for fragments with kinetic energies between 2.4 and 3.3 eV, the dominant parent states are $\Sigma_u^+$ in nature. In this energy range fragments from process (3) dominate the kinetic energy spectrum (see Fig. 13). However, for a process producing CO(a' $^3\Sigma^+$) and O(R), the Wigner-Witmer correlation rules exclude a parent state of the above symmetry. In contrast, a CO(a $^3\Pi$) fragment can combine with a P or $D^0$ state of the Rydberg oxygen atom to yield a $\Sigma^+$ resultant. It is, therefore, likely that process (3) proceeds as follows

$$\begin{aligned} e + CO_2(X\,^1\Sigma_g^+) \rightarrow\ & CO_2(^1\Sigma_u^+) + e \\ & \hookrightarrow CO(a\,^3\Pi) + O(^3P \text{ or } ^3D^0) \end{aligned} \tag{16}$$

where the excited parent molecule and the fragment oxygen atom are both in Rydberg states. In the above equation, the Rydberg oxygen atom is in a triplet state. This would allow the initial excitation to be to a singlet parent state and hence allow the $\Delta S = 0$ selection rule to hold. As pointed out previously, the excitation functions do not peak sharply near threshold as would be expected if the above selection rule was violated.

There is some evidence of a residual peak following the removal of Rydberg fragments from feature (3) (see Fig. 12). This is probably due to the fact that the Rydberg ionizer was not 100% efficient.

### 3.3.4 Processes (4) and (5)

Processes (4) and (5) have relatively high dissociation limits. Data points could only be obtained for fragments with high kinetic energies (see Fig. 15). Consequently, their positions are somewhat uncertain as indicated by the very large energy error bars. Only three data points could be obtained for process (5) and the data points for process (4) appear to be quite scattered. In both cases, the data points could lie equally well on lines of slope 7/11, indicating a two-fragment dissociation into O and CO, or 1/2, indicating a linear O ← C → O break-up. These facts, together with the lack of information about possible dissociation limits at high energy, prevent positive identification of the various fragment states. However, a possible dissociation channel is indicated in Table 1 for each process. The detected fragments are assumed to be $O(^5S^0)$ or oxygen Rydbergs. It should be noted that the corresponding kinetic energy feature, shown in Fig. 13, has both a Rydberg and a non-Rydberg component. Process (4) could produce ground state $CO^+$ ions in addition to O(R) fragments (dissociation limit 33.0 eV) and process (5) could produce both $O(^5S^0)$ and O(R) fragments during a total fragmentation of the parent molecule (dissociation limit 39.0 eV).

The appearance potential data of Misakian et al.

(1975), for processes (4) and (5), is in rough agreement with the present data. They also suggest a total fragmentation of the parent molecule for process (5). The high kinetic energy of the fragments produced by these processes indicates that the corresponding repulsive curves are very steep.

# CHAPTER 4

# THE RESULTS FOR $CCl_2F_2$ AND $CCl_3F$

## 4.1 Introduction

Recently there has been considerable interest in the freons, particularly $CCl_2F_2$ and $CCl_3F$, because of their involvement in the catalytic destruction of ozone in the stratosphere (see page 4). Previous work on these molecules has been limited to studies of photon absorption using photon impact (Ajello et al. 1976; Doucet et al. 1973; Gilbert et al. 1974; Jochims et al. 1976; Person et al. 1975; Roland and Molina 1975) and electron impact techniques (Huebner et al. 1975; King and McConkey 1977). Although the occurrence of molecular dissociation could be inferred from these measurements, little quantitative information is available about the participating dissociation channels, particularly at high energy. In the present work, a number of these dissociation channels have been positively identified, though the energy ranges involved mean that these channels are not directly relevant to solar photodissociation studies. As may be expected from the similarity in structure, the results obtained for $CCl_3F$ are very similar to those obtained for $CCl_2F_2$.

## 4.2 Description of the Results for $CCl_2F_2$ and $CCl_3F$

### 4.2.1 Fragment Signal Intensity as a Function of Gas Pressure and Electron Current

Plots of fragment signal intensity (integrated over all flight times) against gas-beam head pressure were obtained for $CCl_2F_2$ using both the Auger detector and the Rydberg detector. The plots, which were obtained at an electron energy where all the dissociation processes are contributing to the observed signal (100 eV), were similar in shape to the pressure plot obtained for $CO_2$ (see Fig. 9) and are not presented here. The gas-beam head pressure used during time-of-flight and excitation function data taking in $CCl_2F_2$ and $CCl_3F$, was 0.05 torr. Commercially available samples of both gases were used throughout these studies. The stated purity of the samples was 99% (minimum purity).

A plot of fragment signal intensity against electron current was also recorded for $CCl_2F_2$. The plot, which shows a linear relationship for electron currents below 127 $\mu$A, was similar to the electron current plot obtained for $CO_2$ (see Fig. 10) and is not presented here. In general, a 100 $\mu$A electron current was used during data taking in $CCl_2F_2$ and $CCl_3F$. Space charge effects were found to be negligible at this electron current.

### 4.2.2 Time-of-Flight and Kinetic Energy Distributions

Time-of-flight spectra of the dissociation fragments produced during the breakup of $CCl_2F_2$ and $CCl_3F$ are shown in Fig. 16 and Fig. 17 respectively. The data was obtained during use of the Auger detector at the electron energies quoted. The spectra obtained for each gas, which were accumulated by computer using the techniques outlined in subsection 2.4.2. of Chapter 2, are intensity normalized. Both sets of data show two broad features which increase in intensity as the electron energy is increased. The relative magnitude of

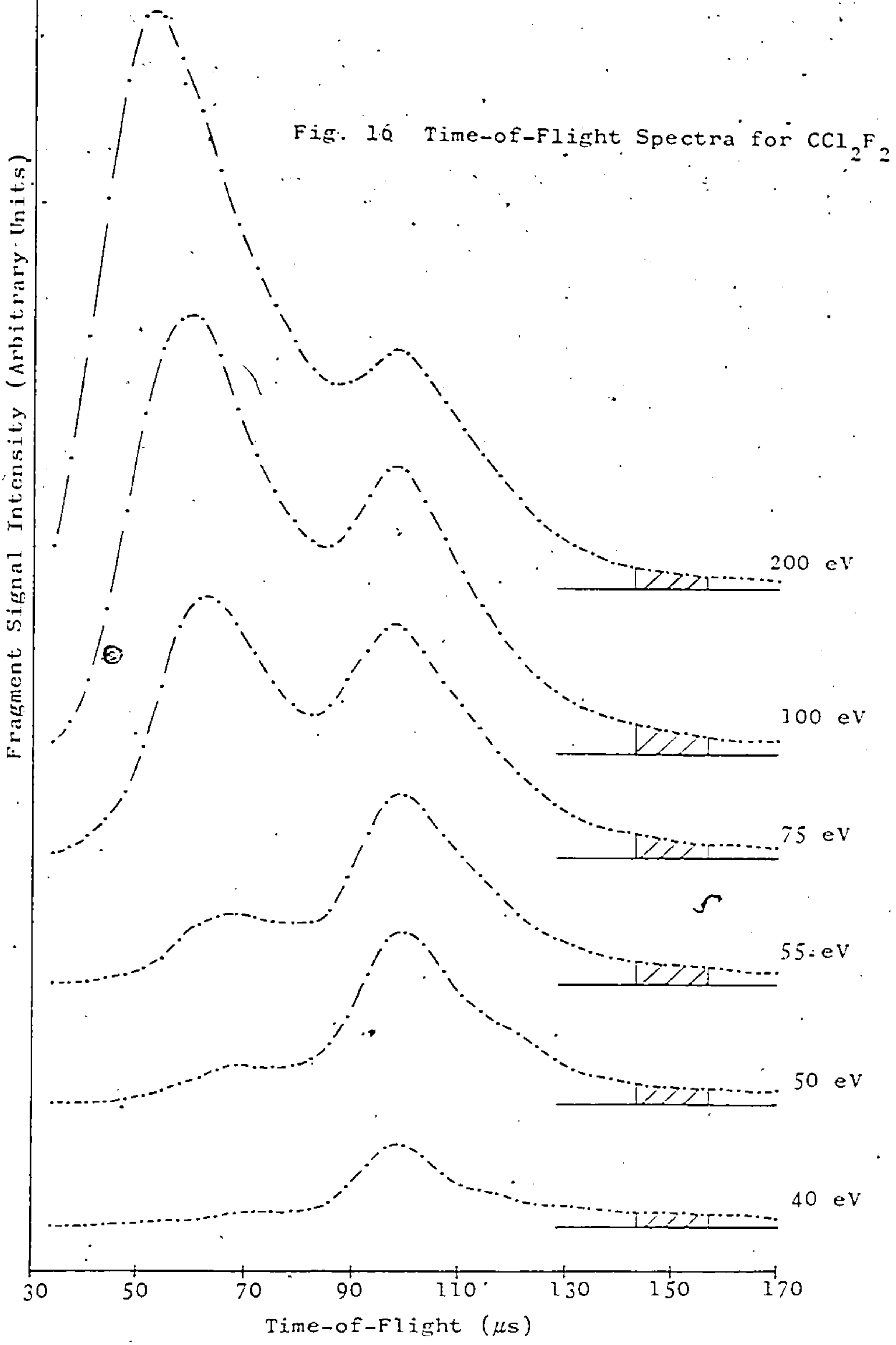

Fig. 16 Time-of-Flight Spectra for $CCl_2F_2$

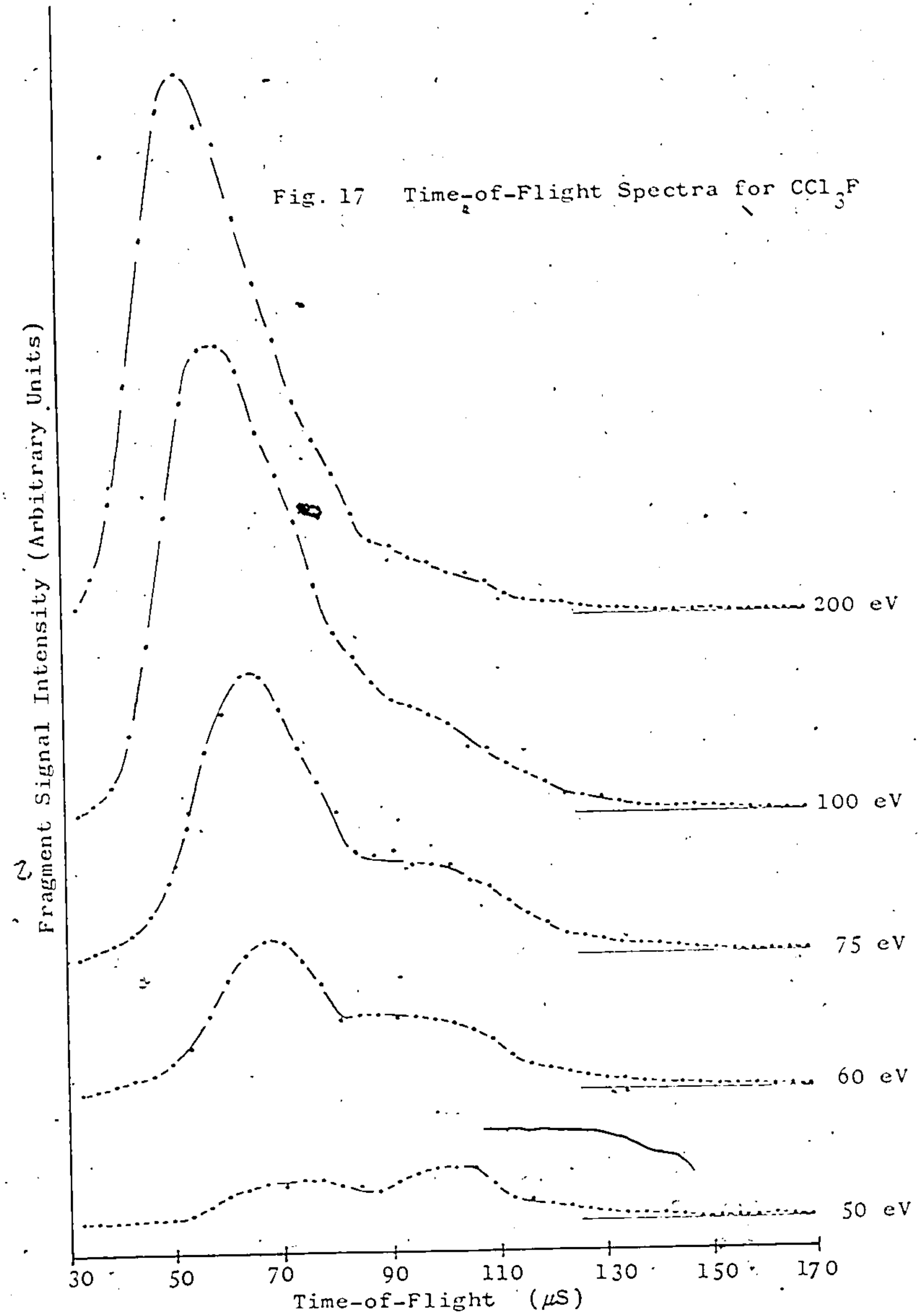

Fig. 17 Time-of-Flight Spectra for $CCl_3F$

the features also changes as the electron energy is increased. The features reach a maximum at about the same flight time in both gases. It is not possible to transform the time-of-flight spectra into the corresponding kinetic energy spectra since the signal recorded in each figure is due to the detection of fragments of different mass. Excitation function measurements (see later) indicate that both features in the time-of-flight spectra are mainly due to the detection of atomic fluorine and chlorine fragments.

Time-of-flight spectra were also recorded at different electron energies during use of the Rydberg detector. In this case, the mass spectrometer was tuned to accept fragments of a particular mass. Time-of-flight spectra of the atomic fluorine, chlorine and carbon Rydberg fragments, produced during the dissociation of both gases, were recorded in this way. The corresponding kinetic energy spectra are presented in Figs. 18-20. The data sets, which are intensity normalized, show some evidence of structure indicating that a number of processes are contributing to the observed signal. The numbers shown above the spectra serve to identify some of these processes for later discussion. Since many of the dissociation processes identified in $CCl_3F$ have approximately the same dissociation limits as those identified in $CCl_2F_2$ (see later), the same numbering scheme is used for both gases. The very wide range of fragment kinetic energies (up to 20 eV in certain cases) should be noted. This indicates that very steep repulsive

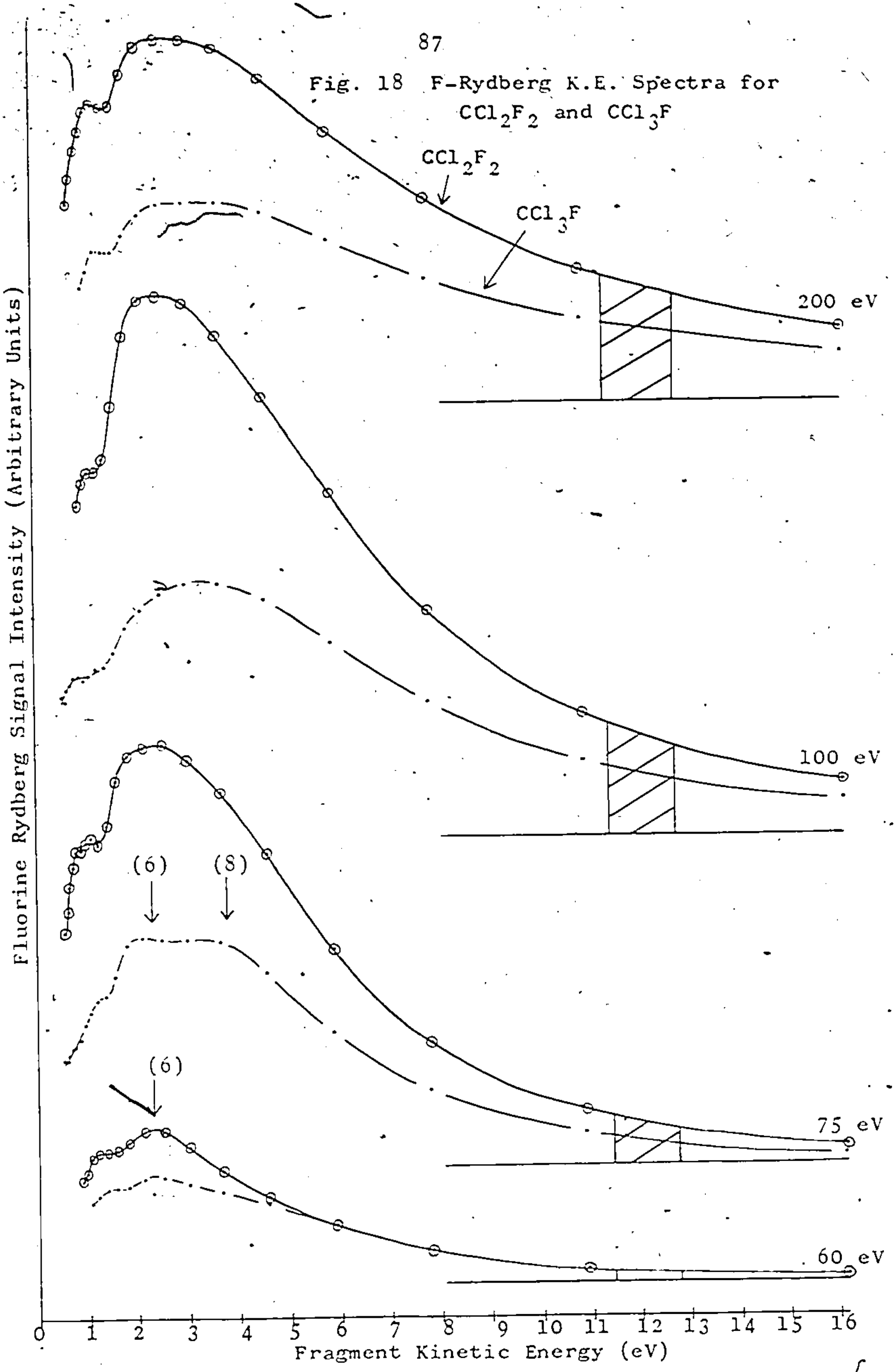

Fig. 18 F-Rydberg K.E. Spectra for $CCl_2F_2$ and $CCl_3F$

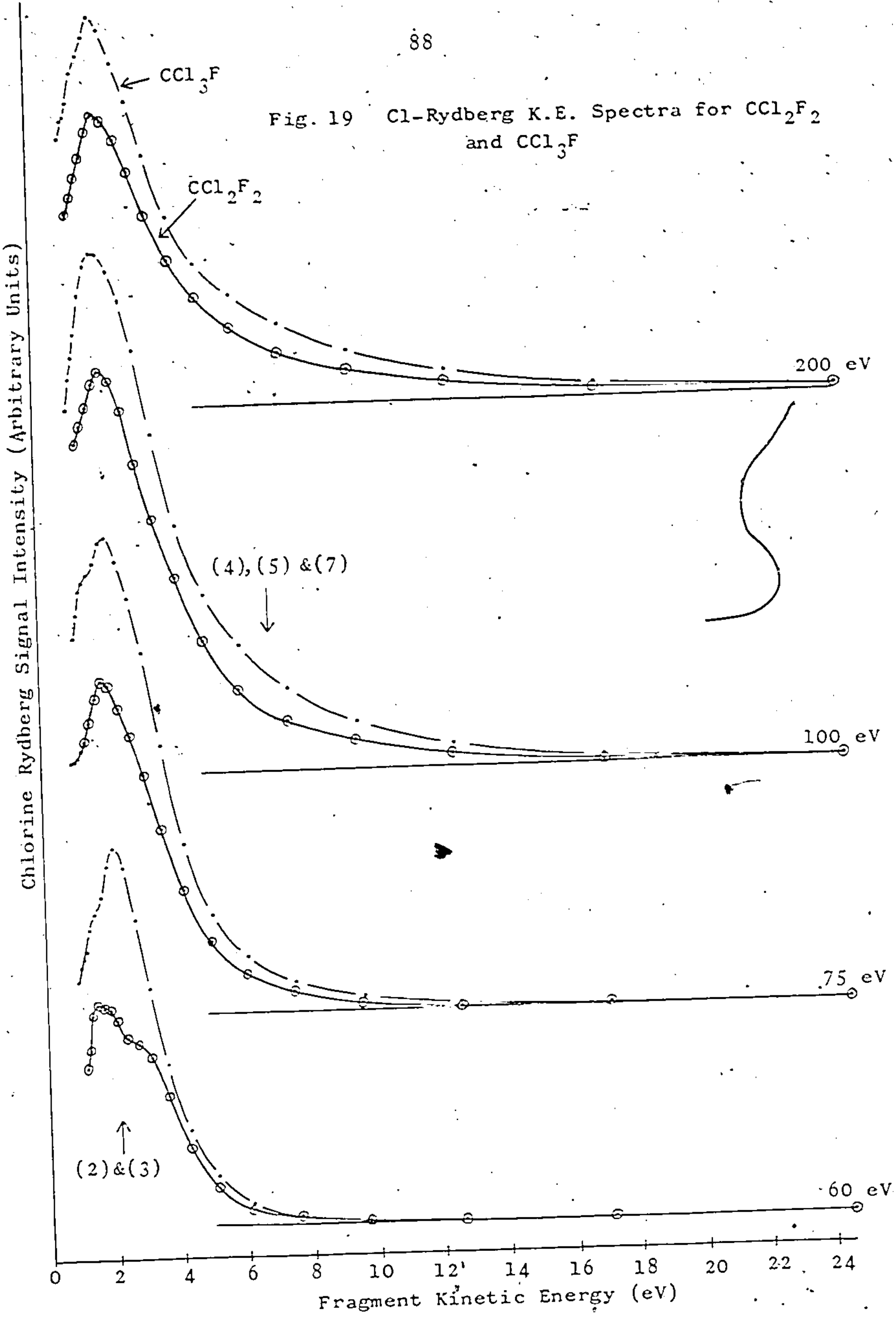

Fig. 19 Cl-Rydberg K.E. Spectra for $CCl_2F_2$ and $CCl_3F$

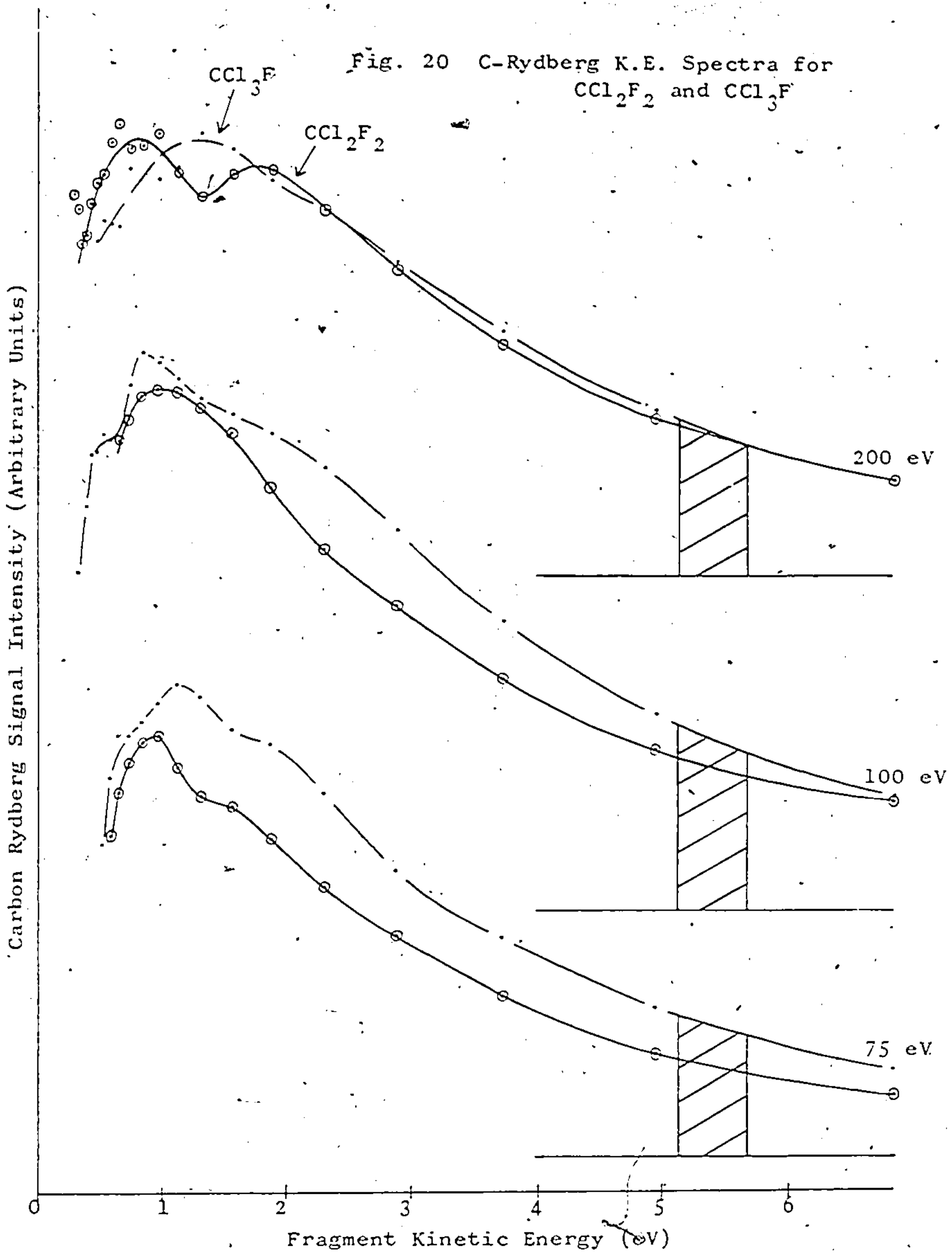

Fig. 20 C-Rydberg K.E. Spectra for CCl$_2$F$_2$ and CCl$_3$F

curves in the Franck-Condon region are sometimes involved. The kinetic energy distributions are terminated at the low kinetic energy side because of the uncertainties involved in locating the time-of-flight baseline. The time-of-flight spectra, corresponding to Figs. 18-20, provide little additional information and are not presented in this dissertation.

### 4.2.3 Excitation Functions

A number of excitation functions, corresponding to different fragment flight times, are shown in Fig. 21 and Fig. 22 for $CCl_2F_2$ and $CCl_3F$ respectively. The data was obtained during use of the Auger detector. The kinetic energies quoted in the figures were obtained by assuming that the detected fragment is a fluorine atom. The excitation functions, which represent only a small fraction of the available data, have been chosen to illustrate the onset of different processes. These processes are indicated by numbers above the corresponding onsets. As shown in the figures, multiple onsets were often observed for fragments with the same kinetic energy. The relative intensities of the different curves in each figure may be obtained by taking into account the appropriate scaling factors (noted beside each curve).

Fig. 23 and Fig. 24 show similar curves taken with the Rydberg detector tuned to F and Cl, for $CCl_2F_2$ and $CCl_3F$ respectively. The appropriate kinetic energies are indicated in each case. Similar data was taken for the carbon Rydbergs

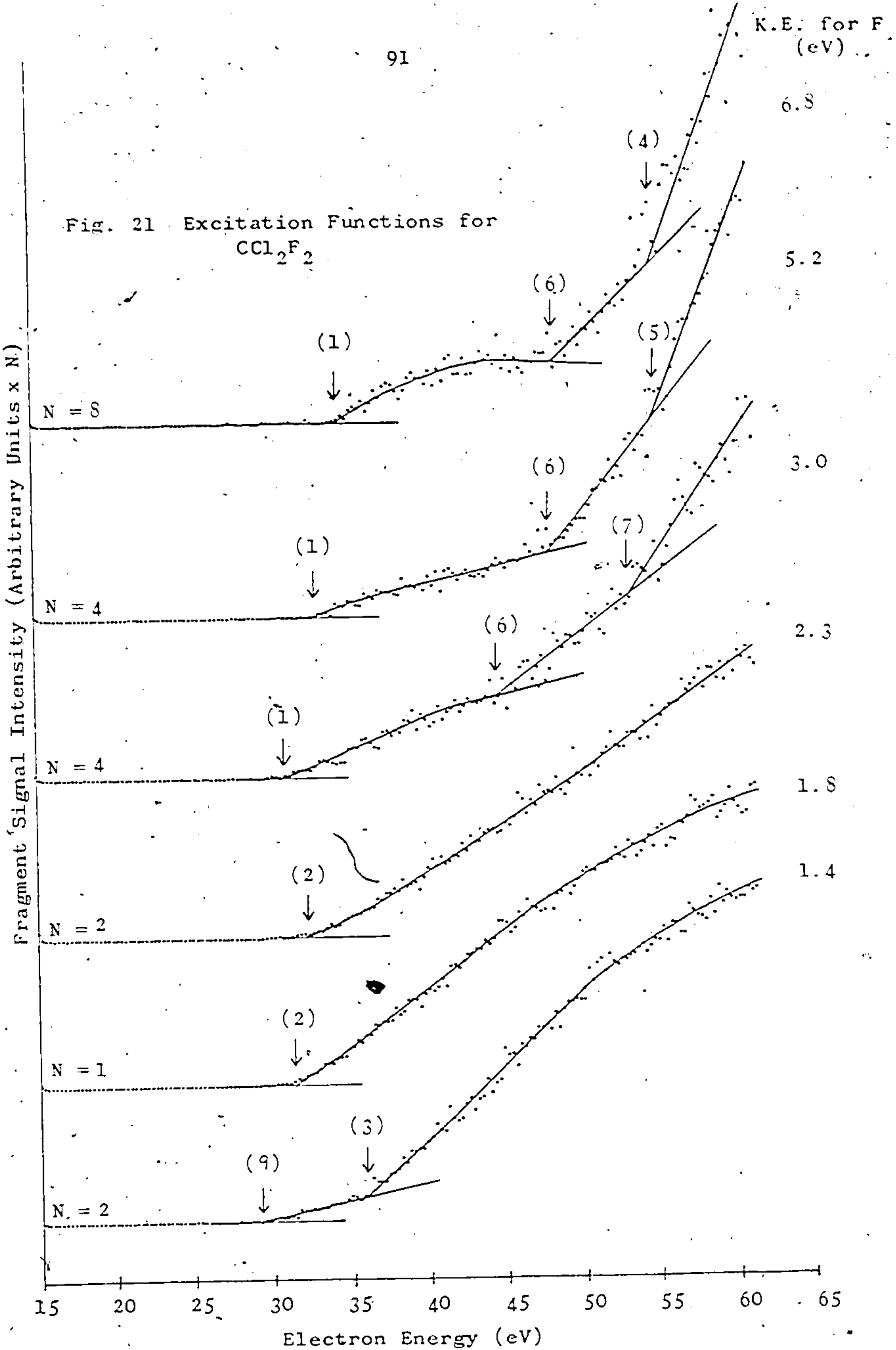

Fig. 21 Excitation Functions for $CCl_2F_2$

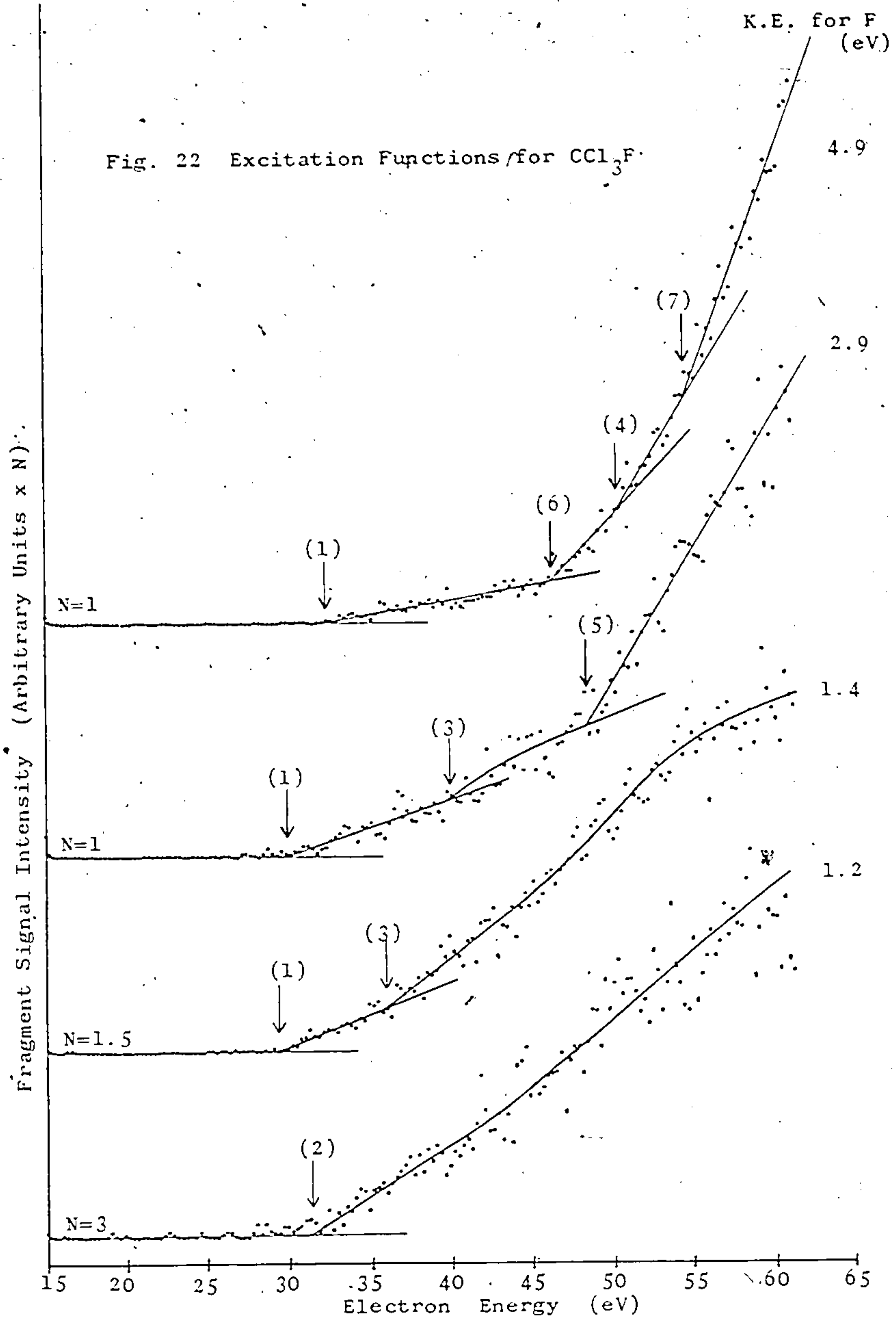

Fig. 22 Excitation Functions for $CCl_3F$

Fig. 23 F-Rydberg and Cl-Rydberg Excitation Functions for $CCl_2F_2$

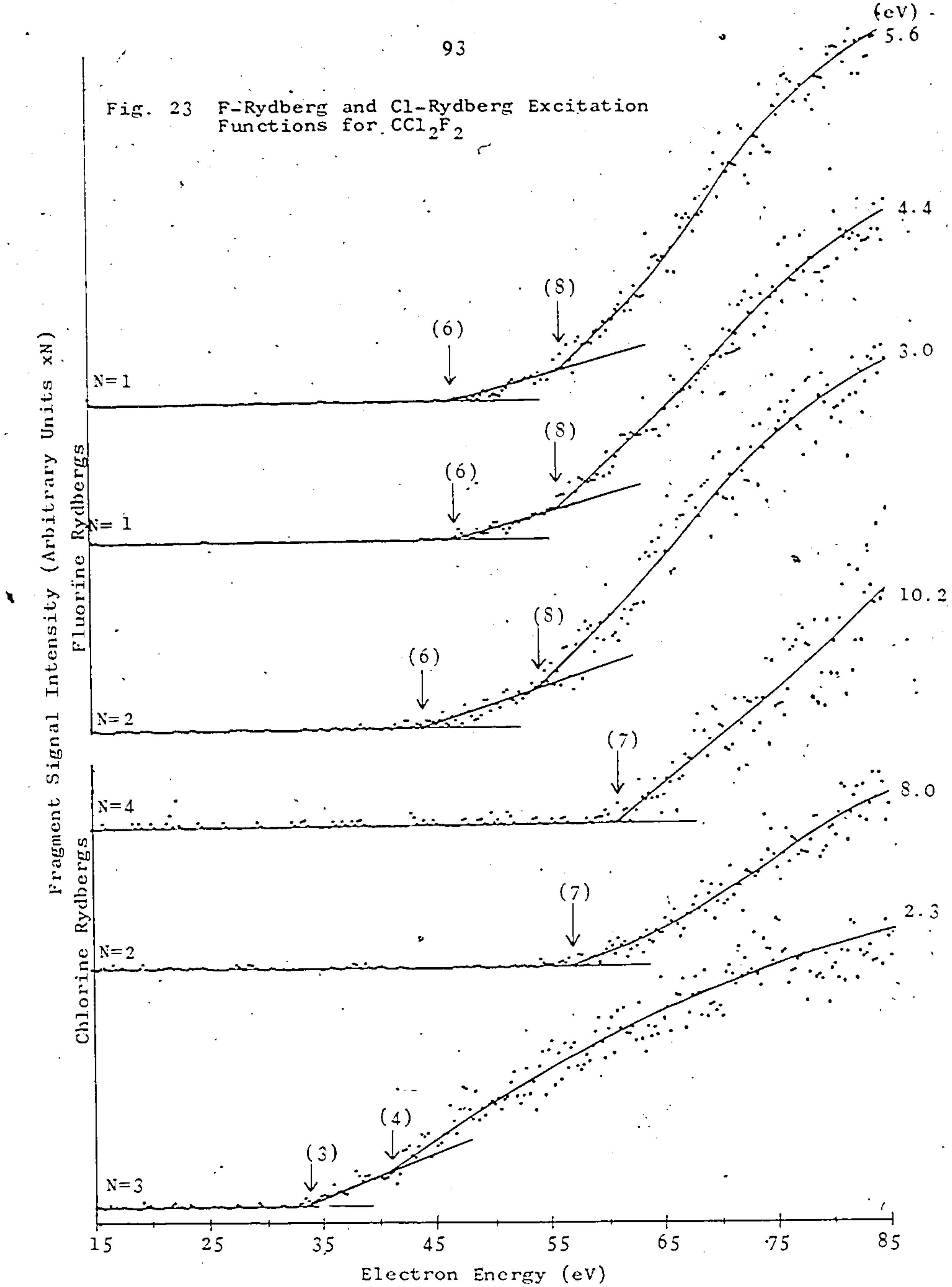

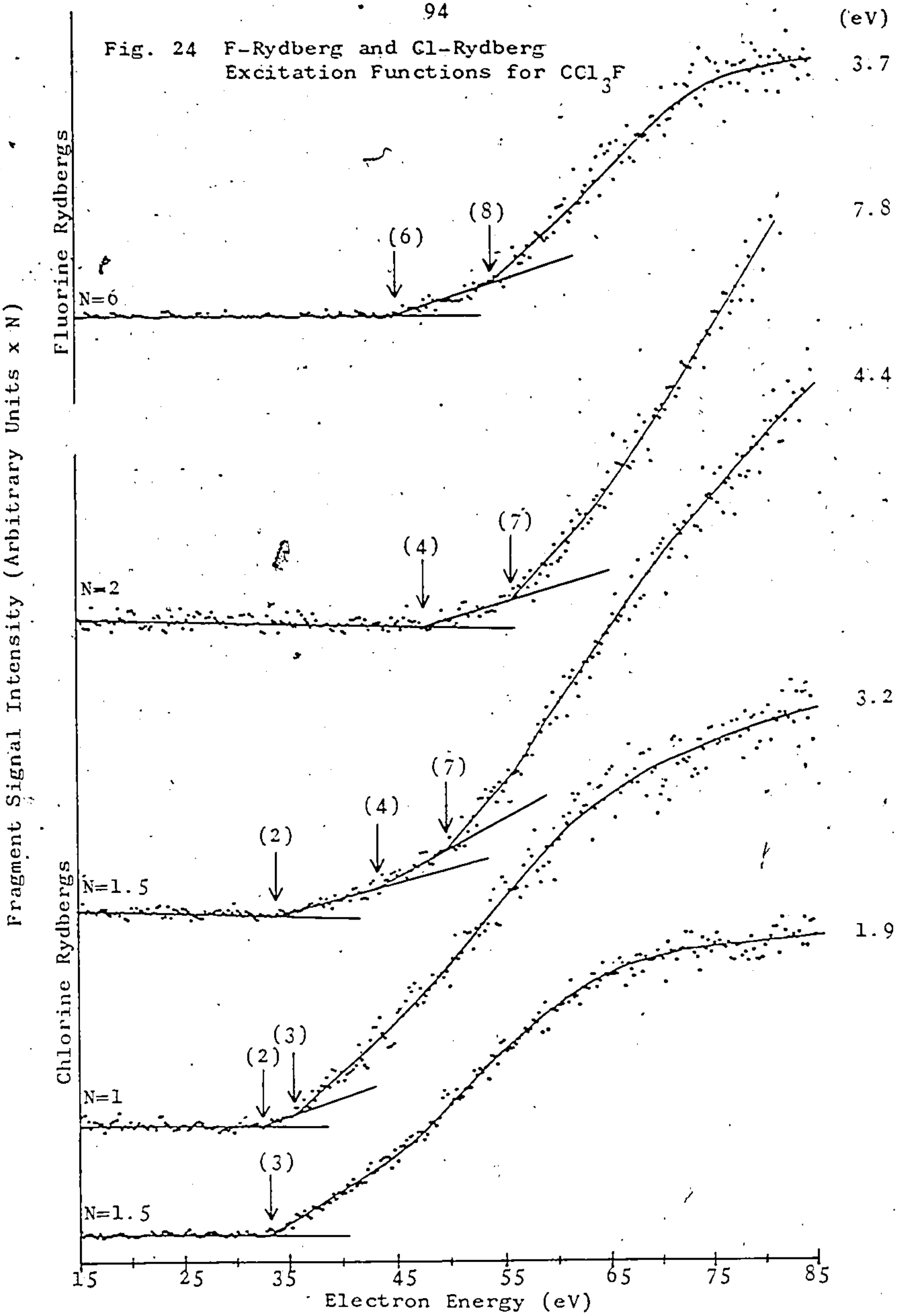

Fig. 24 F-Rydberg and Cl-Rydberg Excitation Functions for $CCl_3F$

produced during the dissociation of $CCl_2F_2$. This data is displayed in Fig. 25.

Excitation functions (not shown) were also recorded during use of the Rydberg detector by operating the electron gun D.C. The appearance potentials obtained in this case are likely to be quite close to the dissociation limits of the Rydberg processes since they correspond to the detection of low kinetic energy fragments. Excitation functions of this type were recorded for the F and Cl Rydbergs produced during the dissociation of both gases. The greater signal intensities obtained during D.C. operation of the electron gun enabled a number of additional weak processes to be observed. The data gives little information about these additional processes apart from the identity of the Rydberg atoms produced. For example, it is not known whether these atoms are produced during two-fragment dissociations or multiple-fragment dissociations of the parent molecule.

### 4.2.4 Fragment Kinetic Energy as a Function of Appearance Potential

A plot of fragment kinetic energy (assuming that the detected fragment is a fluorine atom) against appearance potential is presented in Fig. 26 for $CCl_2F_2$. (A similar plot was obtained during the study of $CCl_3F$.) The figure shows the presence of nine different dissociation processes each of which has a different dissociation limit (appearance potential intercept). Most of the data points (open circles) were obtained during use of the Auger detector.

Fig. 25 C-Rydberg Excitation Functions for $CCl_2F_2$

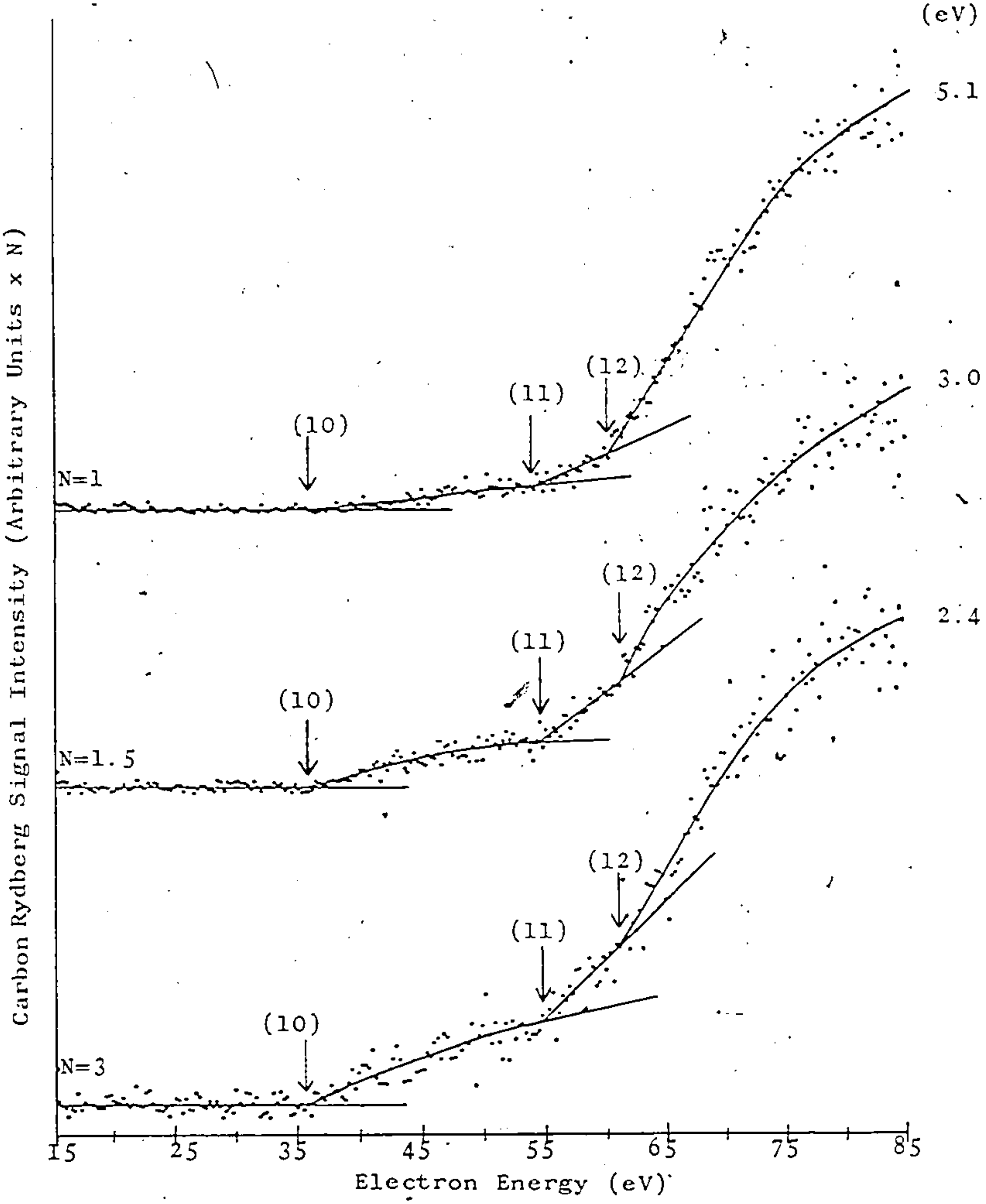

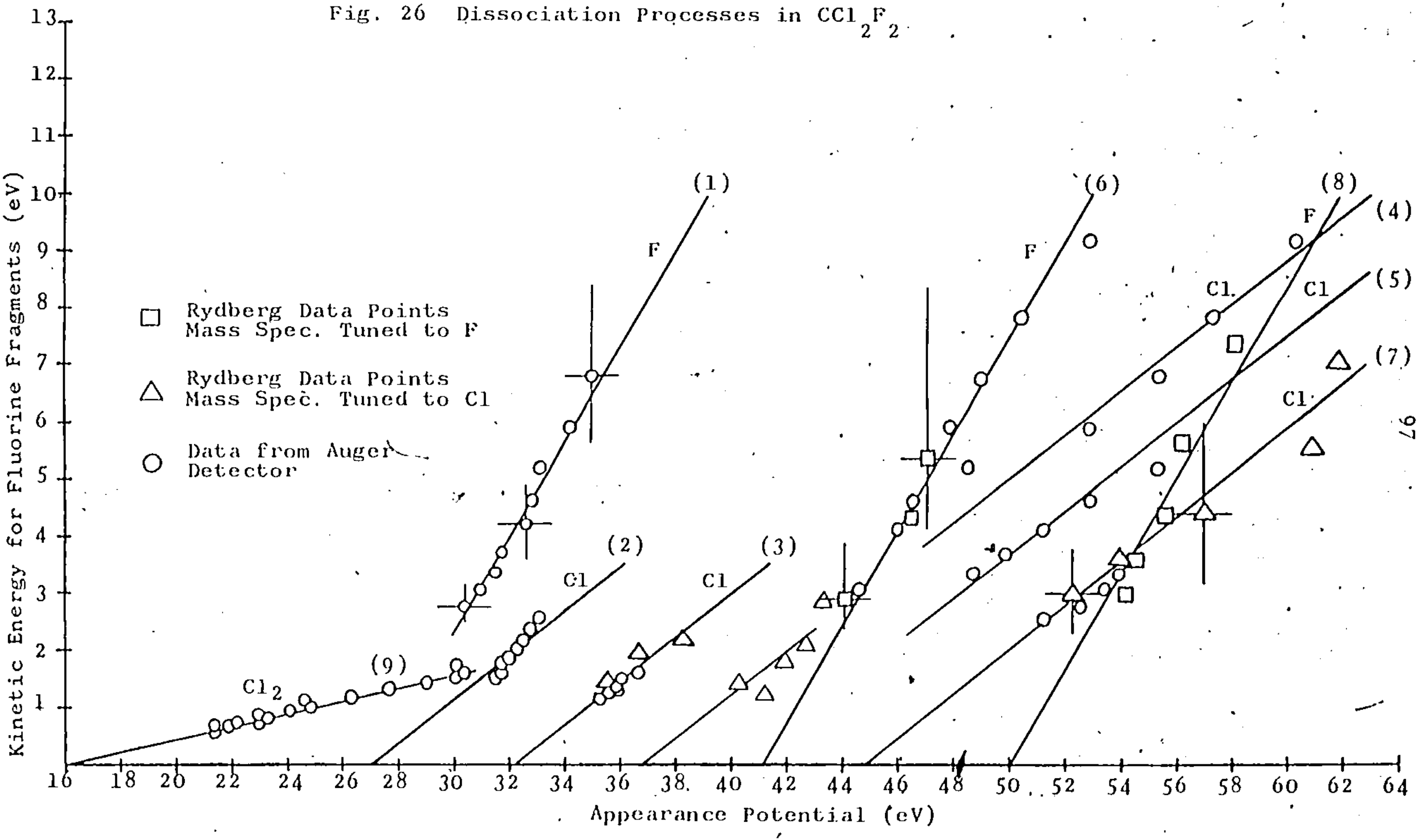

Fig. 26 Dissociation Processes in $CCl_2F_2$

Processes (1), (6) and (8) produce a detectable F atom during a two-fragment dissociation of the parent molecule. A line of slope 0.84 has been drawn through the points in each case (this is the expected slope if the fragment is an F atom). Any other possible fragment, with the exception of C, would have a larger mass and hence a much lower value of slope than the above. Carbon fragments may also be excluded since the production of these fragments involves a multiple fragmentation of the parent molecule and hence a totally different behaviour (see later). The production of F atoms by processes (6) and (8) has been confirmed by the mass sensitive Rydberg detector. The fluorine Rydberg data points are shown as open squares.

The data points for processes (3), (4), (5) and (7) appear to lie quite well on lines of slope 0.38. This is the correct slope for the production of a detectable Cl atom during a two-fragment dissociation process. Although the data points for process (2) appear to lie on a line of slightly greater slope than 0.38, it is very likely that this process also involves the production of chlorine atoms during a two-fragment breakup (see later). The production of Cl atoms by processes (3), (4) and (7) has been confirmed by the Rydberg detector. The chlorine Rydberg data points are shown as open triangles.

The data points for process (9) lie on a line of much smaller slope, 0.11. This is the correct slope for a two-fragment dissociation process if the detected fragment is a

$Cl_2$ molecule. This possibility is discussed later.

For clarity, the data points from the F and Cl producing processes, in $CCl_2F_2$, are displayed separately in Figs. 27(a) and 27(b) respectively. Similar data points were obtained during the study of $CCl_3F$ and are displayed in Figs. 28(a) and 28(b) respectively. The kinetic energy scales shown in the figures correspond to the actual detected fragment. The figures clearly illustrate the similarity between dissociation mechanisms in the two gases since many of the dissociation processes in $CCl_3F$ have similar dissociation limits to those observed in $CCl_2F_2$. In addition, the processes produce fragments with similar ranges of kinetic energy. Many of these ranges cover an energy in excess of 6 eV. This suggests that the corresponding potential curves are strongly repulsive within the Franck-Condon region. In both gases the strong overlap of the kinetic energy ranges results in the broad and often structureless distributions of Figs. 18-20.

Figs. 27 and 28 also show the appearance potentials which were obtained during D.C. operation of the electron gun. These appearance potentials, which are indicated by arrows on the appearance potential axis, were obtained by using the Rydberg detector tuned to Cl and F as shown in each case. Where an appearance potential is likely to correspond to one of the previously observed processes, it has been labelled with the appropriate number. These appearance potentials lie quite close to the corresponding dissociation limits. A number of

Fig. 27(a) Fluorine Producing Processes in $CCl_2F_2$

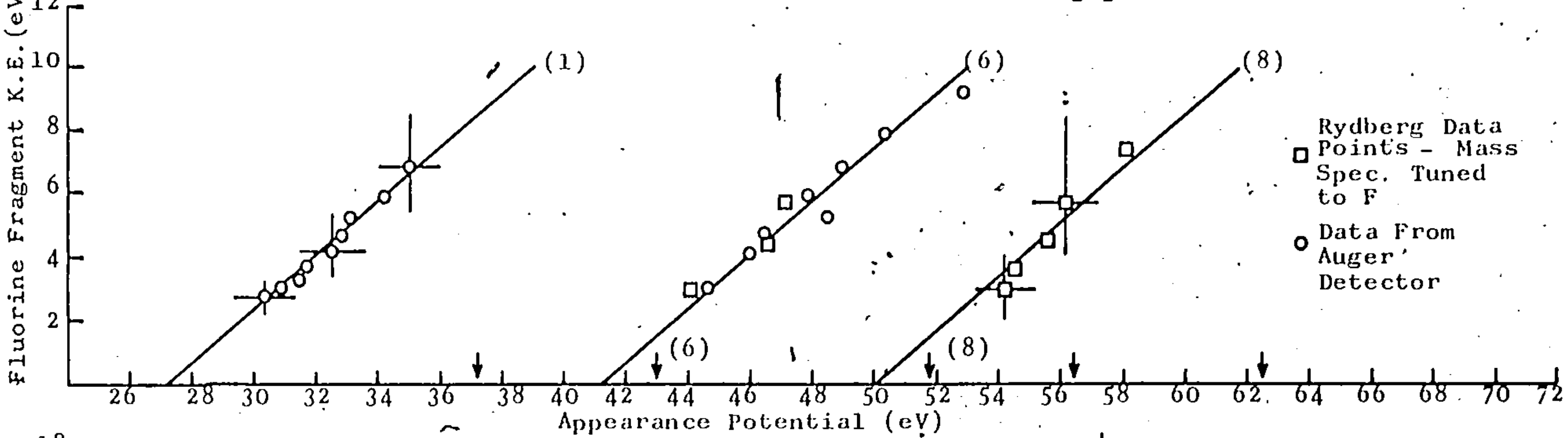

Fig. 27(b) Chlorine Producing Processes in $CCl_2F_2$

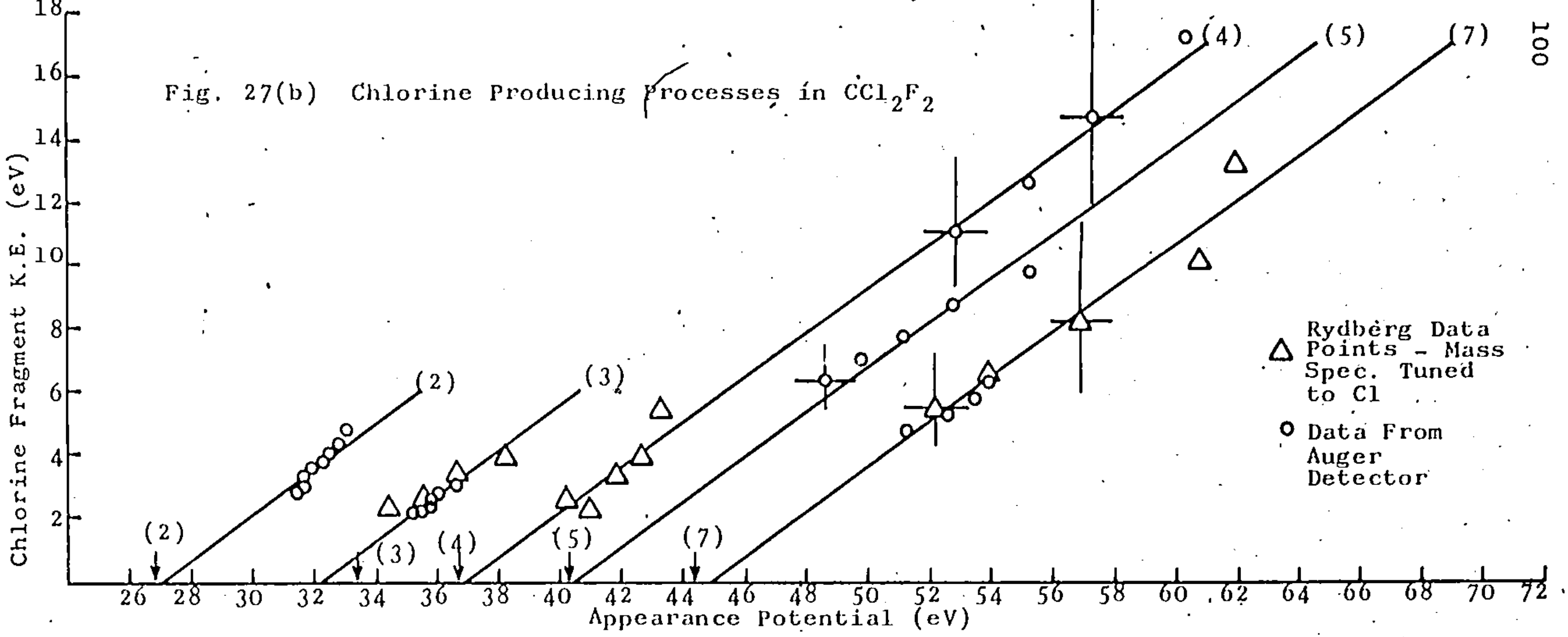

Fig. 28(a) Fluorine Producing Processes in $CCl_3F$

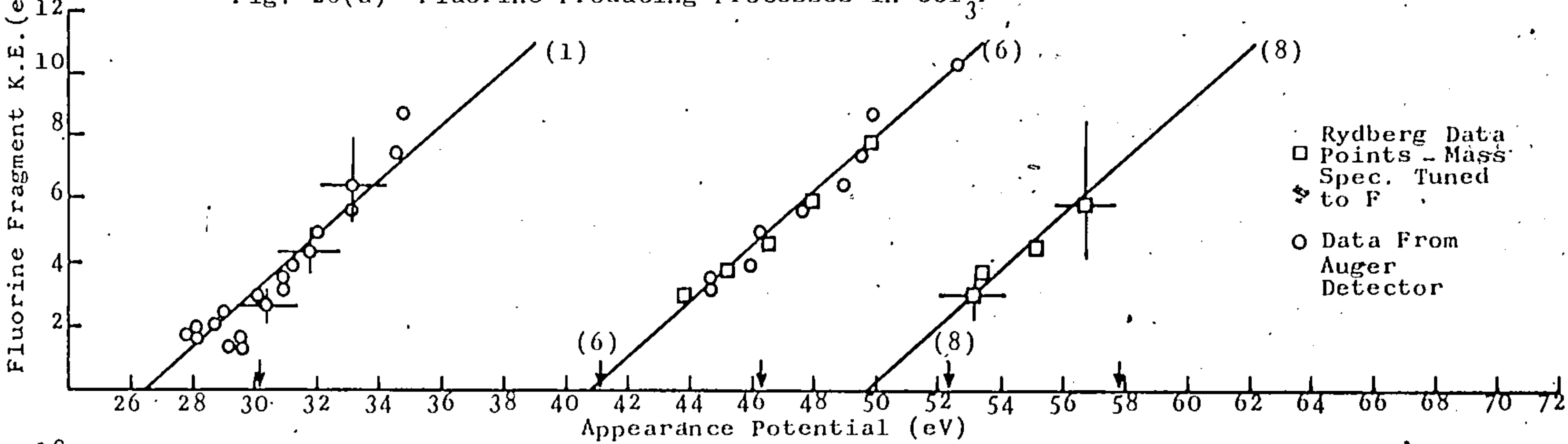

Fig. 28(b) Chlorine Producing Processes in $CCl_3F$

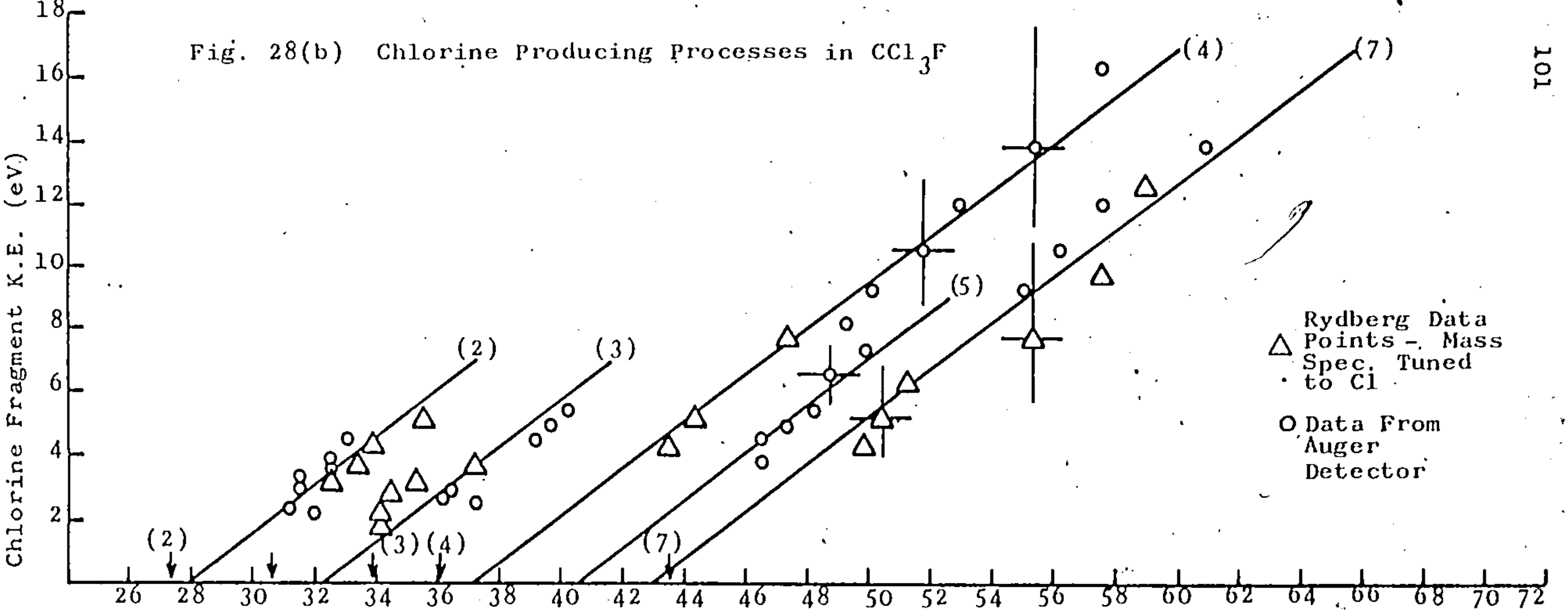

additional weak processes were also observed. These are indicated by unlabelled arrows.

In Fig. 29 the kinetic energy of the Rydberg carbon atoms produced during the dissociation of $CCl_2F_2$ is plotted against fragment appearance potential. Each of the four observed processes produce fragments with a range of kinetic energies, but with the same appearance potential. This behaviour suggests that multiple fragmentations of the parent molecule are occurring (see section 1.4 of Chapter 1) and is consistent with the fact that all four carbon bonds must be broken in order to release a carbon atom from the molecule. Little information can be obtained about these dissociation processes since the total kinetic energy released during the dissociation remains an unknown.

The relevant data from each dissociation process is summarized in Table 2. The F and Cl producing processes are numbered 1 to 8 in order of increasing dissociation limit and the C-Rydberg producing processes are numbered 10 to 13 in order of increasing appearance energy.

## 4.3 Discussion of the Results for $CCl_2F_2$ and $CCl_3F$

### 4.3.1 Introduction

Difficulties arise in satisfactorily interpreting the data presented because the processes have onset energies above 21 eV where there is very little data available for use or comparison. For example, only two mass spectroscopic

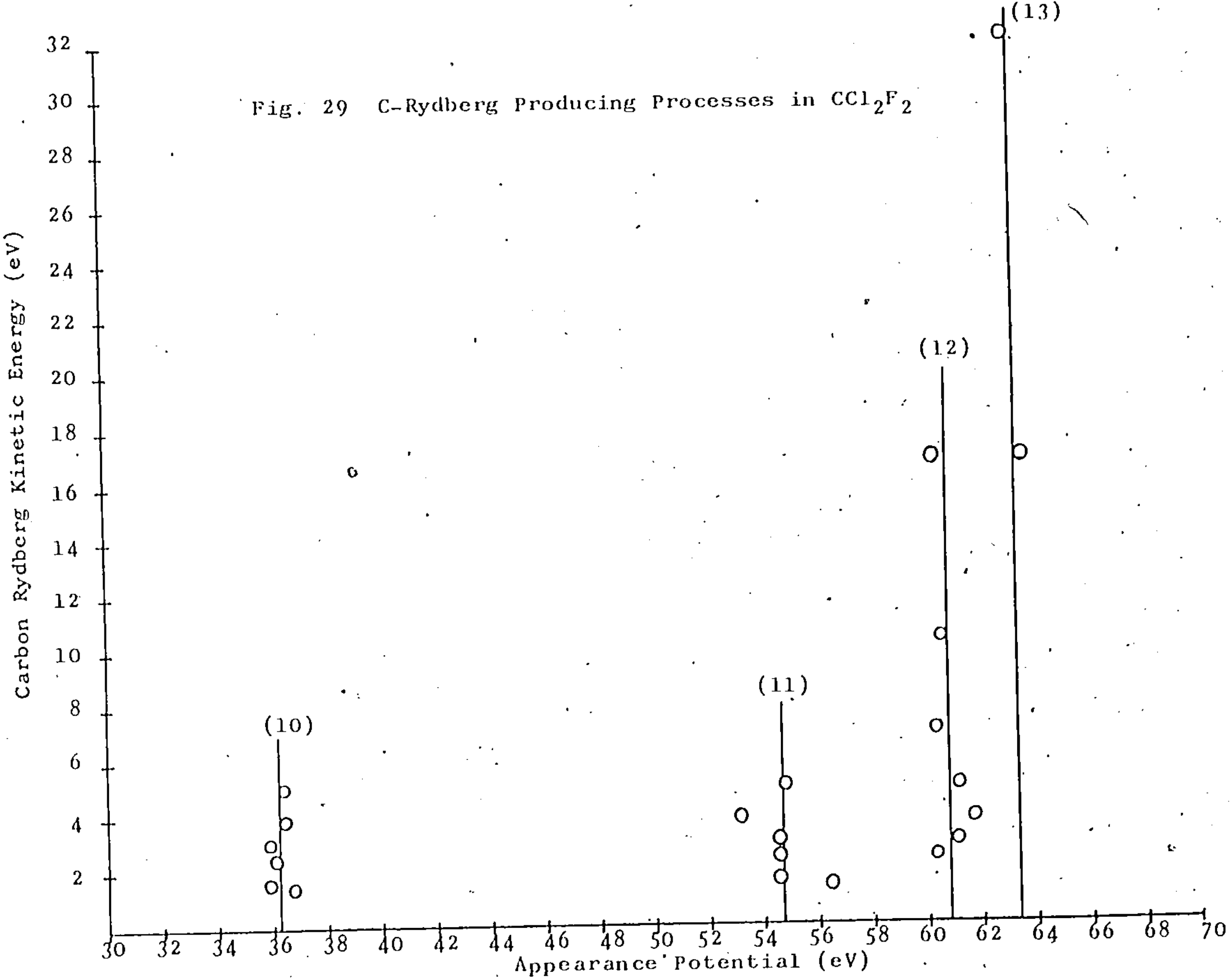

Fig. 29 C-Rydberg Producing Processes in $CCl_2F_2$

TABLE 2. The experimental results for $CCl_2F_2$ and $CCl_3F$.

| Process Number | Detected* Fragment | Dissociation Limit ± 1.0 eV | | Rydberg D.C. App. Pot. ± 1.0 eV | |
|---|---|---|---|---|---|
| | | $CCl_2F_2$ | $CCl_3F$ | $CCl_2F_2$ | $CCl_3F$ |
| 1. | $F(3s^4P_{5/2})$ | 27.3 | 26.6 | - | - |
| 2. | Cl(R) | 27 | 27.9 | 26.8 | 27.4 |
| 3. | Cl(R) | 32.2 | 32.3 | 33.4 | 33.9 |
| 4. | Cl(R) | 36.7 | 37.2 | 36.7 | 36.1 |
| 5. | Cl(R) | 40.5 | 40.6 | 40.3 | - |
| 6. | F(R) | 41.2 | 40.9 | 43 | 41 |
| 7. | Cl(R) | 44.9 | 43 | 44.4 | 43.5 |
| 8. | F(R) | 50 | 49.7 | 51.8 | 52.3 |
| 9. | $Cl_2(C^3\Sigma_{iu})$ | 16.1 | - | - | - |
| 10. | C(R) | 36.2 | Mean Appearance Potential | | |
| 11. | C(R) | 54.7 | | | |
| 12. | C(R) | 60.8 | | | |
| 13. | C(R) | 63.3 | | | |
| Additional Weak Processes | F(R) | - | - | 37.2 | 30.1 |
| | F(R) | - | - | 56.4 | 46.3 |
| | F(R) | - | - | 62.5 | 57.8 |
| | Cl(R) | - | - | - | 30.6 |

* Fragments in Rydberg states are designated by the letter R, e.g. Cl(R).

studies of ionization in $CCl_2F_2$ and $CCl_3F$ have been reported (Ajello et al. 1976; Jochims et al. 1976) and the molecular ion appearance potentials presented in these are limited to energies below 24 eV.

Vacuum U.V. absorption and photoionization experiments on these gases were carried out by Doucet et al. (1973), Gilbert et al. (1974) and Person et al. (1975), but again no data was obtained for incident photon energies greater than 21 eV. In addition, the electron impact photon simulated data of Huebner et al. (1975) only extended up to 20 eV.

Very recently, King and McConkey (1977) have extended the electron impact forward scattering data for $CCl_2F_2$ and $CCl_3F$ and have been able to study the variation of the optical oscillator strength up to 'photon' impact energies of approximately 40 eV. They find that the oscillator strength falls off monotonically above 20 eV with very little sign of any structure. This, of course, might be expected in view of the breadth of the energy ranges involved for processes leading to dissociation and also in view of the small values of the relevant cross sections.

Of particular interest for comparison with the present Rydberg data would have been information on fragment ion kinetic energies. This is because of the often close correspondence between dissociative excitation to Rydberg states and dissociative ionization (see section 1.6 of Chapter 1). Unfortunately, no such information is available at the present time.

Despite these limitations considerable progress has been made in analyzing the data as discussed below.

### 4.3.2 Fluorine Fragment Processes

Process (1) is clearly present in the data from $CCl_2F_2$ and $CCl_3F$. The dissociation limits obtained agree to within the experimental error [see Table 2 and Figs. 27(a) and 28(a)]. The process produces non-Rydberg metastable fluorine atoms. The only possible state of F which has a long enough lifetime to enable it to reach the detector is the 3s $^4P_{5/2}$ state. This has a calculated lifetime of 48.7 μs (Gruzdev, 1971). The fact that a metastable state of F is observed following a TOF of this order is a direct check on these calculations.

Assuming an excitation energy of this state of 12.7 eV and a C–F bond strength of 4.4 eV (bond strength in $CCl_3F$; Cottrell, 1962), we are left with over 9 eV to be accounted for in terms of electronic excitation energy of the other fragment. This almost certainly goes towards the release of an electron. Hence a likely process is

$$e + CCl_2F_2 \longrightarrow CCl_2F^+ + F(3s\,^4P_{5/2}) + 2e \qquad (17)$$

for $CCl_2F_2$ and

$$e + CCl_3F \longrightarrow CCl_3^+ + F(3s\,^4P_{5/2}) + 2e \qquad (18)$$

for $CCl_3F$.

These suggestions are supported by the work of

Person et al. (1975), Huebner et al. (1975) and King and McConkey (1977). They demonstrate that essentially all of the optical oscillator strength in $CCl_2F_2$ and $CCl_3F$ is associated with ionization at energies above 12 eV.

Unfortunately, no data is available which can be directly compared with the dissociation limits of process (1). However, if the excitation energy of $F(3s\,^4P_{5/2})$ (12.7 eV) is subtracted from the measured dissociation limits (see Table 2), then it is possible to predict the existence of onsets in the molecular ion signal intensity at 14.6 eV and 13.9 eV respectively. Although these appearance potentials are likely to correspond to lower limits of the experimental values (since they correspond to the production of fragments with zero kinetic energy), such thresholds were observed by Ajello et al. (1976) and Jochims et al. (1976) at very similar energies to the above. Ajello et al. observed thresholds for the production of $CCl_2F^+$ and $CCl_3^+$ and 13.81 eV and 13.25 eV respectively. Jochims et al. quote values for the same thresholds of 14.15 eV and 13.5 eV respectively.

The wide range of fragment energies observed suggests that the excitation takes place to a surface which is strongly repulsive within the Franck-Condon region. There are some indications, from the shape of the excitation functions (Fig. 21) that the initial excitation process involves a change in multiplicity.

Processes (6) and (8) have both been identified as producing F-Rydberg fragments in $CCl_2F_2$ and $CCl_3F$. The measured dissociation limits again compare very well. In both processes, fragments with a wide range of kinetic energies are produced. This suggests as before that the excitation occurs to a steeply repulsive surface. It is very likely that these processes involve high Rydberg states of the parent molecule corresponding to multiply ionized, and possibly excited cores. No data is available on $F^+$ production in this energy region for comparison. A F(R) based on $F^+(^3P)$ would possess approximately 17.4 eV excitation energy. Thus, from energetic considerations, it is likely that the other fragment produced in each case is an excited ion as indicated below.

$$e + CCl_2F_2 \longrightarrow (CCl_2F^+)^* + F(R) + 2e \qquad (19)$$

$$e + CCl_3F \longrightarrow (CCl_3^+)^* + F(R) + 2e \qquad (20)$$

Multiply ionized fragments may also be produced.

The fluorine Rydberg kinetic energy spectra shown in Fig. 18 clearly illustrate the similarity between the results from $CCl_2F_2$ and $CCl_3F$. As may be expected from its structure, the F(R) signal intensity from $CCl_2F_2$ is greater than that from $CCl_3F$. Processes (6) and (8) are known to produce fragments with similar kinetic energies and are responsible for two strongly overlapping features. The large broad peak which extends from high fragment energies down to less than 2 eV is the result of this overlap. Structure in this peak is visible at low electron energies in the $CCl_3F$ data (see 75 eV and 60 eV curves). At an electron energy of 60 eV the signal in this region is dominated by process (6), since this has the lower dissociation limit. However, by 75 eV a broadening is clearly visible. This is due to process (8). At low kinetic energies an additional feature is visible. This feature appears to be much narrower than the other two and is present at low electron energies. It is likely that the process or processes responsible for this feature have not been previously identified. It should be noted that a number of unidentified processes which produce F-Rydbergs were observed during D.C. operation of the electron gun. Some of these have low dissociation limits and may be responsible for this feature [see Figs. 27(a) and 28(a)]. Although little can be said about these processes, the D.C. onset obtained at about 30 eV in the $CCl_3F$ data is of interest, since a similar onset has been observed for $F^+$ production from $CClF_3$. Franklin et al. (1969) list a 31 eV onset for this dissociative ionization process.

### 4.3.3 Chlorine Fragment Processes

Processes (2), (3), (4) and (7) produce Cl-Rydberg atoms during a two fragment breakup of $CCl_3F$ [see Fig. 28(b)]. Similarly, processes (3), (4) and (7) are known to produce Cl-Rydbergs during the breakup of $CCl_2F_2$ [see Fig. 27(b)].

In addition, there is some evidence to suggest that process (2) in $CCl_2F_2$ and process (5) in both gases, may also be included in the above assignment (see later). The dissociation limits obtained for both gases agree to within the experimental error with the possible exception of process (7) (Table 2). A Cl(R) based on $Cl^+(^3P)$ would possess approximately 13.0 eV excitation energy and thus from energetic considerations, it is likely that the other fragment produced in each case is an excited ion as indicated below.

$$e + CCl_2F_2 \longrightarrow (CClF_2^+)^* + Cl(R) + 2e \qquad (21)$$

$$e + CCl_3F \longrightarrow (CCl_2F^+)^* + Cl(R) + 2e \qquad (22)$$

Multiply ionized fragments may also be produced where the dissociation limits are sufficiently high.

Unfortunately, no data is available which can be directly compared with the dissociation limits of these processes. However, if the excitation energy of the Cl(R) atom is subtracted from the measured dissociation limits of processes (2) and (3), then it is possible to predict values for two of the higher ionization potentials of the parent molecules. These values may be compared with published data. The ionization potentials obtained are 14.0 eV and 19.2 eV in $CCl_2F_2$ and 14.9 eV and 19.3 eV in $CCl_3F$. Although these values are only approximate (due to the fact that they correspond to the dissociation limits of states which may be either repulsive or bound), they do compare favourably with the ionization potentials given by Doucet et al. (1973). They give values of 14.4 eV and 19.0 eV in $CCl_2F_2$ and 14.9 eV and 18.2 eV in $CCl_3F$. The more recent values of Jochims et al. (1976) are in very close agreement with these. It is known that some of the higher ionization potentials of $CCl_2F_2$ and $CCl_3F$ are associated with the C-F bond (Gilbert et al. 1974).

There is some uncertainty in concluding that process (2) produces Rydberg Cl atoms in $CCl_2F_2$. This is because Rydberg data points could not be obtained during pulsed operation of the electron gun. The assignment of a Cl-Rydberg to this process in $CCl_2F_2$ is based on the presence of an onset in the D.C. excitation function data [see Fig. 27(b)] and on the general similarity between the results from the two gases (see Figs. 27 and 28).

Despite similar uncertainty, it is likely that process (5) produces Rydberg Cl atoms in both gases. This is because the slopes of the lines obtained correspond to the production of chlorine atoms and non-Rydberg species may be excluded using lifetime arguments. For example, the lifetime of the 4s ($^4P_{5/2}$) state in Cl (which is equivalent to the 3s ($^4P_{5/2}$) state in F) is only 5 $\mu$s (Weise et al. 1969). Chlorine fragments in this state would decay before reaching the detector. Less speculative evidence for the nature of process (5) is provided by a Cl-Rydberg onset obtained during D.C. operation of the electron gun [see the results for $CCl_2F_2$ in Table 2 and Fig. 27(b)].

The Cl-Rydberg kinetic energy spectra shown in Fig. 19

again illustrate the similarity between the results from $CCl_2F_2$ and $CCl_3F$. As may be expected, the signal intensity from $CCl_3F$ is greater than that from $CCl_2F_2$. Processes (4), (5) and (7) are responsible for the broad high energy feature which is very much reduced at low electron energies. The two low energy features are much narrower and are due to processes (2) and (3).

### 4.3.4 Carbon Fragment Processes

Very little can be said about the dissociation processes which result in the production of a detectable carbon atom, since they necessarily involve a multiple fragmentation of the parent molecule with the breaking of all four carbon bonds. In such a situation, measurement of the kinetic energy of one fragment provides no information about the total kinetic energy released during the breakup. For this reason, excitation function data was only recorded for the carbon fragments produced during the dissociation of $CCl_2F_2$. The only carbon atoms detected during the experiment were in Rydberg states. These fragments were detected with a range of kinetic energies as soon as sufficient energy was supplied to the parent molecule to cause the breakup (see Fig. 29). This is because sharing of the total kinetic energy released during the dissociation is not constrained by the conservation of momentum and energy. Four different dissociation processes are displayed in Fig. 29. Each of these processes has a different onset energy since the undetected fragments produced in each case possess different amounts of electronic excitation energy. The amount of energy involved remains an unknown. Similarly, it is not known whether any of the undetected atoms come together to form molecules during the breakup.

The carbon Rydberg kinetic spectra for both $CCl_2F_2$ and $CCl_3F$, which are shown in Fig. 20, show some evidence of structure, but provide little additional information. The excitation functions, shown in Fig. 25, show some evidence of curvature above threshold. This suggests that the initial excitation of the parent molecule involves a change in multiplicity in some instances.

### 4.3.5 The $Cl_2$ Fragment Process

Process (9) was observed during the dissociation of $CCl_2F_2$, but only very weakly during the dissociation $CCl_3F$. The slope analysis (Fig. 26) suggests that a $Cl_2$ molecules is produced during a two-fragment dissociation. The molecule must be in a metastable state since Rydberg data points could not be obtained. Such processes involving the production of two molecular fragments are not unknown. Schiavone et al. (1977), Ajello et al. (1976) and Jochims et al. (1976) present strong evidence to suggest the presence of such processes in their work. In addition, it should be noted that excited $CF_2$ molecules [the undetected fragments produced by process (9)] have been observed during the photo-dissociation of fluoromethanes (Herzberg, 1966).

The measured dissociation limit for process (9) is 16.1 eV. It is straightforward to show that the dissociation is energetically feasible if the $Cl_2$ molecule is in the $C^3\Sigma_{iu}$ state (excitation energy 7.2 eV) and the $CF_2$ molecule is in the $\tilde{A}(^1A_1)$ state (excitation energy 4.7 eV). The calculation, which assumes a dissociation energy of 2.5 eV for the $Cl_2$ molecule, predicts an average C-Cl bond energy in $CCl_2F_2$ of 3.4 eV. This value is consistent with the data given by Cottrell (1962) for other freon molecules. Values range between 2.95 eV ($CCl_4$) and 3.60 eV ($CF_3Cl$). The suggested fragmentation process in $CCl_2F_2$ is thus,

$$e + CCl_2F_2 \longrightarrow CF_2(\tilde{A}\ ^1A_1) + Cl_2(C^3\Sigma_{iu}) + e\ . \qquad (23)$$

Unfortunately, no lifetime data exists for $Cl_2(C^3\Sigma_{iu})$ to test this hypothesis.

# CHAPTER 5

# THE RESULTS FOR $N_2O$

## 5.1 Introduction

Nitrous oxide has become one of the most studied triatomic molecules in the vacuum - U.V. region in recent years. Interest has centered on $N_2O$ not only as a molecule in its own right, but also because a great many aeronomically important metastable species are produced as photolysis products during vacuum - U.V. irradiation. Among the excited species that have been identified are $N(^2D)$, $O(^1S)$ and $O(^1D)$ excited atoms and $N_2(A\ ^3\Sigma_u^+)$ and $N_2(B\ ^3\pi_g)$ excited molecules [Young et al. (1968 and 1969); Gilpin and Welge (1971); Hampson and Okabe (1970); McEwan et al. (1974); Black et al. (1975); Brom and Broida (1975); Lee et al. (1975)].

A number of workers have studied the dissociation of $N_2O$ by electron impact. Freund and Klemperer (1967) observed the production of metastable $N_2(A\ ^3\Sigma_u^+)$ molecules with an appearance potential of $8.7^{a}$eV. The other fragment produced was a $^3P$ oxygen atom. Clampitt and Newton (1969) also observed the production of excited $N_2$ molecules. They measured a dissociation limit of 9.95 eV for an $N_2$ producing process and suggest that the dissociation channel produces either an $N_2(B'\ ^3\Sigma_u^-)$ molecule or an $N_2(a\ ^1\pi_g)$ molecule. The other fragment produced in each case being an $O(^3P)$ atom. The workers point out that the $B'\ ^3\Sigma_u^-$ state would cascade into the $A\ ^3\Sigma_u^+$ state.

A number of studies of dissociative ionization in $N_2O$ have also been made. In particular, Curran and Fox (1961) measured appearance potentials for the production of $O^+$ and $N^+$

ions. Very little work has been done on the higher energy dissociation processes in $N_2O$.

In the present work both metastable atomic and molecular fragments were observed. The corresponding dissociation processes have been studied systematically and the results are presented in this chapter. Many of the dissociation processes have high dissociation limits.

## 5.2 Description of the Results for $N_2O$

### 5.2.1 Fragment Signal Intensity as a Function of Gas Pressure and Electron Current

A plot of fragment signal intensity (integrated over all relevant flight times) against gas-beam head pressure was recorded for $N_2O$ using the Auger detector. The plot, which was obtained at an electron energy where all the dissociation processes are contributing to the observed signal (100 eV), is similar in shape to the pressure plot obtained for $CO_2$ (see Fig. 9) and is not presented here. The gas-beam head pressure used during time-of-flight and excitation function data taking was 0.05 torr. Research grade $N_2O$ was used throughout these studies. The minimum purity being 99%.

A plot of fragment signal intensity against electron current was also recorded for $N_2O$. The plot, which shows a linear relationship for electron currents below 145 $\mu$A, was similar to the electron current plot obtained for $CO_2$ (see Fig. 10) and is not presented here. In general, an 8 $\mu$A electron current was used during data taking. Space charge effects were found to be negligible at this electron current.

### 5.2.2 Time-of-Flight and Kinetic Energy Distributions

Time-of-flight spectra of the dissociation fragments produced during the breakup of $N_2O$ are shown in Fig. 30. The data was obtained during use of the Auger detector at the electron energies quoted. The spectra, which are intensity normalized, clearly show the presence of a large broad peak at long flight times. This peak dominates the time-of-flight spectrum at low electron energies and was still visible at an electron energy of 10 eV. Excitation function data (see later) indicates that this peak is mainly due to the detection of metastable $N_2$ molecules. As before, the numbering scheme refers to the dissociation processes which contribute signal to the various features. There is some evidence of structure in the leading edge of this peak at high electron energies (see 75 eV and 100 eV curves). Above an electron energy of about 40 eV an additional peak is clearly visible at short flight times. This peak rapidly increases in intensity with increasing electron energy until, by 100 eV, it dominates the time-of-flight spectrum. Excitation function data indicates that this peak is due to the detection of excited oxygen and nitrogen atoms. Kinetic energy transformations of the fast peak are not presented because of the different masses involved. However, kinetic energy transformations of the $N_2$ peak, obtained at two different electron energies, are presented in Fig. 31.

In this figure the 12 eV spectrum reaches a sharp

Fig. 30 Time-of-Flight Spectra for $N_2O$

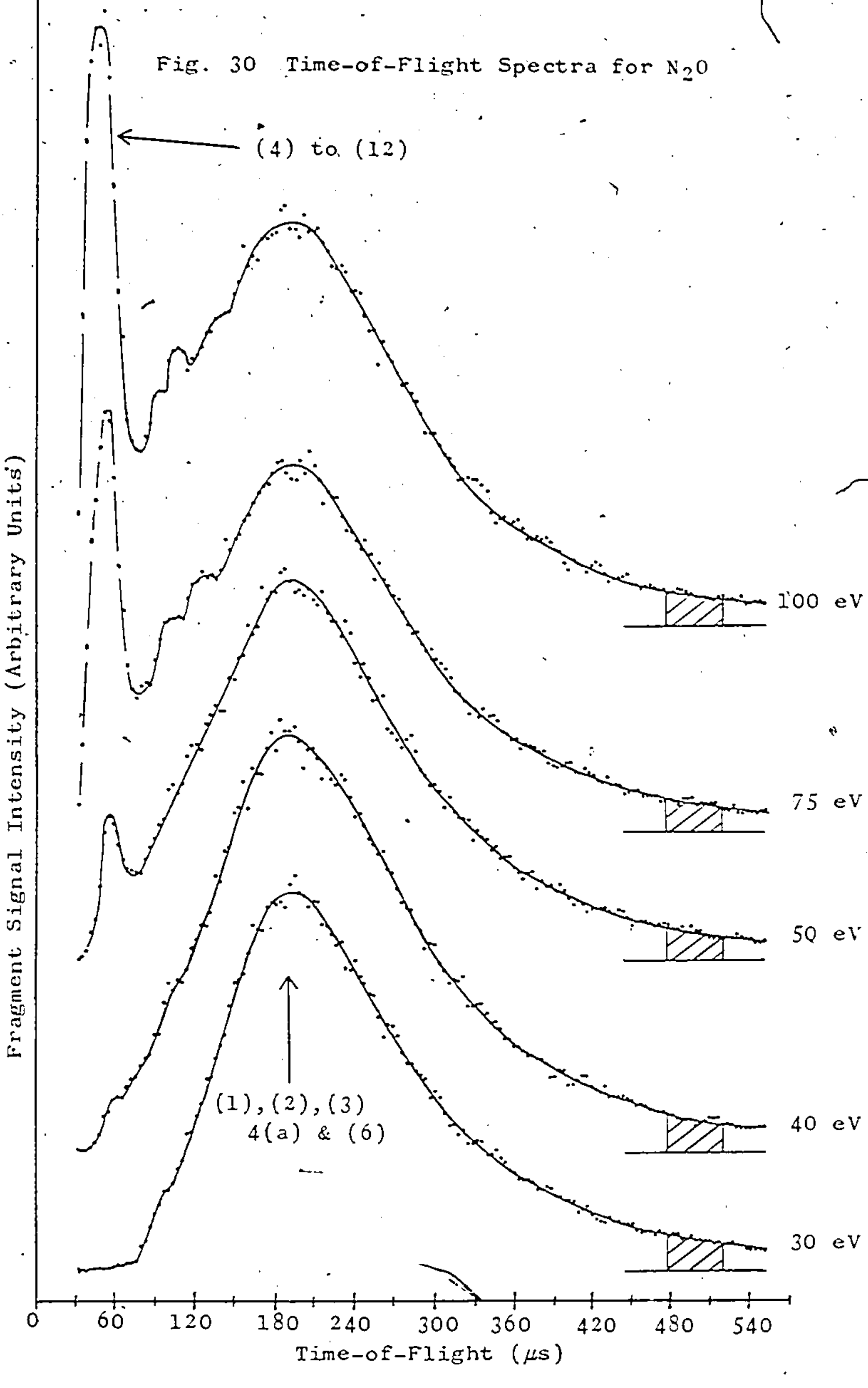

Fig. 31 $N_2$ Fragment K.E. Spectra for $N_2O$

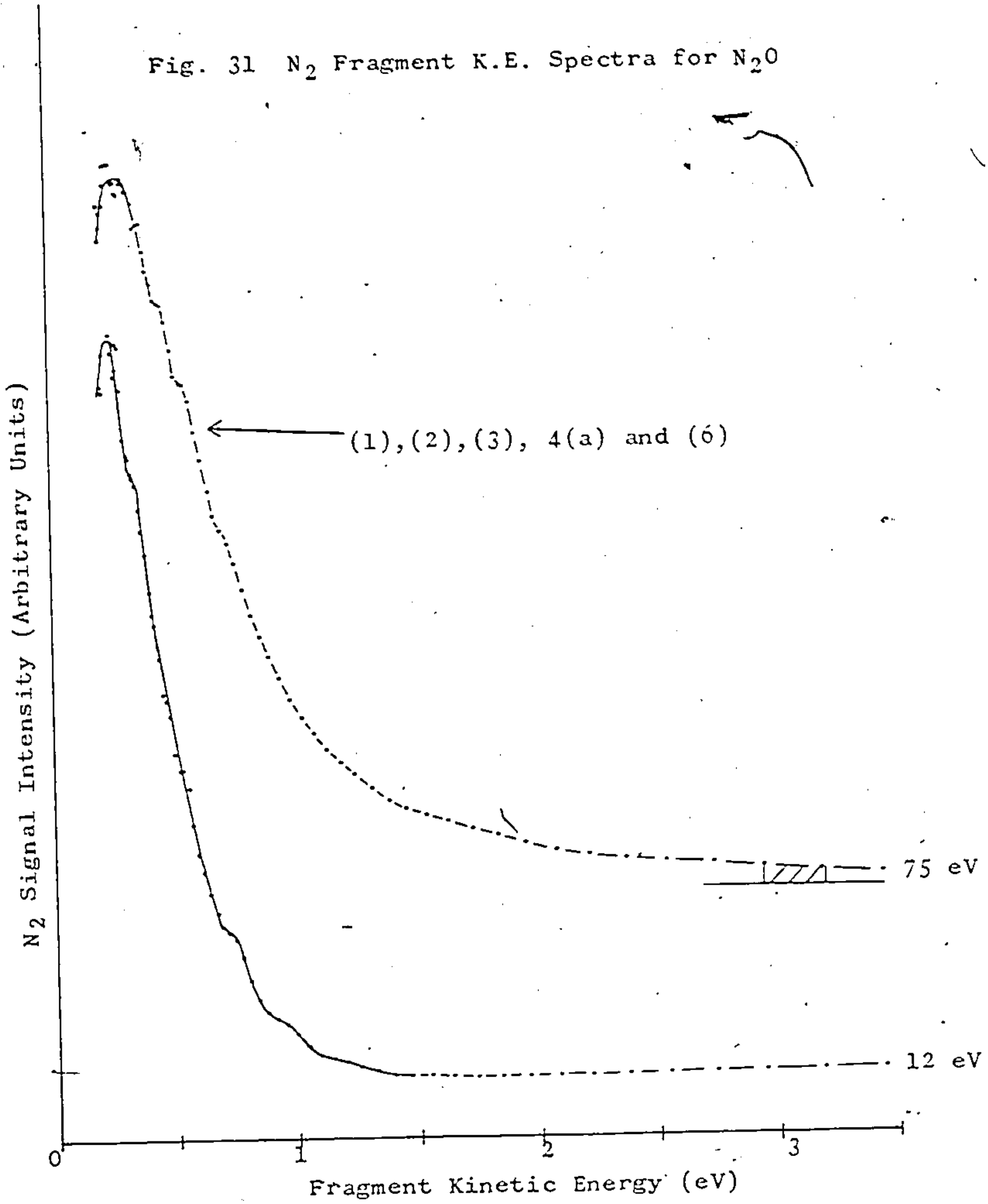

maximum at a kinetic energy of about 0.27 eV. By an electron energy of 75 eV the peak appears to be much broader. This suggests that a number of dissociation processes contribute signal to the $N_2$ peak. There is some evidence of structure in both curves which supports this suggestion.

Time-of-flight spectra were also recorded at different electron energies for the oxygen and nitrogen Rydberg atoms produced during the dissociation of $N_2O$. The corresponding kinetic energy spectra are shown in Fig. 32 and Fig. 33 respectively. The spectra in each figure, which are intensity normalized, show some evidence of structure indicating that a number of different dissociation processes produce Rydberg atoms in $N_2O$. The numbering scheme refers to the dissociation processes which are possibly responsible for the various features. The assignment cannot be made with certainty because of the strong overlap of the kinetic energy features.

### 5.2.3 Excitation Functions

A number of excitation functions, corresponding to different fragment flight times, are shown in Fig. 34. The data was obtained during use of the Auger detector. The lowest two excitation functions correspond to flight times well within the broad $N_2$ peak of Fig. 30. The kinetic energies quoted for these excitation functions were calculated assuming that the detected fragments were $N_2$ molecules. Dissociation limit analysis and slope analysis of a plot of fragment kinetic energy

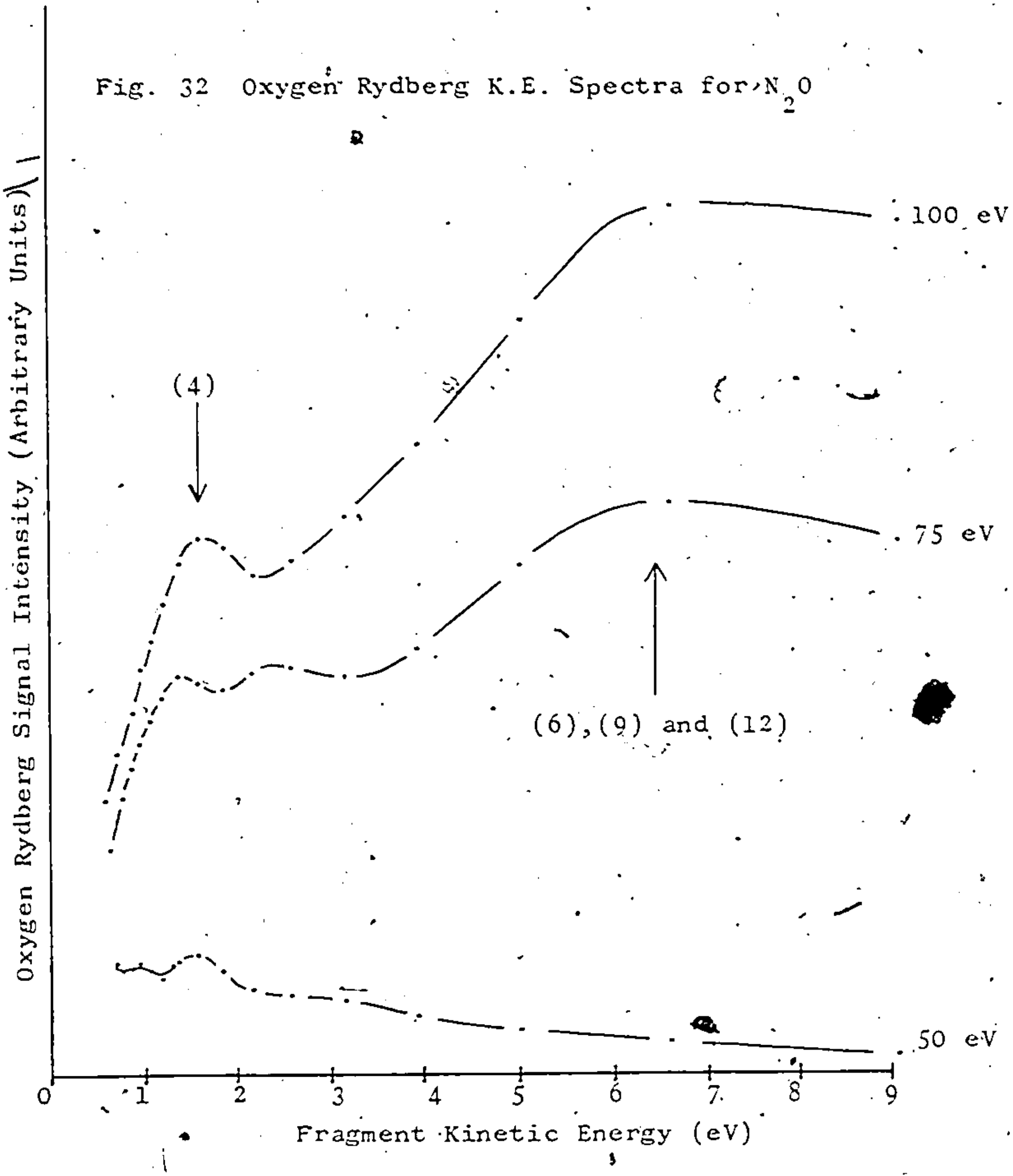

Fig. 32 Oxygen Rydberg K.E. Spectra for $N_2O$

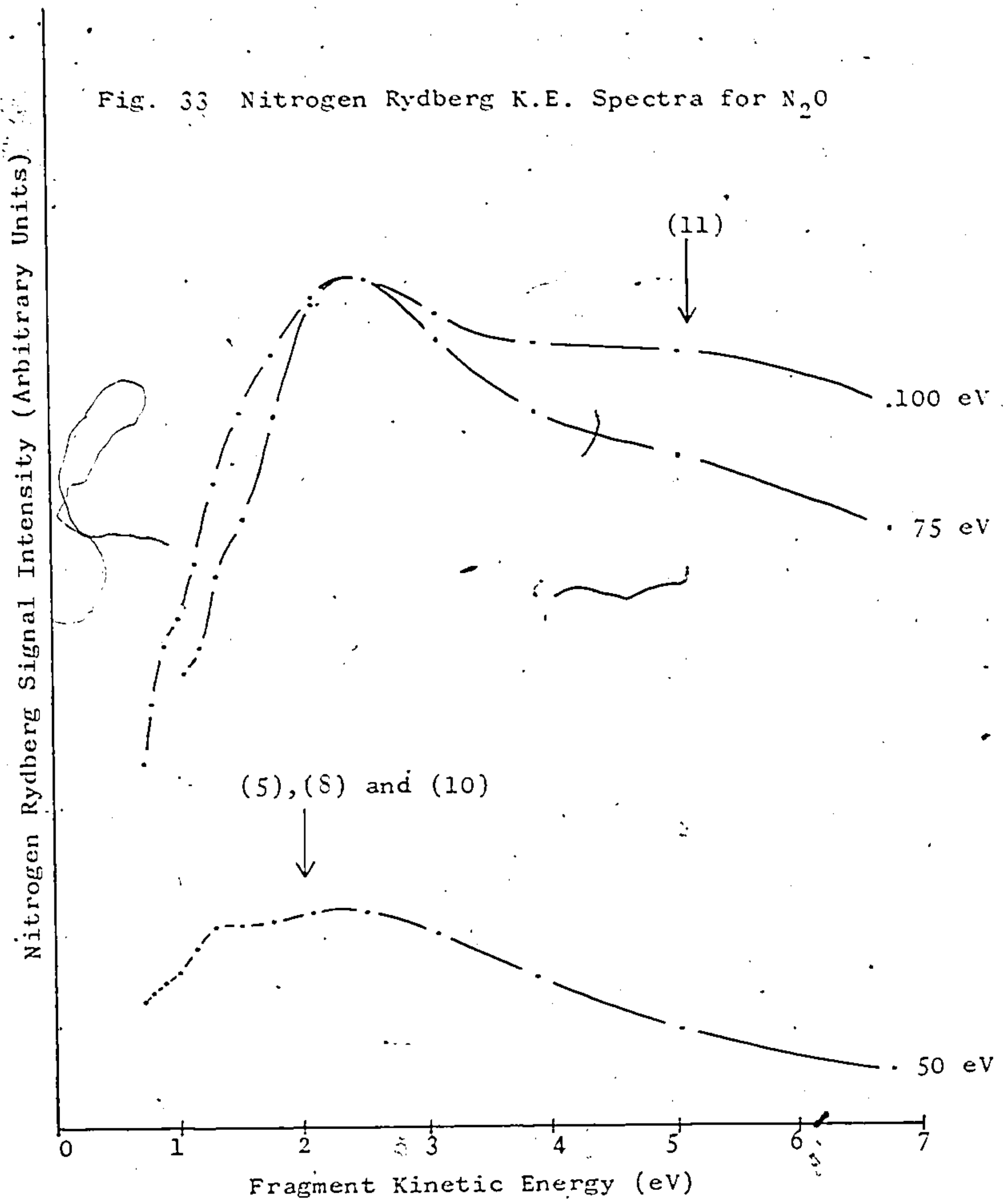

Fig. 33 Nitrogen Rydberg K.E. Spectra for $N_2O$

Fig. 34 Excitation Functions for $N_2O$

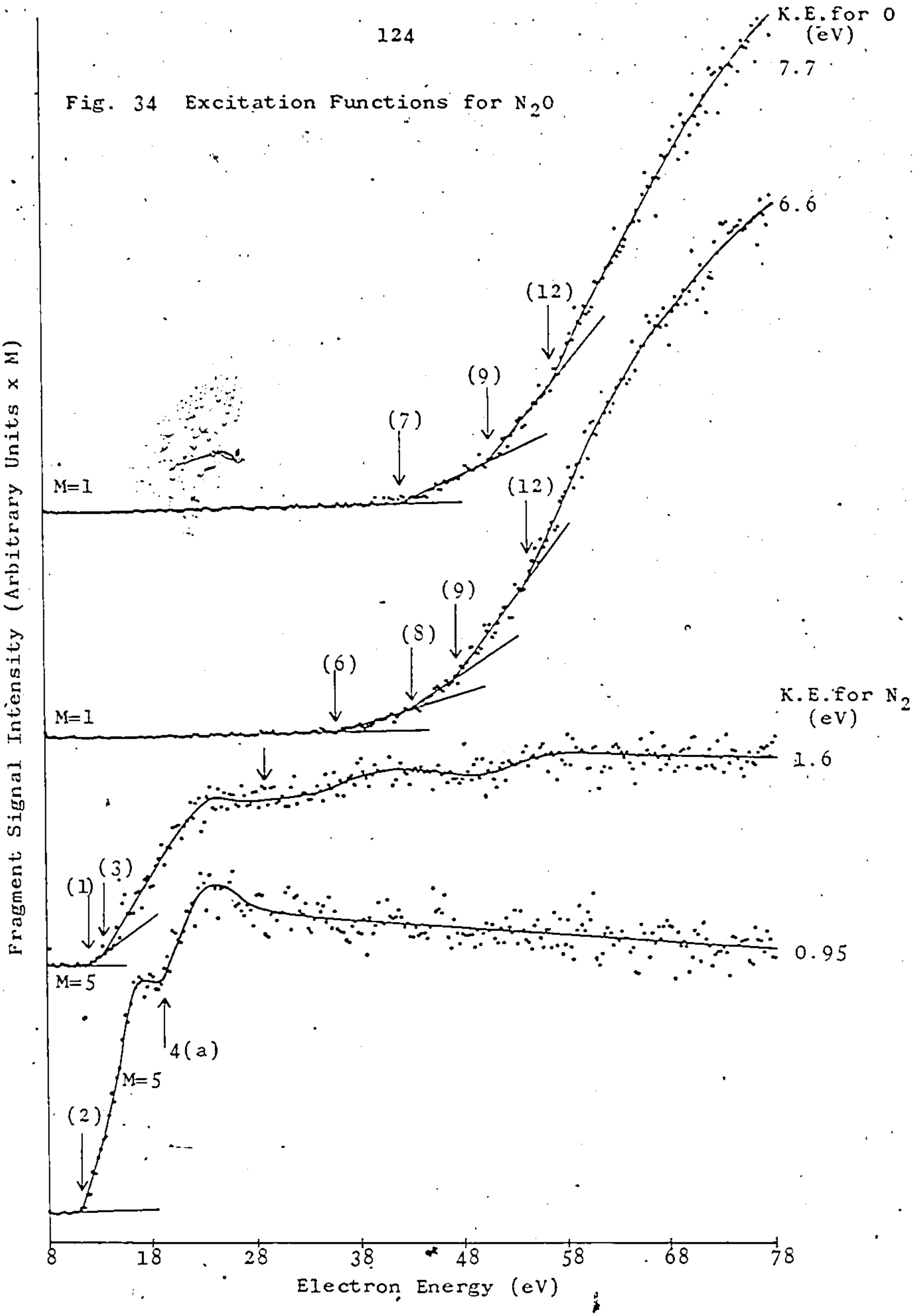

against appearance potential verified this assumption. The excitation functions appear to peak sharply above threshold suggesting that at least two of the dissociation processes involve a change in multiplicity during the initial excitation (see later). The remaining excitation functions shown in Fig. 34 correspond to flight times in the vicinity of the fast atomic peak. The kinetic energies were calculated by assuming that the detected fragment was an oxygen atom. The excitation functions which represent only a small fraction of the available data, have been chosen to illustrate the onset of different processes. These processes are indicated by numbers above the corresponding onsets. As shown in the figure, multiple onsets were often observed for fragments with the same kinetic energy. The relative intensities of the different curves may be obtained by taking into account the appropriate scaling factors (noted beside each curve). Fig. 35 shows an additional excitation function for $N_2$ fragments which was recorded with greater resolution. The excitation function clearly shows the presence of three different dissociation processes which produce a detectable $N_2$ fragment (see later).

Fig. 36 shows sample excitation functions which were recorded using the Rydberg detector tuned to O (top two curves) and N (bottom two curves). The appropriate kinetic energies are indicated in each case.

Fig. 35 An Excitation Function for the Low K.E. Fragments from $N_2O$

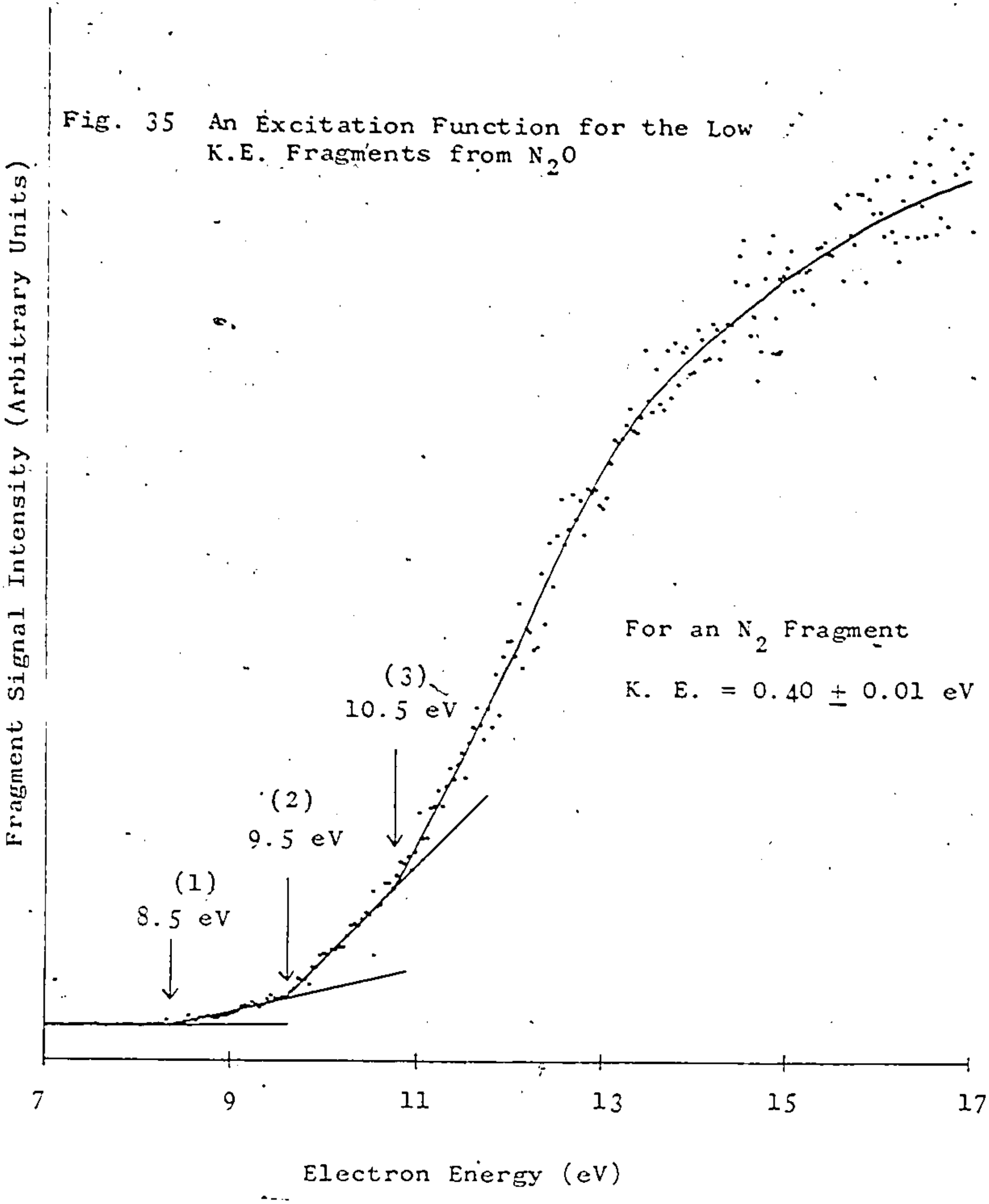

Fig. 36 O-Rydberg and N-Rydberg Excitation Functions for $N_2O$

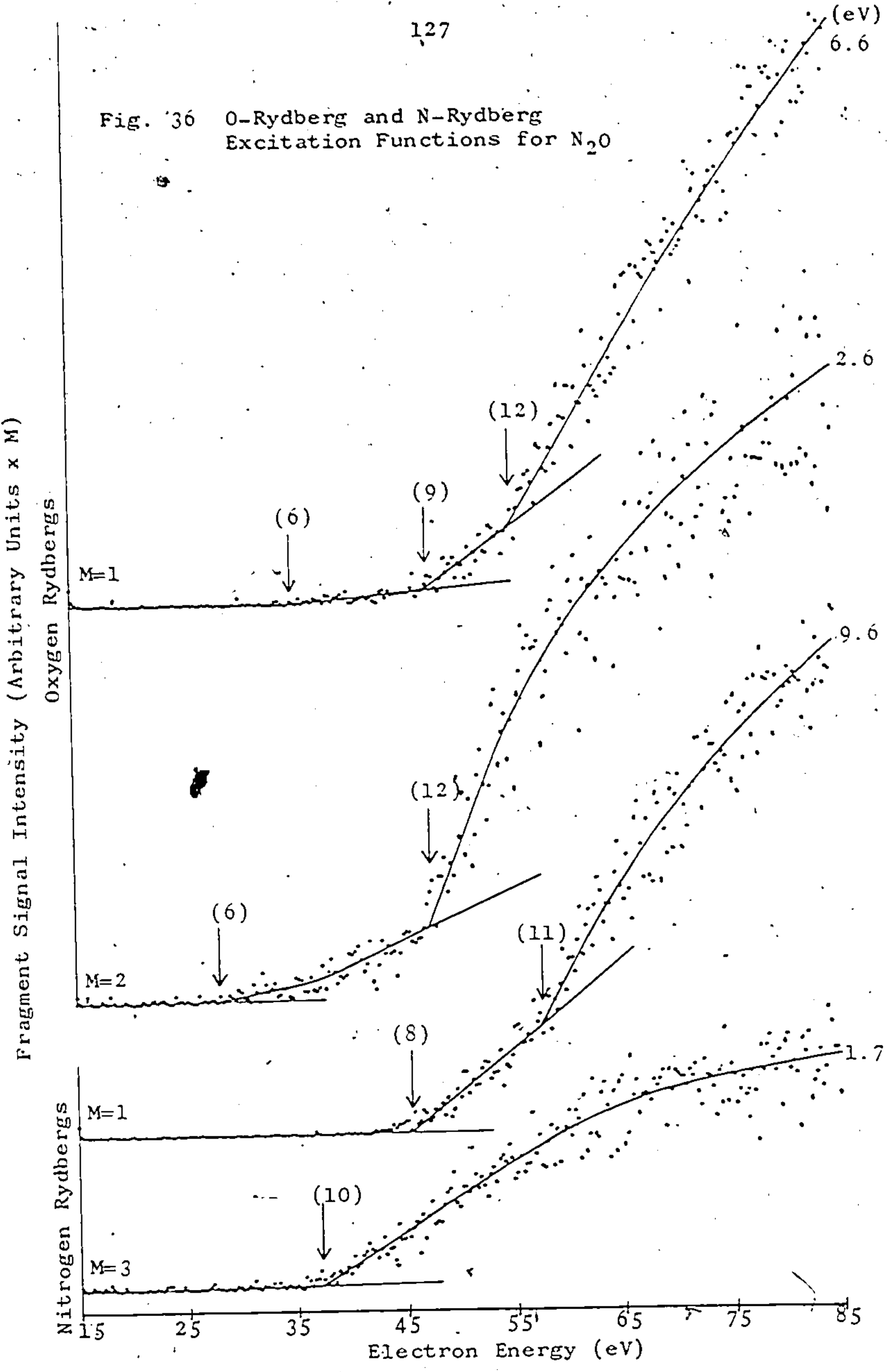

### 5.2.4 Fragment Kinetic Energy as a Function of Appearance Potential

Slope analysis of a plot of fragment kinetic energy against appearance potential, where all the detected fragments were assumed to be oxygen atoms, enabled the processes which produce a detectable molecular fragment, during a two-fragment dissociation of the parent molecule, to be separated from those which produce a detectable atomic fragment. However, it was not possible to distinguish between the production of a nitrogen atom and an oxygen atom or a nitrogen molecule and an NO molecule using this technique because of their similarity in mass. Thus, identification of the detected fragment was dependent on use of the mass sensitive Rydberg detector for the processes which produce Rydberg fragments and on dissociation limit analysis for the remaining processes. Although many dissociation processes were identified in this way, some ambiguity still remains (see later).

All the dissociation processes which produce a detectable nitrogen atom are shown in Fig. 37(a). Similarly, the dissociation processes which produce a detectable oxygen atom are displayed in Fig. 37(b). In addition, Fig. 37(c) shows three dissociation processes which produce detectable $N_2$ molecules. The kinetic energy scales shown in the figures correspond to the actual mass of the detected fragment. A total of twelve different dissociation processes are displayed. Where possible, these are numbered in order of increasing dissociation limit. Most of the data points (open circles) were obtained during use

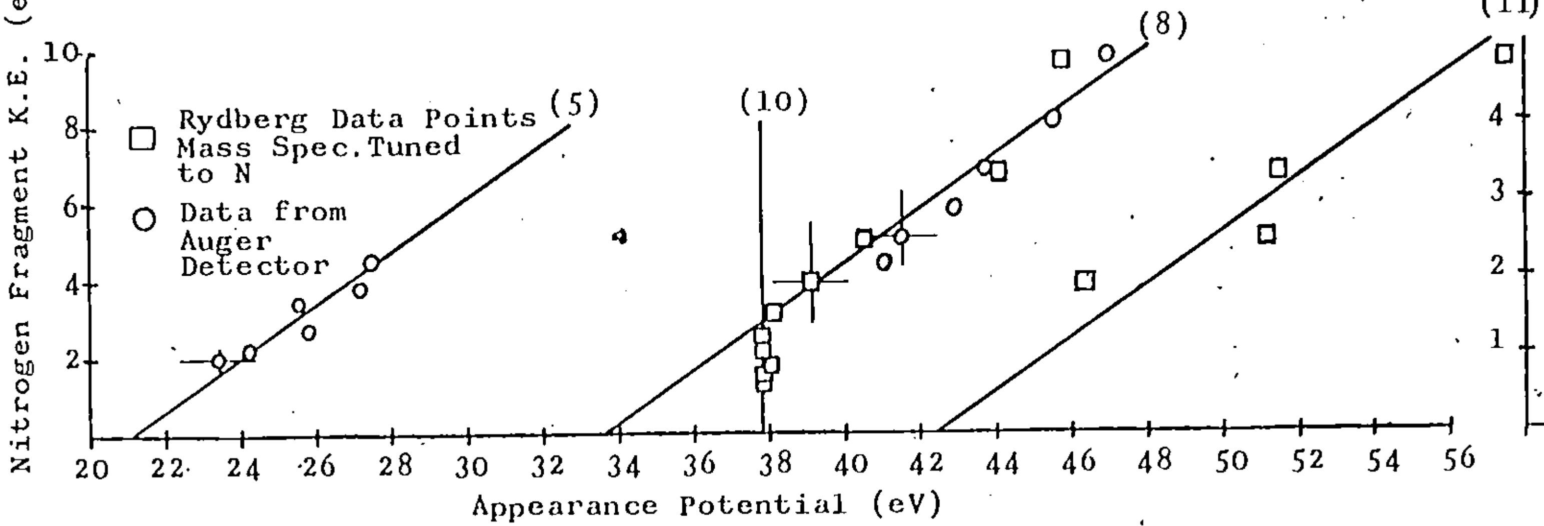

Fig. 37(a) Atomic Nitrogen Producing Processes in $N_2O$

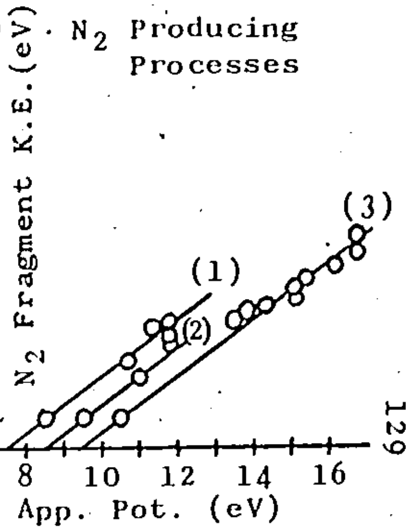

Fig. 37(c) $N_2$ Producing Processes

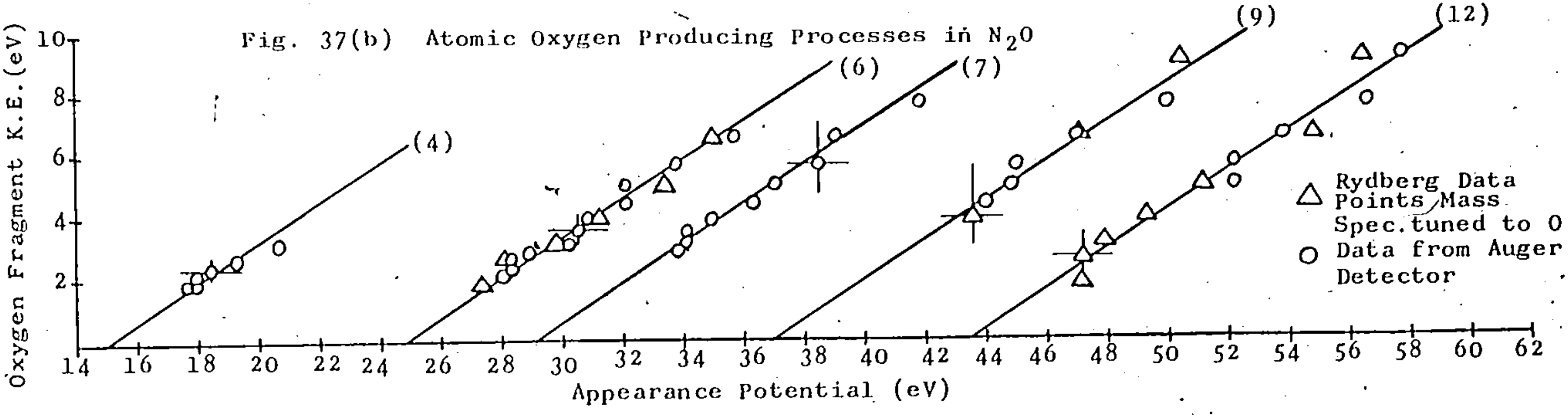

Fig. 37(b) Atomic Oxygen Producing Processes in $N_2O$

of the Auger detector. The production of nitrogen atoms by processes (8), (10) and (11) has been confirmed by the mass sensitive Rydberg detector. The nitrogen Rydberg data points are shown as open squares. Similarly, the production of oxygen atoms by processes (6), (9) and (12) has been confirmed by the Rydberg detector. The oxygen Rydberg data points are shown as open triangles. Many of the dissociation processes produce atomic fragments with similar ranges of kinetic energy. These ranges strongly overlap and hence result in the broad and often structureless distributions of Figs. 32 and 33. This is also true of the processes which produce $N_2$ molecules (see Fig. 37(c) and Fig. 31).

Only one dissociation process was observed to produce fragments with various kinetic energies, but with constant appearance potential [see process (10)]. The detected fragment in this case was a Rydberg nitrogen atom.

## 5.3 Discussion of the Results for $N_2O$

### 5.3.1 Introduction

Table 3 lists dissociation limits (assuming no rotational/vibrational excitation of the molecular fragment) for various possible break-up processes and also gives the measured dissociation limits (obtained from Fig. 37) for comparison. The identification of the different dissociation processes is discussed below. Again, the validity of this identification is dependent on the production of molecular fragments with only small amounts of vibrational energy. This

TABLE 3. The measured dissociation limits and possible dissociation channels in $N_2O$.

| Dissociation Fragments† | Predicted Diss.Limit (eV) | Measured Diss.Lim. ± 1 eV | Process Number | Possible Parent Symmetries | Poss. Parent Multiplicities |
|---|---|---|---|---|---|
| $N_2(A^3\Sigma_u^+) + O(^3P)$ | 7.88 | 7.9* | (1) | $\Pi$ | 1, 3 |
| $N_2(W^3\Delta_u) + O(^3P)$ | 8.88 | | | $\Pi$ | 1, 3 |
| $N_2(B^3\Pi_g) + O(^3P)$ | 8.98 | 8.9* | (2) | $\Sigma^+$, $\Pi$ | 1, 3 |
| $N_2(A^3\Sigma_u^+) + O(^1D)$ | 9.84 | | | $\Sigma^+$, $\Pi$ | 3 |
| $N_2(B'^3\Sigma_u^-) + O(^3P)$ | 9.88 | 9.8* | (3) | $\Sigma^+$, $\Pi$ | 1, 3 |
| $N_2(a^1\Pi_g) + O(^3P)$ | 10.28 | | | $\Sigma^+$, $\Pi$ | 3 |
| $N_2(X^1\Sigma_g^+) + O^+(^4S^0)R$ | 15.3 | 15 | (4) | $\Pi$ | 3 |
| $N_2(C^3\Pi_u) + O(^1S)$ | 16.83 | 16.6 | (4a) | $\Pi$ | 3 |
| $NO(X^2\Pi_r) + N^+(^3P)R$ | 19.47 | | | $\Sigma^+$, $\Pi$ | 1, 3 |
| $N_2(X^1\Sigma_g^+) + O^+(^2P^0)R$ | 20.3 | 20 | | $\Sigma^+$, $\Pi$ | 1, 3 |
| $NO(X^2\Pi_r) + N^+(^1D)R$ | 21.37 | 21 | (5) | $\Sigma^+$, $\Pi$ | 1, 3 |
| $N_2(a^1\Pi_g) + O^+(^4S^0)R$ | 23.88 | | | $\Sigma^+$, $\Pi$ | 3 |
| $N_2(w^1\Delta_u) + O^+(^4S^0)R$ | 24.18 | | | $\Sigma^+$, $\Pi$ | 3 |
| $N_2(A^3\Sigma_u^+) + O^+(^2D^0)R$ | 24.78 | 24.8 | (6) | $\Sigma^+$, $\Pi$ | 1, 3 |
| $N_2^+(B^2\Sigma_u^+) + O(^5S^0)$ | 29.52 | 29.1 | (7) | $\Sigma^-$ | 4 |
| $NO^+(X^1\Sigma^+) + N^+(^1S)R$ | 32.72 | | | $\Sigma^+$, $\Pi$ | 2 |
| $NO^+(a^3\Sigma^+) + N^+(^3P)R$ | 33.67 | 33.6 | (8) | $\Sigma^+$, $\Pi$ | 2, 4 |
| $N_2^+(^4\Sigma_u^+) + O^+(^4S^0)R$ | 36.4 | 36.8 | (9) | $\Pi$ | 2, 4 |
| $N_2^+(A^2\Pi_u) + O^+(^2P^0)R$ | 37.0 | | | $\Sigma^+$, $\Pi$ | 2, 4 |
| $N_2^+(B^2\Sigma_u^+) + O^+(^2D^0)R$ | 37.3 | | | $\Sigma^+$, $\Pi$ | 2, 4 |
| N(HR) + ? | | App. Pot. 37.8 | (10) | | |
| $NO^+(A^1\Pi) + N^+(^1S)R$ | 41.8 | 42.4 | (11) | $\Sigma^+$, $\Pi$ | 2 |
| $N_2^+(C^2\Sigma_u^+) + O^+(^2P^0)R$ | 43.9 | 43.5 | (12) | $\Sigma^+$, $\Pi$ | 2, 4 |

---

* These three measured dissociation limits have been corrected for a small systematic error (see text). The estimated uncertainty in the values is ± 0.2 eV.

† Note that the designation of the core ion is indicated for the Rydberg fragments, e.g. $O^+(^4S^0)R$.

appears to be the case for all dissociation processes which can be identified unambiguously. For all remaining processes, the production of molecular fragments in well known electronic states is taken as an indication of the validity of the assignment. The excitation energies of the electronic states of $N_2$, $N_2^+$, NO and $NO^+$ were obtained from tabulations by Gilmore (1965) and Herzberg (1966). Only those dissociation channels which appear to be energetically consistent with the measured dissociation limits are included in Table 3. Also shown in Table 3 are the possible symmetries and multiplicities of the corresponding molecular or molecular ion parent states.

Figs. 38 and 39 show partial potential energy diagrams for the two-fragment dissociation processes identified in the present work. Fig. 38 shows the results for $N_2$ - O breakup and Fig. 39 shows the results for N - NO breakup. The points at which such potential energy curves cross the Franck-Condon region correspond very approximately to the maximum and minimum appearance potentials observed in each case. These points have been indicated on the figures and potential energy curves have been qualitatively drawn in which connect the points to the measured dissociation limits. All the curves appear to require a potential minimum outside the Franck-Condon region.

### 5.3.2 $N_2$ Fragment Processes

Processes (1), (2) and (3) produce a detectable $N_2$ molecule during a two-fragment dissociation of the parent molecule. Dissociation processes which involve the production of excited NO fragments may be excluded from these assignments since only one such process has a dissociation limit near the measured values. This process involves the production of NO (a $^4\Pi_i$) and N($^4$S) at a dissociation limit of 9.6 eV. Although the NO(a $^4\Pi_i$) is likely to be metastable, it possesses only 4.7 eV excitation energy and hence its detection by the Auger detector is unlikely. N.B. The Auger detector was found to be insensitive to O($^1$S) which has an excitation energy of 4.17 eV.

The measured dissociation limits of processes (1), (2) and (3) are 7.5 eV, 8.5 eV and 9.4 eV respectively. All three dissociation processes produce clear onsets on a single excitation function (see Fig. 35 and the 0.4 eV points on Fig. 37(c)). These onsets are all separated by about 1 eV. The lowest energy dissociation process which produces a detectable $N_2$ molecule has a dissociation limit of 7.88 eV (see Table 3). The next two dissociation channels have very similar dissociation limits which are 1 eV higher in energy at about 8.9 eV. The next group of dissociation channels have dissociation limits which are an additional 1 eV higher in energy. It is therefore very likely that the measured dissociation limits for processes (1), (2) and (3) are all low by about 0.4 of an eV. This has been taken into account in Table 3.

As shown in Table 3, process (1) produces ground state oxygen atoms and $N_2$(A $^3\Sigma_u^+$) molecules. No other detectable channel has a low enough dissociation limit. This dissociation channel has been previously observed by Freund and Klemperer

(1967) during electron impact excitation and by a number of workers during photon absorption [e.g. Young (1969); Gilpin (1971)]. The fragments produced by process (2) are likely to be ground state oxygen atoms and $N_2(B\ ^3\Pi_g)$ molecules. Here the $B\ ^3\Pi_g$ state would quickly radiate into $A\ ^3\Sigma_u^+$ state producing the same metastable $N_2$ fragments as produced by process (1). McEwan et al. (1974) observed this dissociation channel by monitoring radiative emission from the $B\ ^3\Pi_g$ state following excitation by photon absorption at less than 125.6 nm (> 9.87 eV). They also observed the production of $N_2(B\ ^3\Pi_g)$ molecules via a cascade mechanism. They suggest that the cascade takes place from either the $B'\ ^3\Sigma_u^-$ state or the $W^3\Delta_u$ state. The other fragment produced in each case being a ground state oxygen atom. It is interesting to note that the dissociation limit of the $N_2(B'\ ^3\Sigma_u^-)$ producing process compares favourably with the measured limit for process (3). Therefore, it is likely that process (3) involves the production of $N_2(B'\ ^3\Sigma_u^-)$ molecules and ground state oxygen atoms and that the $B'\ ^3\Sigma_u^-$ state cascades into the metastable $A\ ^3\Sigma_u^+$ state via the $B\ ^3\Pi_g$ state. It is very likely that process (3) was also observed by Clampitt and Newton (1969). They observed a dissociation process with a limit of 9.95 eV and suggest that the process involves the production of either $N_2(B'\ ^3\Sigma_u^-)$ or $N_2(a\ ^1\Pi_g)$ molecules. An additional possibility for process (3) involves the production of $N_2(A\ ^3\Sigma_u^+)$ molecules and $^1D$ oxygen atoms (see Table 3).

The excitation functions from which processes (1),

(2) and (3) were identified appear to peak sharply above threshold indicating that at least two of the processes involve a change in multiplicity during the initial excitation of the parent molecule (see 0.95 eV curve of Fig. 34). This seems somewhat surprising since the dissociation channels corresponding to processes (1), (2) and (3) appear to be accessible by photon absorption as well as by electron impact (see above). This suggests that the initial excitations of the parent molecule are spin allowed (i.e. no change in multiplicity). One possible explanation for the observed structure is that two of the processes do involve the excitation of triplet parent states (see Table 3) by electron impact. These states could have the same dissociation limits as the singlet states excited by photon absorption (N.B. the ground state of $N_2O$ is a singlet $\Sigma^+$). The excitation of singlet and triplet parent states of the same dissociation channel may also occur. It is interesting to note that the alternative dissociation channels for process (3) correlate only with triplet parent states. Clearly, the $N_2$ molecules produced by processes (1), (2) and (3) possess little or no vibrational excitation energy.

There is some uncertainty as to whether an additional $N_2$ producing process has an onset at about 19.2 eV in the excitation function for 0.95 eV fragments (see Fig. 34). There is a clear increase in signal intensity at this energy [see arrow labelled 4(a)]. However, this increase could be due to the overlap of signal from two of the previously discussed processes, namely, those responsible for the two peaks in the excitation function. The addition of two such curves, which peak sharply above threshold but at different energies, could conceivably produce the observed structure. Alternatively, a two-fragment dissociation process with a dissociation limit at about 16.6 eV could be responsible. Only one suitable dissociation channel has a dissociation limit which lies within ± 1 eV of this value. This channel produces $N_2(C\ ^3\Pi_u)$ and $O(^1S)$ at a dissociation limit of 16.83 eV (see Table 3). The $C\ ^3\Pi_u$ state of the $N_2$ molecule would quickly cascade into the metastable $A\ ^3\Sigma_u^+$ state via the $B\ ^3\Pi_g$ state. It is interesting to note that the above dissociation fragments correlate only with a triplet parent state. If the process does exist it apparently produces $N_2$ molecules with only small amounts of kinetic energy (i.e. under 1 eV). For this reason, it was not possible to obtain appearance potentials for a range of fragment kinetic energies. The $O(^1S)$ atoms produced by this process would also have fairly low kinetic energies (under 1.7 eV). $^1S$ oxygen atoms were not detected in the present experiment. It should be noted that no suitable NO producing process has a dissociation limit near the corresponding measured value.

### 5.3.3 Oxygen Fragment Processes

It is likely that processes (4), (6), (7), (9) and (12) produce a detectable oxygen atom during a two-fragment dissociation of the parent molecule. This has been confirmed for processes (6), (9) and (12) using the mass sensitive Rydberg detector. The identity of the detected fragment produced by the other two processes is less certain.

Process (4) was observed only weakly during the present work. The signal onsets were not very clear and were only present on a small number of excitation functions. Therefore, there is some uncertainty as to whether the process exists at all. However, evidence for its existence comes from the measured dissociation limit of 15 eV. As shown in Table 3, the first dissociation process which is expected to produce oxygen atoms in Rydberg states has a dissociation limit at about this energy. In addition, Curran and Fox (Curran 1961) list an appearance potential of 15.5 eV for the production of $O^+$ from $N_2O$. It is likely, therefore, that process (4) produces ground state $N_2$ molecules and Rydberg oxygen atoms. It is also likely that the signal intensity from this process was too low to enable the oxygen atoms to be detected by the Rydberg detector. It should be noted that a detectable nitrogen atom could not be produced by process (4) since the corresponding dissociation limit is too low. The lowest energy dissociation process which produces a detectable nitrogen atom has a dissociation limit of about 19.5 eV (see Table 3).

Process (6) has a measured dissociation limit of 24.8 eV and produces a Rydberg oxygen atom. There are three suitable dissociation channels which lie within ± 1 eV of the measured dissociation limit. The most likely of these has a dissociation limit of 24.78 eV and produces an $N_2(A\ ^3\Sigma_u^+)$

molecule and a Rydberg oxygen atom based on a $^2D^0$ core ion. Although weak, there is some evidence to suggest that the $N_2(A\ ^3\Sigma_u^+)$ molecule, produced by this process, was also detected. This evidence comes from the excitation function recorded for 1.6 eV $N_2$ molecules (see Fig. 34). An $N_2$ molecule from the above process would produce a signal onset at about 29.2 eV on this curve. The expected position is marked by an unlabelled arrow. Both the 1.6 eV and the 0.95 eV excitation functions peak at an electron energy of about 24.2 eV. However, above this energy there is a steady decline in the 0.95 eV curve. In contrast, the 1.6 eV curve shows a slight increase in signal with an onset somewhere near the expected electron energy. This increase in signal intensity could be due to process (6). It is significant to note that onsets for the Rydberg oxygen atoms produced by process (6) could not be obtained for kinetic energies below 1.8 eV [see Fig. 37(b)]. The corresponding kinetic energy of the $N_2$ fragments would be 1.0 eV. This fact could explain the absence of a suitable $N_2$ onset on the 0.95 eV excitation function (see Fig. 34).

The other possible dissociation channels for process (6) involve the production of Rydberg oxygen atoms based on the $^4S^0$ core ion. One of the processes produces $N_2(W^1\Delta_u)$ at a dissociation limit of 24.18 eV and the other produces $N_2(a^1\pi_g)$ at a dissociation limit of 23.88 eV. One argument against the participation of these channels is that they both involve a change in multiplicity during the initial excitation of the parent molecule (see Table 3). The excitation functions do not indicate a change in multiplicity.

As pointed out above, the identify of the detected fragment produced by process (7) is somewhat uncertain. However, the production of a nitrogen atom seems unlikely since the process does not appear to produce atoms in Rydberg states and the low-lying metastable states of nitrogen have insufficient energy to be detected. The most likely fragment to be produced is an oxygen atom in the 3s $^5S^0$ state. If this fragment is produced with an $N_2^+(B^2\Sigma_u^+)$ ion then the expected dissociation limit is 29.52 eV. This dissociation limit compares favourably with the measured value of 29.1 eV. No other dissociation channel which produces $O(^5S^0)$ is available within ± 2 eV of the measured dissociation limit. However, one problem which arises from this assignment is concerned with the symmetry of the excited parent state. As shown in Table 3, the suggested dissociation fragments correlate only with a $\Sigma^-$ parent state. Thus, the initial excitation would involve a transition from a $\Sigma^+$ to a $\Sigma^-$ state. A direct transition of this kind is usually forbidden during electron impact.

Process (9) has a measured dissociation limit of 36.8 eV and produces a Rydberg oxygen atom. There are three suitable dissociation channels which lie within ± 1 eV of the measured dissociation limit. The first of these produces a Rydberg oxygen atom (based on a $^4S^0$ core ion) and an $N_2^+(^4\Sigma_u^+)$ ion at a dissociation limit of 36.4 eV. An alternative channel produces Rydberg oxygen atoms which have $^2P^0$ core ions. The other fragments produced in this case are $N_2^+(A\ ^2\Pi_u)$ ions at a dissociation limit of 37 eV. The final alternative produces a Rydberg oxygen atom (based on a $^2D^0$ core ion) and an $N_2^+(B\ ^2\Sigma_u^+)$ ion at a dissociation limit of 37.3 eV. It is not possible to say which of these dissociation channels are responsible for process (9) from the present measurements.

Process (12) has a measured dissociation limit of 43.5 eV and produces a Rydberg oxygen atom. Only one suitable dissociation channel lies within ± 1 eV of the measured dissociation limit. This channel produces a Rydberg oxygen atom (based on a $^2P^0$ core ion) and an $N_2^+(C^2\Sigma_u^+)$ ion at a dissociation limit of 43.9 eV.

### 5.3.4 Nitrogen Fragment Processes

Processes (8) and (11) produce a Rydberg nitrogen atom during a two-fragment dissociation of the parent molecule. Process (10) also produces a Rydberg nitrogen atom but in this case the fragmentation process is more complicated (see later). The identity of the detected fragment produced by process (5) is less certain but again the process involves a two-fragment dissociation of the parent molecule.

Process (5) was observed only weakly during the present work. The signal onsets were not very clear and were only present on a small number of excitation functions. If the process produces a detectable nitrogen atom, it must be in a Rydberg state since the low-lying metastable states of nitrogen have insufficient energy to be detected The measured dissociation limit of process (5) is 21 eV. As shown in Table 3, the first dissociation process which is expected to produce nitrogen atoms in Rydberg states has a dissociation limit at about 19.47 eV. This value seems to be too low. However, if the Rydberg nitrogen atom has a $^1D$ core ion, then the expected dissociation limit is 21.37 eV. In both cases, the undetected fragment is a ground state NO molecule [i.e. $NO(X\ ^2\Pi_r)$]. No other nitrogen producing process has a dissociation limit within ± 2 eV of the measured value. Support for the above assignment comes from the ionization work of Curran and Fox (Curran 1961). They list an appearance potential of 20.81 eV for the production of $N^+$ from $N_2O$. It is likely that the signal intensity from process (5) was too low to enable the nitrogen atoms to be detected by the Rydberg detector. An additional, though less likely possibility for process (5) is the production of a detectable oxygen atom. In this case, the measured dissociation limit would be 20 eV. The only suitable dissociation channel with a dissociation limit near this value is based on the production of an $N_2(X\ ^1\Sigma_g^+)$ molecule and an oxygen Rydberg atom based on a $^2P^0$ core ion. The expected dissociation limit of this channel is about 20.3 eV.

Process (8) has a measured dissociation limit of 33.6 eV and produces a Rydberg nitrogen atom. There are only two suitable dissociation channels which lie within ± 1 eV of the measured dissociation limit. The most likely of these has a dissociation limit of 33.67 eV and produces an $NO^+(a\ ^3\Sigma^+)$ ion and a Rydberg nitrogen atom based on a $^3P$ core ion. A less likely candidate is based on the production of a ground state $NO^+$ ion [i.e. $NO^+(X\ ^1\Sigma^+)$] and a Rydberg nitrogen atom based on a $^1S$ core ion. The expected dissociation limit of this channel is about 32.72 eV.

Process (10) produces Rydberg nitrogen atoms with various kinetic energies at a constant appearance potential of 37.8 eV. A number of possible dissociation mechanisms could be responsible for this effect (see section 1.4 of Chapter 1). Firstly, it is not possible to rule out a total fragmentation of the parent molecule where the atomic fragments fly off in arbitrary directions. Certainly, sufficient energy is given to the parent molecule to allow the production of Rydberg nitrogen atoms during such a dissociation process. The dissociation into different directions could occur during a non-linear vibration of the parent molecule.

Secondly, the above effect could result during a two-fragment dissociation of the parent molecule where the dissociation can proceed by a number of different paths each corresponding to the same amount of electronic energy in the fragments, but to a different amount of vibrational energy in the NO molecule (see section 1.4 of Chapter 1). These paths could be due to modifications of the potential hypersurface due to surface crossings. This suggestion seems particularly attractive since process (10) appears to be connected with process (8). It should be noted that data points for process (8) could not be obtained for appearance potentials below about 38 eV and data points for process (10) could not be obtained for kinetic energies above the intersection of the two respective lines on Fig. 37(a). The two processes could in fact be different manifestations of a single dissociation process where the available energy is partitioned in different ways between translation and vibration (see section 1.4 of Chapter 1). If this is the case, process (10) could produce fragments with the same electronic excitation energies as process (8) (i.e. the productions of $NO^+(a\ ^3\Sigma^+)$ and a Rydberg nitrogen atom). Such a suggestion has also been made by Schiavone et al. (Schiavone, 1977) in order to explain a similar occurrence observed in the dissociation of $CH_4$.

An additional possibility for process (10) involves the initial excitation of a repulsive state of the neutral molecule which lies above a similar state of the molecular ion within the Franck-Condon region, but has a lower dissociation limit (i.e. the respective surfaces cross). Such a state may autoionize into the continuum of the molecular ion state and release an electron of variable kinetic energy. The molecular ion could then undergo a two-fragment dissociation and produce fragments with various kinetic energies at a fixed appearance potential. In such a case, the undetected fragment produced by process (10) would be an $NO^+$ ion. Similar dissociation processes have been observed in $H_2$ (Köllmann, 1977).

Process (11) has a measured dissociation limit of 42.4 eV and produces a Rydberg nitrogen atom. Only four data points were obtained for this process and these appear to be somewhat scattered. However, there is only one well known state of $NO^+$ which could combine with a Rydberg nitrogen atom in order to produce such a high dissociation limit. This state is the A $^{1}\pi$ which has an excitation energy of about 18.3 eV. If an $NO^{+}$ ion in this state is produced with a Rydberg nitrogen atom (based on a $^{1}S$ core ion) then the expected dissociation limit is 41.8 eV. This value agrees fairly well with the measured dissociation limit. √

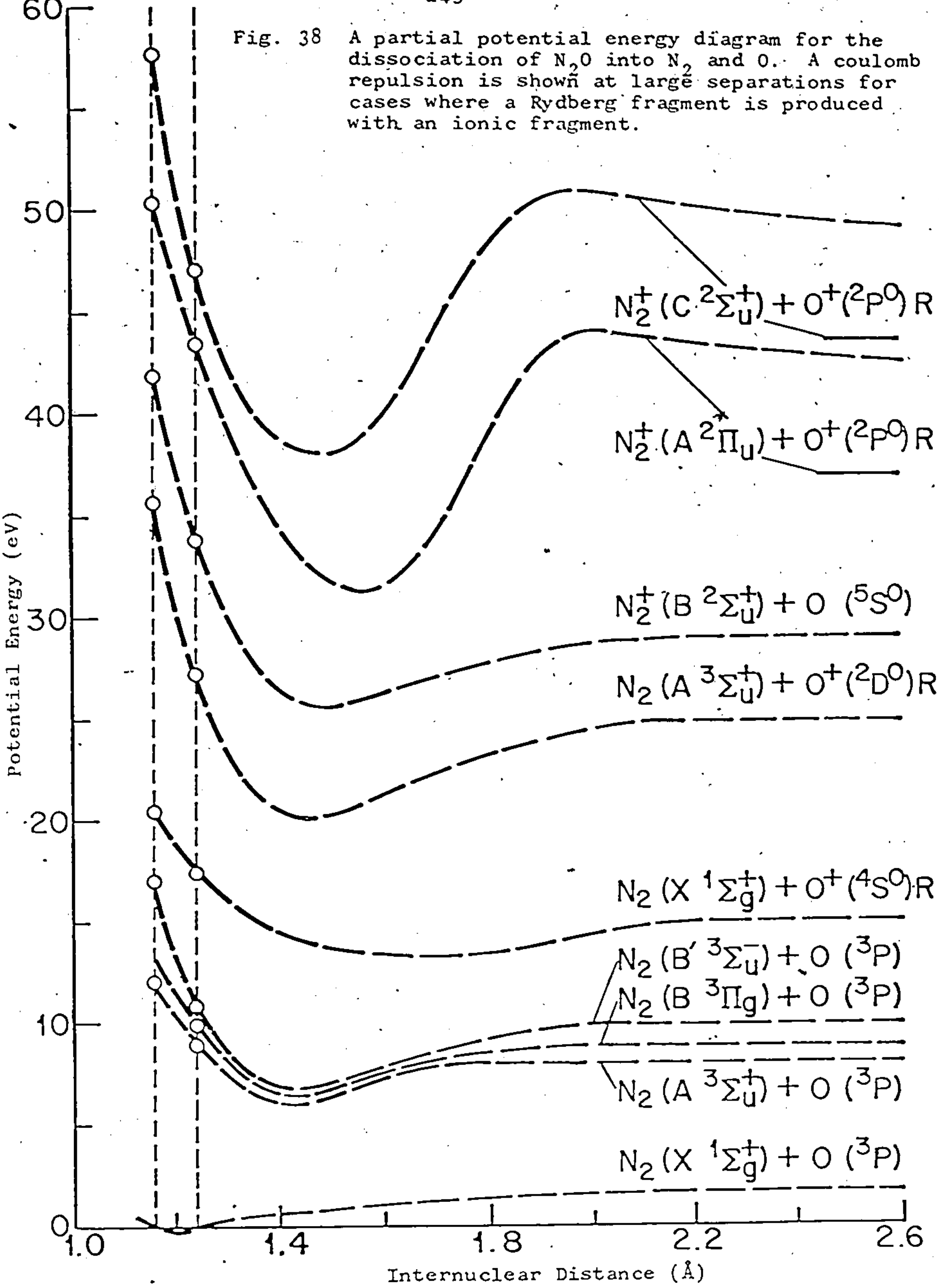

Fig. 38 A partial potential energy diagram for the dissociation of $N_2O$ into $N_2$ and O. A coulomb repulsion is shown at large separations for cases where a Rydberg fragment is produced with an ionic fragment.

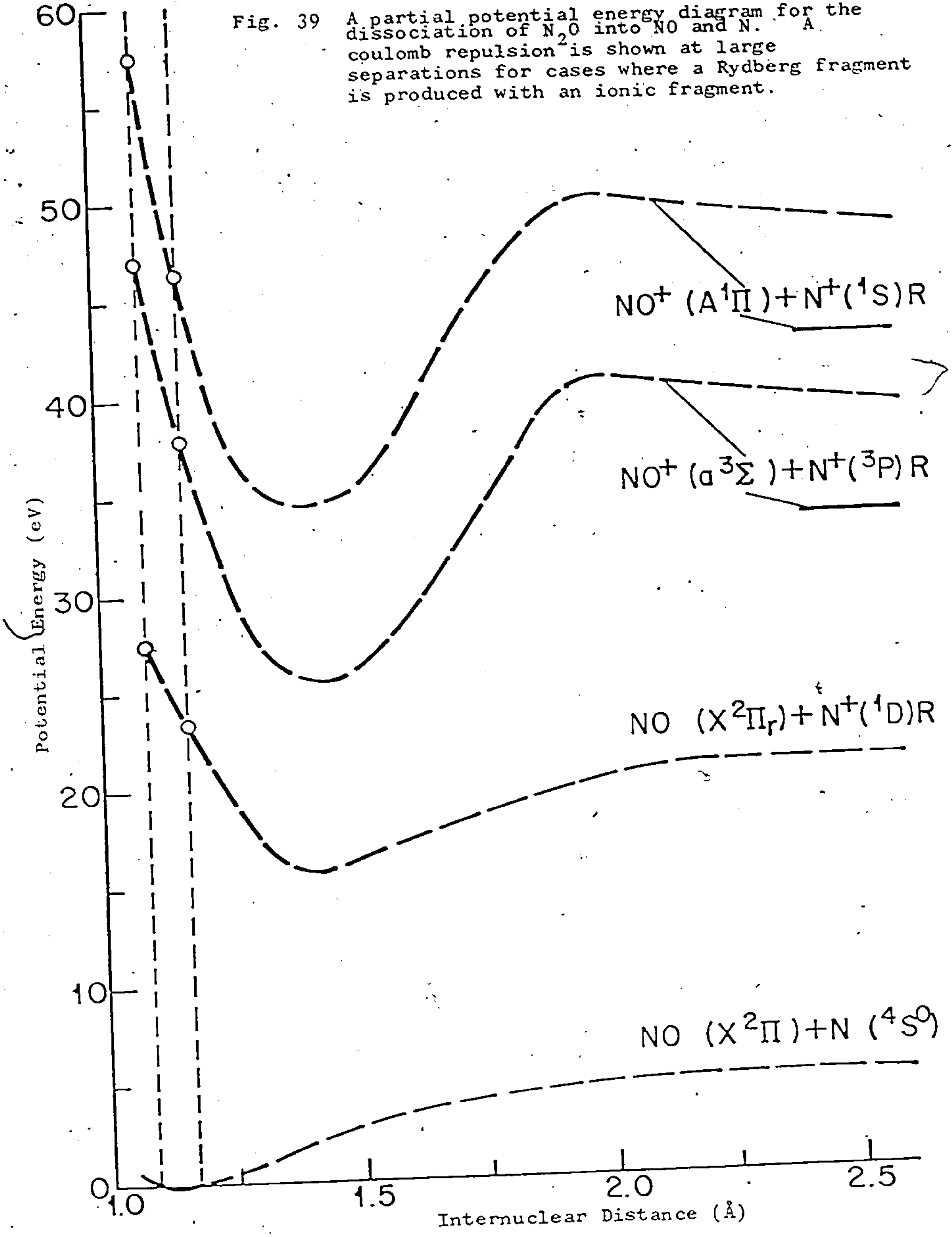

Fig. 39 A partial potential energy diagram for the dissociation of $N_2O$ into NO and N. A coulomb repulsion is shown at large separations for cases where a Rydberg fragment is produced with an ionic fragment.

# SUMMARY AND CONCLUSIONS

Metastable atoms and molecules, including Rydberg species, have been directly detected following the electron impact dissociation of $CO_2$, $CCl_2F_2$, $CCl_3F$ and $N_2O$. The kinetic energies of these fragments were measured during time-of-flight spectroscopy. Excitation function measurements of fragments of known kinetic energy provided information about the mass of the detected fragment, the number of fragments produced, the dissociation limit of the excited state of the parent molecule and the sharing of energy between translation of the fragments and the vibrational degrees of freedom of any molecular fragments produced. This information was obtained from plots of fragment kinetic energy against appearance potential. Unambiguous identification of the Rydberg fragments was achieved during use of a mass sensitive Rydberg detector. Both Rydberg and non-Rydberg fragments were also detected by an Auger detector.

Two fragments were produced in most of the dissociation processes identified in the present work. One of the fragments was usually an excited atom and the other an electronically excited molecule. However, in most cases the molecular fragments appeared to receive little or no vibrational energy. Only one dissociation process was observed where the molecular fragments were apparently produced with significant amounts of vibrational energy. In this case, the fragments were produced with different amounts of vibrational energy at a constant appearance potential. This resulted in the production of fragments of various kinetic energies at constant appearance potential.

Comparison of the measured dissociation limits with those of possible dissociation channels in the molecule under study, often enabled the excited states of the fragments to be identified. All the data is summarized in Tables 1-3.

Where more than two fragments were produced during a one step dissociation of a non-linear molecule, fragments of various kinetic energies were also produced at a constant appearance potential.

# BIBLIOGRAPHY

Ajello, J.M., Huntress, W.T. and Rayermann, P. 1976. J. Chem. Phys. 64, 4746.

Allcock, G. 1975. M.Sc. Thesis, University of Windsor, (unpublished).

Appell, J. and Kubach, C. 1971. Chem. Phys. Letts. 11, 486.

Black, G., Sharpless, R.L., Slanger, T.F. and Lorents, D.C. 1975. J. Chem. Phys. 62, 4266.

Brom, J.M. and Broida, H.P. 1975. Chem. Phys. Letts. 33, 384.

Chamberlain, J.W. 1961. Physics of the Aurora and Airglow, Academic Press.

Clampitt, R. and Newton, A.S. 1968. Surface Sci. 12, 92.

Clampitt, R. and Newton, A.S. 1969. J. Chem. Phys. 50, 1997.

Cottrell, T.L. 1962. The Strengths of Chemical Bonds, Butterworths Scientific Publications, London.

Curran, R.K., Fox, R.E. 1961. J. Chem. Phys. 34, 1590.

Doucet, J., Sauvageau, P. and Sandorfy, C. 1973. J. Chem. Phys. 58, 3708.

Dunn, G.H. 1962. Phys. Rev. Letters, 8, 62.

Franklin, J.L., Dillard, J.G., Rosenstock, H.M., Herron, J.T., Draxl, K. and Field, F.H. 1969. NSRDS-NBS 26, U.S. Dept. of Commerce.

Freund, R.S. and Klemperer, W. 1967. J. Chem. Phys. 47, 2897.

Freund, R.S. 1971. J. Chem. Phys. 55, 3569.

Gilbert, R., Sauvageau, P. and Sandorfy, C. 1974. J. Chem. Phys. 60, 4820.

Gilmore, F.R. 1965. J. Quant. Spect. Rad. Trans. 5, 369.

Gilpin, R. and Welge, K.H. 1971. J. Chem. Phys. 55, 975.

Gruzdev, P.F. 1971. Optics and Spectroscopy, 30, 319.

Hagstrum, H.D. 1954. Phys. Rev. 96, 336.

Hampson, R.F. and Okabe, H. 1970. J. Chem. Phys. 52, 1930.

Heddle, D.W.O. 1967. Proc. Phys. Soc. 90, 81.

Herzberg, G. 1966. Molecular Spectra and Molecular Structure I & III, Van Nostrand, New York.

Huebner, R.H., Bushnell, D.E., Celotta, R.J., Mielczarek, S.R. and Kuyatt, C.E. 1975. Nature, 257, 376.

Jochims, H.W., Lohr, W. and Baumgartel, H. 1976. Berichte der Bunsen Gesellschaft, 80, 130.

King, G.C. and McConkey, J.W. 1978. J. Phys. B. (in press).

Köllmann, K. 1977. Private communication and Abstracts X ICPEAC, 1, 577.

Kuhn, H.G. 1969. Atomic Spectra, Longmans, London.

Lee, L.C., Carlson, R.W., Judge, D.L. and Ogawa, M. 1975. J. Phys. B. 8, 977.

McConnell, J.C. and McElroy, M.B. 1970. J. Geophys. Res. 75, 7290.

McEwan, M.J., Lawrence, G.M. and Poland, H.M. 1974. J. Chem. Phys. 61, 2857.

Misakian, M., Mumma, M.J. and Faris, J.F. 1975. J. Chem. Phys. 62, 3442.

Mumma, M.J., Stone, E.J. and Zipf, E.C. 1971. J. Chem. Phys. 54, 2627.

Mumma, M.J., Stone, E.J. and Zipf, E.C. 1975. J. Geophys. Res. 80, 161.

Murray, J.R. and Rhodes, C.K. 1973. Lawrence Livermore Laboratory, Preprint UCRL-51455.

Nicolet, M. 1974. Can. J. Chem. 52, 1382.

Person, J.C., Fowler, D.E. and Nicole, P.P. 1975. Argonne Nat. Lab. Report ANL-75-60 Pt.1.

Pichanick, F.M.J. and Simpson, J.A. 1968. Phys. Rev. 168, 64.

Rockwood, S.D. 1973. Los Alamos Scientific Laboratory Preprint LA-UR-73-1031.

Roland, F.S. and Molina, M.J. 1975. Rev. Geophys. and Space Phys. 13, 1.

Schiavone, J.A. and Freund, R.S. 1975. Private communication.

Schiavone, J.A., Donohue, D.E. and Freund, R.S. 1977. J. Chem. Phys. 67, 759.

Smyth, K.C., Schiavone, J.A. and Freund, R.S. 1973. J. Chem. Phys. 59, 5225.

Smyth, K.C., Schiavone, J.A. and Freund, R.S. 1974. J. Chem. Phys. 61, 1789.

Tilford, S.G. and Simmons, J.D. 1972. J. Phys. Chem. Ref. Data 1, 147.

Weise, W.L., Smith, M.W. and Miles, B.M. 1969. Atomic Transition Probabilities, 2, NSRDS-NBS 22, U.S. Dept. of Commerce.

Wells, W.C., Borst, W.L. and Zipf, E.C. 1972. J. Geophys. Res. 77, 69.

Young, R.A., Black, G. and Slanger, T.G. 1968. J. Chem. Phys. 48, 2067.

Young, R.A., Black, G. and Slanger, T.G. 1969. J. Chem. Phys. 50, 303.

Zare, R.N. 1967, J. Chem. Phys. 47, 204.

# Vita Auctoris

I was born in Harrogate, England, on March 4th 1951. In the summer of 1972 I graduated from the University of York (England) with an honours degree in Physics. In January 1973 I began graduate work in Physics at the University of Windsor and graduated with an M.Sc. degree in the summer of 1975. I was married in 1974 and have one child.

## LIST OF PUBLICATIONS

The publications which have resulted from the present study are listed below.

1. 'The Dissociation of $N_2O$ into Metastable Fragments following Electron Impact Excitation'.
   G. Allcock and J.W. McConkey (to be published 1978).
2. 'The Dissociation of $CCl_2F_2$ and $CCl_3F$ into Metastable Fragments Following Electron Impact Excitation'.
   G. Allcock and J.W. McConkey, J. Phys. B. 11, 741 (1978).
3. 'Metastable Fragmentation of $N_2O$ under Electron Impact'.
   G. Allcock and J.W. McConkey, Bull. Amer. Phys. Soc. 22, 1330 (1977).
4. 'Metastable Fragmentation Patterns of $CCl_2F_2$ and $CCl_3F$ Following Electron Impact'.
   G. Allcock and J.W. McConkey, Abstracts X I.C.P.E.A.C., 1, 576 (1977).
5. 'Metastable Fragment Production Following Electron Impact on $CO_2$'.
   G. Allcock and J.W. McConkey, J. Phys. B. 9, 2127 (1976).
6. 'Metastable Fragment Production in the Dissociation of Simple Molecules by Electrons'.
   G. Allcock and J.W. McConkey, Abstracts IX I.C.P.E.A.C., 2, 820 (1975).
7. 'Time-of-Flight Study of Molecular Dissociation by Electrons'.
   G. Allcock and J.W. McConkey, Bull. Amer. Phys. Soc., Dec. 1974).